CHALMERS

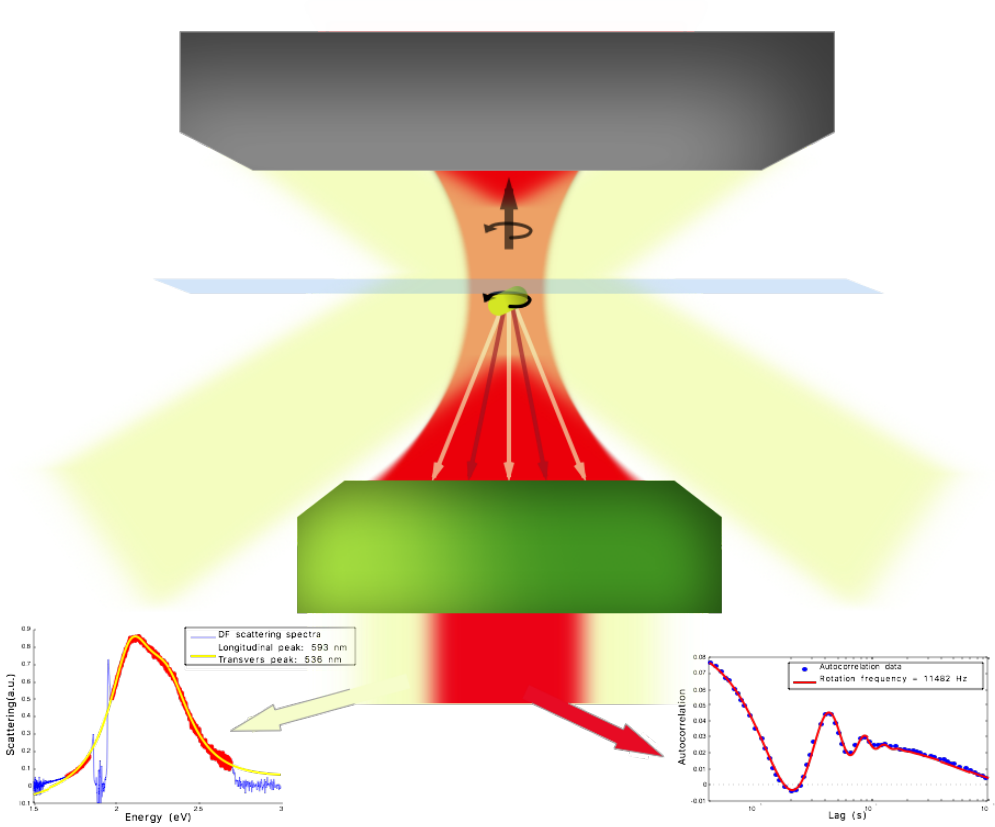

Spectroscopic investigations of rotating gold nanorods in an optical trap

Master's Thesis in Nanotechnology

DANIEL ANDRÉN

Bionanophotonics
Department of Physics
Chalmers University of Technology
Gothenburg, Sweden 2016

Master's Thesis in Nanotechnology

Spectroscopic investigations of rotating gold nanorods in an optical trap

Daniel Andrén

Supervisors:

Mikael Käll

Lei Shao

Srdjan Aćimović

Bionanophotonics - Department of Physics

Chalmers University of Technology

Gothenburg, Sweden 2016

Spectroscopic investigations of rotating gold nanorods in an optical trap
Daniel Andrén

Master's thesis 2016:03
Bionanophotonics, Department of Physics
Chalmers University of Technology
SE-412 96 Gothenburg
Sweden
Phone: +46 (0)31-772 1000

Cover illustration: Schematic illustration of a gold nanorod trapped and rotated against a cover glass. From scattered laser and illumination light the dark-field scattering spectra as well as the rotation frequency can be obtained.

Chalmers Reposervice
Gothenburg, Sweden 2016

Abstract

Due to their extraordinary plasmonic properties, gold nanorods are prime candidates for a variety of sensory, biomedical, spectroscopic, and data storage applications. Recent studies have demonstrated that gold nanorods trapped by optical tweezers can function as nanoscopic rotary motors driven by scattering induced optical torques. The system holds promise for applications within numerous fields, ranging from nano/microfluidic flow control and nanorobotics to sensing and DNA manipulation. However, for many proposed applications, understanding and controlling the photothermal effects associated with laser trapping is crucial. The reason being that they could lead to a number of unwanted effects, but could also be interesting and useful in their own right.

To deduce how photothermal effects such as heating, reshaping, and possibly bubble formation affect the particle, spectroscopic investigations on trapped rotating gold nanorods were performed. An optical setup was constructed which included circularly polarized laser tweezers, dark-field illumination, photon correlation spectroscopy, video microscopy, and a free-space coupled grating spectrometer. The setup allowed continuous real-time measurements of scattering spectra and rotational dynamics of individual monocrystalline gold nanorods at high resolution over extended periods of time. Through continuous tracking of plasmon resonance shifts and rotational dynamics of trapped particles, a number of important effects were observed. These included changes in the refractive index of the water surrounding, nanoparticle reshaping effects and bubble generation. Moreover, it was found that by using a small collection fiber information about translational Brownian motion of the trapped particle is detectable in the autocorrelation signal.

The results presented in this thesis shed light on thermal processes on the nanoscale and will be useful in evaluating the applicability and performance of nanorod motors for possible future applications.

Keywords: Optical tweezers, localized surface plasmon, optical rotation, DF spectroscopy, gold nanorod, photothermal effects.

Acknowledgements

The work during the past year, which has led up to this master's thesis, has been fascinating indeed. There is a range of people who all have made both my scientific endeavours and personal growth during this year possible, and for that I am truly grateful.

First, a sincere thanks to my supervisor Mikael Käll for believing in me to develop, perform, and complete this project. I am very thankful to you for all the guidance and inspiration you have provided during the course of the project. You have been an excellent mentor and your inquisitiveness, experience, and ability to always find an interesting direction to steer a project are things I admire and strive towards.

Also, I would like to express my gratitude to Lei Shao. Thank you for all the time you spent teaching me about optical trapping, plasmonics and the field in general, but just as much for all the valuable help I have received from you regarding experimental work, data analysis, and scientific methodology. You have been an inestimable asset to me when performing and completing this project.

I thank Srdjan Ćimović for all his help with understanding the spectroscopic measurement techniques and for sharing his amazing measurement interface. I hope your attention to detail and your realistic and pragmatic view on science has rubbed off on me. Moreover, your company has been a pleasure during countless lunches throughout the year.

Thank you to Faegheh Hajizadeh for all the valuable help during the construction of the optical tweezers setup. You provided me with an understanding regarding tweezing which I have found useful during the entire project. Thank you also for the introduction into trapping stability and data analysis of such measurements.

A big thanks to Nils Odebo Länk who has helped me understand much of the theoretical models necessary for this project and who has also provided simulations to further deepen the analysis of the measured results. Thank you for always keeping your door open and for always making time to answer my, sometimes stupid, questions.

Of course, a great thanks to the rest of the people at the Bionanophotonics division for making it such a great place to work, Robin Ogier, Ruggero Verre, Martin Wersäll, Timur Shegai, Gustav Emilsson, Kunli Xiong, Andreas Dahlin, Hana Sipova, Pawel Karpinski, and Peter Johansson.

I want to thank my family and my girlfriend for always supporting and encouraging me during my entire education. Lastly, a huge thanks to all the wonderful people I have had the chance to befriend during my time at Chalmers. You have made my entire study period an amazing experience.

Daniel Andrén, Göteborg 6/3/16

Contents

Page

Abstract **v**

Acknowledgements **vi**

List of Figures **xv**

1 Introduction **1**
- 1.1 Plasmonics . . . 1
- 1.2 Optical tweezers . . . 2
  - 1.2.1 Optical rotation . . . 3
- 1.3 Reshaping . . . 5
- 1.4 Spectroscopy . . . 5
- 1.5 Purpose and aim . . . 6

2 Theory **7**
- 2.1 Localized surface plasmon resonance . . . 7
  - 2.1.1 Quasi-static approximation . . . 8
    - 2.1.1.1 Spherical case . . . 9
    - 2.1.1.2 Spheroidal case . . . 9
    - 2.1.1.3 MLWA correction . . . 10
    - 2.1.1.4 Calculated cross sections . . . 11
- 2.2 Optical tweezers . . . 13
  - 2.2.1 Optical force calculations . . . 15
  - 2.2.2 Trapping stiffness . . . 18
- 2.3 Optical rotation . . . 19
  - 2.3.1 Torque calculations . . . 20
  - 2.3.2 Rotational dynamics through autocorrelation . . . 21
    - 2.3.2.1 Temperature estimation . . . 22

3 Experimental methods **23**
- 3.1 Construction of Optical tweezers . . . 23
  - 3.1.1 Trapping system . . . 24
  - 3.1.2 Laser intensity . . . 28

3.2 Circular polarization of laser . . . 28
3.2.1 Measurement of polarization phase . . . 28
3.2.2 Phase correction . . . 30
3.3 Nanorod selection criteria . . . 31
3.3.1 Selective shortening of nanorods . . . 33
3.4 Trapping stiffness measurement . . . 34
3.5 Single nanoparticle spectroscopy . . . 35
3.5.1 Dark-field scattering spectroscopy . . . 35
3.5.2 Calibration of spectra . . . 36
3.5.2.1 Self-fluorescence of glass slide . . . 37
3.6 Determination of LSPR peaks . . . 38
3.7 Experimental procedure . . . 39

4 Results and Discussion **41**
4.1 Trapping stiffness measurement . . . 41
4.2 Autocorrelation analysis . . . 44
4.2.1 Fiber size dependence . . . 44
4.2.1.1 Correction to autocorrelation fitting equation . . . 46
4.3 Parallel continuous measurements . . . 48
4.3.1 Constant laser power . . . 48
4.3.2 Single triangular power ramp . . . 50
4.3.3 Linearly increasing triangular power raps . . . 51
4.3.4 Decouple reshaping and heating effects . . . 53
4.3.4.1 Reshaping . . . 54
4.3.4.2 Refractive index . . . 55
4.4 Possible changes to experimental procedure . . . 57
4.4.1 Centroid tracking . . . 57
4.4.2 Revised laser power ramps . . . 58
4.5 Preliminary results for continued investigations . . . 58
4.5.1 Rapid reshaping of long rods . . . 58
4.5.2 Laser induced particle release . . . 59

5 Conclusion and outlook **61**
5.1 Summary and conclusion . . . 61
5.2 Outlook and future applications . . . 62

Bibliography **64**

A Detailed measurement data from Section 4.3 **72**

B Second argument against desorption of CTAB **74**

List of Figures

1.1 A photograph of vividly colored windows in Basilica of the Sagrada Família in Barcelona. The colors are due to scattering and absorption of colloidal metallic particles supporting localized surface plasmon resonance (LSPR), which are incorporated into the glass during fabrication. 2

2.1 An illustration of a localized surface plasmon resonance of the dipole mode. The conduction electron cloud is affected by the electric field to start oscillating. Since the frequency of the field matches the LSPR frequency a collective resonant oscillation is induced. 8

2.2 Extinction cross section spectra calculated using quasi-static approximations for a range of spherical gold particles with increasing diameter excited by unpolarized light. For increasing diameter, the peak is red-shifted and broadened. It is also important to note the increased extinction at smaller wavelengths corresponding to damping from interband transitions of electrons in the nanoparticle. The inset figure illustrates the increasing maximum of the extinction cross section for increasing size of the sphere. . . 11

2.3 Normalized extinction cross section spectra calculated using quasi-static approximations for spheroidal gold nanorods, with a fixed width (40 nm) and increasing length, excited by unpolarized light. The long axis of the rod is assumed to be oriented perpendicular to the propagation direction of the light. The LSP resonance splits into two distinct resonances that are interpreted as a transverse LSPR peak constant at around 525 nm and a longitudinal peak that is red-shifted as the length of the rod is increasing. The inset figure illustrates the increasing maximum of the extinction cross section for increasing the length of the rod. 12

2.4 A qualitative illustration of the Ray optics model for an optical tweezers setup trapping a large transparent dielectric particle. The particle will refract the two light beams that have the wave vectors k_1 and k_2, which will give rise to the optical forces F_1 and F_2. The resulting force will direct the particle to the focus. Both the reflective and absorptive components of the light are here neglected. 14

2.5 Calculated spatial distribution of trapping forces in a laser beam with a paraxial Gaussian distribution affecting a gold nanorod of dimensions 80/40 nm. Here, the laser light has a power of 8 mW and a wavelength of 1064 nm and is focused by an objective with NA = 1.4. The scattering (F_{scat}) and gradient forces (F_{grad}) are presented separately in the left and middle graph. The figure to the right represents the total optical force. For this particular parameter set a stable 3D trap is generated. 16

2.6 Calculated spatial distribution of trapping forces in a laser beam with a paraxial Gaussian distribution affecting a gold nanorod of dimensions 80/40 nm. Here, the laser light has a power of 8 mW and a wavelength of 660 nm and is focused by an objective with NA = 1.4. The scattering (F_{scat}) and gradient forces (F_{grad}) are presented separately in the left and middle graph. The figure to the right represents the total optical force. For this particular parameter set no stable 3D trap can be generated resulting from too high scattering at this wavelength. 17

2.7 Calculated optical torques (a) as well as rotation frequency (b) for a nanorod with dimensions 80/40 nm within the quasi-static regime. For this particular nanorod the optical torques from absorption and scattering are almost equal. 21

3.1 A generic optical tweezers setup. A laser is through the use of a lens pair expanded to an appropriate size and collimated (to parallel rays). Thereafter, another lens pair denoted as beam steering will enable movement of the optical tweezers with respect to the sample. Hereafter, the beam is introduced into the optical path of the microscope by a dichroic mirror or a beamsplitter. After the microscope objective and trap, the light from the laser will be collected into a position detection system. Since dichroic mirrors are used, the microscope can be used for imaging in parallel with the trap. . . 24

3.2 A Keplerian telescope where two lenses are separated by their focal lengths. The telescope is expanding the width of the laser beam by a magnification factor of M from h_1 to h_2 through the relation $M = \frac{h_2}{h_1} = \frac{f_2}{f_1}$. 25

3.3 An illustration of the setup realized in this project combining an optical trap with instrumentation for spectroscopic measurements as well as autocorrelation analysis. Collimated laser light is circularly polarized using a sequence of two waveplates and then guided to the objective with a beamsplitter. Dark-field illuminated white light and laser light is scattered by the trapped nanoparticle and collected by the objective. The scattered laser light will be guided by a beamsplitter (70T/30R) to an APD, which creates a signal that is analyzed in an autocorrelator. The scattered white light is passed to a spectrometer after the laser light has been filtered away. 26

3.4 Photographs of the setup described in the text. The left picture shows the setup of the entire system from behind the microscope, and the most important parts of the setup have been marked for clarity. The inset image displays the mirror-waveplate configuration that directs and polarizes the light. 27

3.5 Measured laser power at the sample plane after the objective, depending on output laser power. A linear model is fitted to the data and yields a dependence according to $y = 0.019824x + 0.087373$. 28

3.6 A polarization ellipse where the amplitude of the two polarization directions are assumed to be equal ($E_{0x}^2 = E_{0y}^2 = 1$). The angle ψ defines the angle between the major axis of the ellipse and the x-axis and also between the minor axis and the y-axis, and a and b are the lengths semi-major and semi-minor axis. 29
3.7 Illustration of the setup used to correct for the phase shift induced by the beamsplitter, as the laser light is focused at the sample plane. A half-wave plate in sequence with a quarter-wave plate is used to continuously probe the Poincaré sphere to find the combination of three phase shifts that add up 90 degrees (the F denotes the fast axis). A polarizer and power meter together are employed to check the outgoing polarization state of the laser by measuring the major and minor axis of the polarization ellipse. In the figure for simplicity we also display the xy-projection of the polarization state. . . 31
3.8 Extinction spectra together with SEM images of the corresponding particles. The dashed line in the spectral plot corresponds to the 660 nm wavelength of the trapping laser light. The larger, stably trapped, NR02 (blue) has a spectral shape that is suboptimal for our investigations because of the large overlap between the two LSPR. NR07 (red) has a very pronounced longitudinal LSPR; however, its small size makes it difficult to trap. NR14 (green) combines the two advantageous properties of the prior two particles; stable trapping characteristics and a rather distinct longitudinal LSPR. Hence, NR14 is the particle utilized in this study. 32
3.9 Selective etching of nanorods in solutions through the process of anisotropic oxidation. a) Extinction spectra taken before and after the etching process. The longitudinal LSPR blue-shifts from 673 nm to 625 nm. This indicates a shortening of the length of the rod and a decreased aspect ratio. b) SEM images taken before and after the etching process also show a shortening of the gold rods. Before the process the particles have the dimension $115 \pm 7/65 \pm 4$ nm, and after $108 \pm 7/65 \pm 5$ nm. 34
3.10 In dark-field spectroscopy, light is passed through a dark-field condenser and incident on the nanostructure of interest at a high angle. Light scattered at an angle inside the collection cone defined by the numerical aperture of the objective will be collected. The obliquely incident illumination light will, however, be excluded from the detection since it is outside detection cone of the objective. Hence, the criteria for DF illumination becomes $\mathrm{NA_{obj}} < \mathrm{NA_{cond}}$. 35
3.11 Two spectral measurements used to calibrate the final single particle scattering spectrum. The blue graph represents the white light spectrum from the excitation light used in the illumination and spectroscopic ray path of the setup. The spectrum is approximately Gaussian and has an intensity maximum around 690 nm. The green curve displays the background spectrum with the laser turned off. It contains significantly more noise than the white signal owing to the much lower count rate of the signal, making shot noise more pronounced. 36

3.12 Raw data spectrum (blue), background spectrum containing self-fluorescence (light blue) and calibrated spectrum (green) for a single measurement. The focused laser beam is producing autofluorescence radiation from the glass slide, which is strong enough to distort the measured DF scattering spectrum. Therefore, spectra for a laser power sweep with an empty trap are recorded to create a library of background signals for different laser powers, which can continuously be subtracted for the current trapping power. The dip in the spectrum around 660 nm is a result of the notch filter blocking these wavelengths of light in the optical path. 37
3.13 Normalized DF scattering spectrum from a trapped rotating nanorod. The energy range that is blocked by the notch filter is deselected. The spectrum is fitted by a bi-Lorentzian model function with a linear interband transition correction term. The fit is shown in yellow. The three components to the fit are seen in green. 39
3.14 Triangular power ramp schemes that are utilized to study the long-term dynamic heating and reshaping effects of trapped particles. A single triangular ramp (blue), and consecutive triangular ramps with a linearly increasing maximum (green). 40

4.1 Data recorded with the CMOS camera for a trapped particle. a) and b) give position distributions in the x- and y-directions (in units of pixels on the CCD of the camera). These distributions are fitted with good agreement to Gaussian distribution curves. In c) and d) power spectra in the x- and y-directions are displayed together with fitted Lorentzians. From the fit the corner frequency is determined, which can be used to estimate the trapping stiffness. 42
4.2 Trapping stiffness in the x- and y-directions determined for a particle trapped at powers that are linearly increasing from 3.9 to 6.85 mW in six steps. The stiffness is approximately linearly increasing with increasing laser power. It is noted that the y-direction stiffness is consistently slightly larger than the x-direction stiffness. This is attributed to a polarization state of the laser that is deviating a bit from perfectly circular polarization, resulting in a lower trapping stiffness in the direction of the major axis of the polarization ellipse. 43
4.3 Autocorrelation signals from scattering of a rotating nanoparticle recorded using fibers with a small (62.5 μm) as well as a large (400 μm) core diameter. For the thick fiber the autocorrelation is oscillating around $C(\tau) = 0$ whereas in the thin fiber case the signal is pushed up into the upper right quadrant of the coordinate system, oscillating while it is decaying close to $C(\tau) = 0$ as the lag time increases. The lines connecting the data points serve as guides for the eye. 45

4.4 Two different fiber core diameters and thus collection volumes. Schematic illustrations for the fiber size with respect to translational motion of the nanorod (a and c). Images of fiber spot as laser light is coupled in from the back of the fiber (b and d). The scale bar in these two images is $2\,\mu$m and the diameter of the collection area can hence be estimated to $8.9\,\mu$m for the large fiber and $1\,\mu$m for the small. For the large fiber the translational motion in the trap will always be contained within the sensitive region. However, for the small fiber the translation will at times move the particle outside the detection region and hence lead to an intensity oscillation, characteristic to the translational Brownian motion. It should be mentioned that the apparent size difference between the collection area and the particle is not to scale. The size of the particle is strongly increased for the sake of the illustration. 46

4.5 Data from autocorrelation of scattered light collected with a thin fiber from a rotating particle and fitted with the two different models, the herein proposed Eq(4.1) as well as the previous Eq(2.34). From these two model functions it is seen that the first one (red curve) fits the measured data to a much higher degree, with $R^2 = 0.9994$, than the second (green curve) that has a $R^2 = 0.9628$. 47

4.6 A trapped rotating nanorod in constant laser power tweezers. The figure shows time evolution of the four parameters; longitudinal (a) and transverse (b) LSPR peak positions as well as rotation frequency (c) and calculated temperature (d). A continuous blue-shift of the longitudinal, red-shift of the transverse LSPR, as well as decrease in the rotation frequency and temperature is observed. 49

4.7 A trapped and rotating nanorod during a single high triangular laser power ramp. For the particle longitudinal LSPR peak (a), rotation frequency (b) and surrounding medium temperature (c) are extracted from the DF scattering spectrum and autocorrelation signal. A dip in the LSPR peak position at the time of the laser ramp is observed and followed by a large irreversible spectral shift. The rotation frequency and temperature both reach a crest as the power is ramped, and are thereafter stabilized on values lower than at the start of the experiment. 51

4.8 Data obtained during continuous measurements on a trapped and rotating nanorod when applying several triangular power ramps with linearly increasing maximum power. Displayed are the longitudinal (a) and transverse (b) LSPR peak shifts during the experiment, together with rotation frequency (c) and estimated temperature (d). As with the previous experiments the long-term spectral trend is indicating continuous reshaping of the trapped rod, with blue- and red-shift respectively of the longitudinal and transverse peak. During the laser ramps both peak exhibit blue shift, again indicating lowering of the RI due to photothermal effects. The rotation frequency and estimated temperature also follow the ramps to a high degree. 52

4.9 Illustration showing how the reshaping and temperature LSPR peak shifts can be decoupled in the triangular power ramp experiments. Figures a) and c) show longitudinal peak shift as displayed in Figures 4.7a) and 4.8a) (blue data points) together with an estimate of the reshaping induced peak shift (red line). Once the peak shift from reshaping is approximated this can be subtracted from the total peak shift, thus, obtaining a measurement of the peak shift induced only by the change in refractive index due to increased laser heating. This is done and displayed for a single high power triangle ramp (b) as well as the linearly increasing triangular ramps (d). 53

4.10 Values for refractive index plotted against temperature. The red lines correspond to an experimentally obtained expression for the refractive index of water derived in reference [76]. Blue data points are offset-corrected estimations of the change in refractive index of the surrounding from the heating attributed LSPR peak shift, plotted against the calculated surrounding temperature. These plots are generated for the single high power triangular laser ramp (a) and the linearly increasing laser power ramp (b). For b), the slope of the estimated heating induced refractive index change corresponds very well to the experimentally measured values for the refractive index of water at varying temperature. For a) most of the measured data points (marked with red dashed lines to guide the eye), the slope corresponds well to the red curve. However, there is a passage (dashed blue line) that exhibits a different slope. This indicates that the RI properties of the medium here are different, possibly owing to a phase change of the environment. The arrows are indicating the temporal direction of the measurement. 56

4.11 Four scattering spectra taken of a long nanorod immobilized on the substrate. At time $t = 0\,\mathrm{s}$ laser illumination is turned on at the power of 3.9 mW. During the following 19.5 seconds there is a continuous slight blue-shift of the longitudinal LSPR peak. Thereafter, at $t = 20.86\,\mathrm{s}$ something initializes a process where rapid peak shift of about 150 nm is accompanied with a decrease in the integrated scattered intensity. . . 59

4.12 High-speed image sequence taken during a light induced particle release from the bottom surface of a sample cell. At time $t = 0$ the laser illumination is started, and in the following two frames the particle is seen to be released and pushed away from the substrate and from focus by the radiation pressure of the laser light. It is thereafter free in solution and can be trapped and manipulated as previously described. 60

5.1 A schematic illustration of a proposed measurement and drug injection system. In an upright microscope configuration functionalized or drug-carrying gold nanorods are immobilized on the top surface in a microfluidic channel and can be released at will with a tightly focused laser beam. After being released, a particle can be rotated as it is approaching a cell, which has been trapped at the bottom surface of the channel. The cell could be immobilized momentarily by nanoscopic plasmonic tweezers, which are excited in a total internal reflection configuration. As the nanoparticle reaches the cell, it can be optically injected through the cell wall. The cell can be studied for as long as required and thereafter be released. 64

A.1 Examples of detailed measurements for particle in the constant laser power experiment in Section 4.3.1. Measured autocorrelation data together with a fit to the model function (a) and recorded DF scattering spectra together with a fit (b). In the figures the extracted parameter of important are presented. 72

A.2 Examples of detailed measurements for particle in the single triangular power ramp experiment in Section 4.3.2. Measured autocorrelation data together with a fit to the model function (a) and recorded DF scattering spectra together with a fit (b). In the figures the extracted parameter of important are presented. 73

A.3 Examples of detailed measurements for particle in the consecutive triangular laser ramps with linearly increasing maximum experiment in Section 4.3.3. Measured autocorrelation data together with a fit to the model function (a) and recorded DF scattering spectra together with a fit (b). In the figures the extracted parameter of important are presented. 73

1

Introduction

The interaction between light and matter is something that has interested and eluded scientists for centuries and has truly helped shape modern physics. Many of the theoretical descriptions of optical properties for bulk solids were performed over a hundred years ago, and can be described in classical or semi-classical models. An illustrative example of this is the Lorentz model for an electron bound to an isolated atom. Here, a dipole oscillator model can be derived from three simple approximations; classical, harmonic, and Born-Oppenheimer approximation. By simply adding N atoms and using this model we can describe general optical properties such as polarizability, absorption, scattering, and refractive index for bulk solids to a first approximation [1, 2].

It is fascinating that despite the age of the field and the sometimes rather elementary theory describing it, topics researched and interesting discoveries have far from stagnated. During this thesis light-matter interactions with gold nanorods have been investigated. These structures are of utter importance in the field due to their highly interesting properties described in plasmonics [3, 4].

1.1 Plasmonics

Since the beginning of the 20^{th} century the study of plasmonics has evolved, analyzing how electromagnetic fields can interact with and be confined within matter with the dimension of, or smaller than, the wavelength of the incident field. It is a fundamental fact from nanotechnology that reducing at least one dimension of a structure to the nanoscale will drastically alter the electronic properties such as the density of states or spatial length scale of the electronic motion since these are now governed by surface effects. If all three dimensions of a noble metallic structure shrink to the nanoscale, the particle will support an effect known as localized surface plasmon resonance (LSPR). This is an effect that leads to strongly enhanced scattering and absorption at specific wavelengths, producing rich colors, especially for gold and silver nanoparticles where the resonances fall within the visible region of the electromagnetic spectrum.

Long before the physics of plasmonic was understood and without knowledge about the underlying processes, metallic nanostructures in colloidal solutions were used to produce the vivid colors in the magnificent stained windows of Gothic churches. In Figure 1.1 an example from the Basilica of the Sagrada Família in Barcelona is shown, illustrating the potential beauty of these creations. At a lecture for the Royal Society in London in 1857, which later led to the publication of reference [5], Faraday recognized

Figure 1.1: A photograph of vividly colored windows in Basilica of the Sagrada Família in Barcelona. The colors are due to scattering and absorption of colloidal metallic particles supporting localized surface plasmon resonance (LSPR), which are incorporated into the glass during fabrication.

that the colors in the church windows were due to metallic nanoparticles. In 1908 another integral step in the early development of plasmonics was taken by Mie when solving Maxwell's equations for scattering and absorption of spherical particles smaller than the wavelength of light [1, 6]. Since Mie's results and until today these small particle effects have been studied extensively for a wide range of particle materials and shapes and have been found useful in a wealth of areas, such as sensing [7], medicine [8, 9], data storage [10], solar cells [11] and many more.

A direction of study not mentioned in the list above for nanoparticles supporting LSPR has been taken in this thesis. It involves a highly focused laser beam in the configuration of so-called *optical tweezers*. Using the linear momentum as well as angular momentum of laser light, nanostructures can be trapped and rotated in the focus of the laser beam.

1.2 Optical tweezers

It has been widely known since the development of the electromagnetic theory that light waves can be associated with linear momentum [12]. In 1970 Ashkin published a seminal paper [13] illustrating that the momentum of a focused laser beam could be used to accelerate and trap micron-sized particles. Using this effect a group at AT&T (Bell) Laboratories led by Ashkin constructed a "single-beam gradient optical trap" by focusing a laser beam through a high numerical aperture[1] lens [14]. This idea caught

[1]Numerical aperture is a dimensionless quantity that describes how large the collection cone of a lens or objective is. $NA = n_{\mathrm{m}} \sin\theta$ where n_{m} is the refractive index of the surrounding medium and θ is the largest angle that the objective can collect light from.

hold in the scientific community and later also in industry, and the device is today referred to as optical tweezers [15]. The beauty of the optical tweezers is that through a gradient force interaction the radiation pressure from the light is counteracted, and objects can be stably trapped in three dimensions.

The particles originally used in optical tweezers were around micron-sized dielectric particles. The trapping and manipulation of these has widely been utilized to study positions, forces and torques to an impressive precision. Optical micro-manipulation has brought advances and applications in a variety of fields such as cell and molecular biology [16, 17], atomic physics [18][2] and micro-machining [19]. From the invention of the optical tweezers and throughout the coming years, it was widely believed that three-dimensional trapping of metallic particles was not possible. Due to increased scattering from the reflective surface of the metallic particle, radiation pressure was thought to always dominate over the attractive gradient force, hence effectively pushing the particle away from the trapping region [20]. On the contrary, it was found in 1994 that metallic nanoparticles can be trapped in 3D using optical tweezers if the particles are in the Rayleigh size regime (the size of the particle d is much smaller than the wavelength of light λ, i.e. $d \ll \lambda$) and the trapping laser light is far from the LSPR of the particle. Moreover, the gold particles used in their study even demonstrated a sevenfold increase in trapping stiffness compared with dielectric particles of equal size [21].

Since the paper by Svoboda and Block in 1994 optical manipulation of metallic nanostructures have continued and is now its own subfield where plasmonics meets optical manipulation. The size range for particles that are possible to trap in 3D has been well expanded [22] and many different shapes including nanorods have been investigated [23, 24]. Also, studies to extract information about torque and Brownian motion for rods trapped with linear polarization have been performed and will prove to be of importance to the work performed in this thesis [25]. The most recent advances in this field are presented by the excellent review in reference [26].

Although certain types of particle might not be possible to trap in 3D it does not mean they are rendered uninteresting to study. At Chalmers, such structures have been investigated extensively over the years, in a sample configuration where the radiation pressure is counteracted by a glass slide instead of the z-direction gradient force. Hence, the particle is trapped in two dimensions by the xy-direction gradient forces and is free to be manipulated in the plane of the glass slide [27].

1.2.1 Optical rotation

Just as a photon carries linear momentum, if circularly polarized, light also carries a spin angular momentum (SAM). As the photon interacts with a particle it will transfer some or all its SAM, which will be translated into a light-induced torque on the structure it is incident on. Already in 1936 this effect was demonstrated to induce a macroscopically detectable angular displacement of a birefringent waveplate [28]. In this case, the torque

[2]The Nobel prize in Physics was in 1997 awarded to Steven Chu, Claude N. Cohen-Tannoudji, and William D. Phillips for the cooling and trapping of single atoms with laser. The reference is a transcript of the address held by Phillips on the occasion of the award ceremony.

arises from phase conversion of the incoming circularly polarized light into transmitted elliptical light. The fundamental observation in the early part of the last century did not at the time result in much attention for optically induced torques. However, the interest was rekindled as optical tweezers grew more common, and studies on optical rotation and torque from light on birefringent microscopic particles were published [29]. Since then, a wide range of dielectric structures have been studied as candidates for rotary motors driven by optical fields [30, 31][3]. Just as in the general field of optical tweezers it was soon realized that the plasmonic properties of metallic nanoparticles made them well suited for optical rotation schemes. The first publication on this was produced by the Bionanophotonics division at Chalmers in 2010 [33].

In the case of trapped metallic nanostructures the optical torque can originate from either solely absorption or a combination of absorption and scattering of photons, depending on the shape of the particle. If the particle is small, for a spherically (or cylindrically) symmetric particle, the torque will be solely due to absorption. For a rod or shapes with different rotational symmetry, scattering driven torque will dominate over a comparably small absorption contribution [34]. Through this interaction, appropriately sized and shaped gold particles can be made to spin with extraordinarily high rotation frequencies up to several kHz for nanospheres [35] and several tenths of kHz for nanorods in water [36]. The speed of the rotation is dependent on several variables; however, the final rotational frequency will be limited by the frictional torque from the viscosity of the media the particle is spinning in. The optically trapped rotating gold nanorod is a prime candidate for use as a nanoscopic rotary motor and transducer of torque. The system holds promise for applications within numerous fields, ranging from nano/microfluidic flow control and nanorobotics to sensing and DNA manipulation, as discussed in reference [36].

Apart from the transferred angular momentum, light will cause photothermal effects such as substantial heating of the nanoparticle. Heating will be present for both nanospheres and nanorods, yet slightly more distinguished in the spherical case since the optical torque will be absorption dominated. This is in contrast to the nanorod case where the scattering torque will play a significant role and absorption can be limited. Since the viscosity of liquids in general and water in particular is lowered as temperature increases the heating of the particle will influence the rotation frequency. In 2013 it was shown that when laser light incident on a nanoparticle fixed to a substrate with sufficiently high power (comparable to powers used in the rotation experiments mentioned above), the surrounding water can form a nanoscopic vapor bubble around the particle [37]. This would induce a significant lowering of the viscosity in the vicinity of the particle, and it is hypothesised that vapor bubble formation could explain some specific high laser power results of previous rotation experiments [35, 36].

[3]The studies mentioned above are all performed in water, which is the medium where nanoscopic rotary motors are most applicable. However, as a side note it can be noted that dielectric particles have been made to rotate at incredible frequencies up to 5 MHz in vacuum [32].

1.3 Reshaping

It is well known that the atoms in gold nanoparticles are substantially more mobile than their bulk counterparts [38]. The diffusion process governing this movement will lead to gold atoms migrating from high curvature areas to lower curvature areas. For a nanorod this essentially results in a migration process where the rod becomes shorter and wider, eventually forming the thermally stable sphere.

Experiments to study the reshaping effects from thermal heating of immobilized nanorods have been conducted [39]. In this study, nanorods were heated to a temperature of 250 °C (well below the melting temperature of gold [40]) and demonstrated to reshape to a sphere within an hour. Furthermore, reshaping of immobilized nanorods under pulsed laser illumination has been thoroughly studied, and a theory for this phenomenon has been produced. The theory is based on surface diffusion of gold atoms from high to lower curvature areas on the nanorod [41]. Lastly, the attempts to use continuous wave (CW) lasers to study reshaping effects in gold nanorods have been limited. The first main study on this topic was presented as late as 2014, although this is the most common type of laser used in both optical trapping as well as photo-thermal therapy [42][4].

The photothermal effects of particles in optical traps have been used to drive certain chemical surface reactions of the trapped nanorod, which in turn leads to reshaping [43]. However, reshaping solely due to photothermal effects of rods inside optical tweezers has not been studied more than in passing (i.e. supporting information of [25]). The understanding of how reshaping and heating effects are affecting trapped and rotating nanorods is a necessary step towards a complete picture of the ultrafast nanoscopic rotary motors studied in this thesis. In order to reach the proposed high end application of this platform, reshaping and heating effects of the particle inside the trap are essential to study and control.

1.4 Spectroscopy

Spectroscopic measurements relate intensity of radiation to the wavelength, energy, or frequency of the incident wave. For plasmonic nanoparticles, spectroscopy is a valuable tool that allows researchers to probe the LSP resonance. Also, since the LSPR depends strongly on particle shape, size, and environment, with spectroscopic measurements of the LSPR these properties can be analyzed. As mentioned above, there is a whole subfield that has been developed by using the LSPR of plasmonic nanoparticles as sensors [7], with devices sensitive enough to resolve single molecule binding [44, 45]. There are certainly many different single nanoparticle spectroscopic techniques, and in this work the method of dark-field scattering spectroscopy has been utilized [7].

[4] It should be mentioned that photothermal reshaping with CW lasers has been touched upon in earlier works, it is for example mentioned in the supporting information of reference [10]. Yet, to the best of the author's knowledge the study in reference [42] is the first study with this effect as its main focus.

1.5 Purpose and aim

For several years, optical rotation of plasmonic nanoparticles has been one of the ongoing research projects at the Bionanophotonics division at Chalmers University of Technology. Their research in the field has led to several insights regarding both the underlying physics as well as possible applications of the system [26, 33, 35, 36].

This master thesis can be seen as a continuation of the work done previously in the group. The project was initialized with the construction of a fully functional experimental setup where optical trapping and rotation experiments can be continued. The purpose for this new system is to broaden the base of possible experiments that can be performed on the optically driven rotary motors, by including instrumentation enabling spectroscopic measurements. The construction of the experimental setup can be seen as the first of two major sub-projects of the thesis.

The second sub-project commenced as the setup including the optical trap and the appropriate measurement instrumentation was constructed, functional and characterized. The aim was to use this setup to study the rotational and plasmonic properties of gold nanorods in relation to the photothermal effects induced by the laser light, and to perform spectroscopic measurements to probe the local environment around the particle during trapping and rotation. Through continuous tracking of plasmon resonance shifts and rotational dynamics of the trapped particles, the aim was to be able to resolve a number of important effects. These include changes in the refractive index of the water surrounding the trapped nanoparticle, nanoparticle reshaping effects, and bubble generation, and how these effects affect the performance of the rotary motors. The results will potentially shed light on thermal processes on the nanoscale and will be useful in evaluating the applicability and performance of nanorod motors for different applications. As recent as the end of last year a paper was published discussing the spectral changes of an optically trapped nanosphere due to temperature variation, illustrating that studies such as this one are currently of interest [46].

2

Theory

In the introduction, the context of the study that will be conducted was established. To expand on the topics presented there it is crucial to present the theory necessary to deepen the understanding of the topic at hand. Thus, the following chapter will present the theory and physics related to plasmonic nanoparticles, optical tweezers systems, and optical rotation of particles. The field of plasmonics has become well established over the course of the last century and a wealth of theory has been produced to describe observed properties and process. Hence, the theory presented in the chapter should be seen as a summary of concepts important for the thesis at hand rather than in-depth derivations of the formulas. Interested readers who wish to deepen their knowledge, or those who are completely new to the subject, are referred to the following textbooks [1, 3] or excellent reviews on the topics [4, 7, 26]. As the significant part of the theory has been presented, the formulas below are used to perform some calculations that are meant to illustrate the physics of the system of interest for the thesis.

2.1 Localized surface plasmon resonance

A plasmon is the collective oscillation of the conduction electrons in a material, excited by an electromagnetic field. The oscillation will be induced most strongly when the wavelength of the electromagnetic field is matching the plasmon resonance wavelength in the material. Materials that support plasmon oscillations have a negative real and a near zero imaginary part of the dielectric function [7]. If a thin layer of plasmonically active material is placed on a material of positive permittivity and the conduction electrons in this surface layer are driven by an electric field, a surface plasmon resonance (SPR) is induced. These oscillations are indeed interesting; however, not further discussed in this thesis, for more on this see for example [3]. On the other hand, if the material that supports plasmon resonance is in the form of a nanoparticle the collective oscillation of the conduction electrons will be characterized as a localized surface plasmon resonance (LSPR). In Figure 2.1 a schematic illustration is presented of the LSPR induced by an oscillating incident field.

The localized surface plasmon resonance is found to be strongly dependent on the shape of the resonant particle, and for a nanorod the single resonance in the spherical case is split up into two distinctly separate plasmon resonances. These two resonances are corresponding to resonant excitations of the conduction electrons in the longitudinal as well as transverse direction of the rod. The transverse LSPR peak will show a resonance

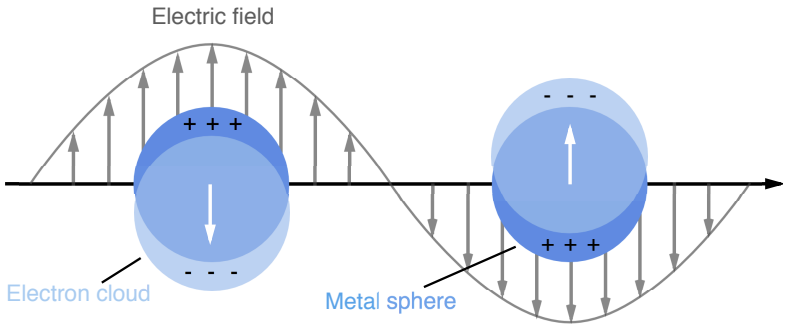

Figure 2.1: An illustration of a localized surface plasmon resonance of the dipole mode. The conduction electron cloud is affected by the electric field to start oscillating. Since the frequency of the field matches the LSPR frequency a collective resonant oscillation is induced.

in the same wavelength range as the spherical particle ($\sim 520\,\text{nm}$ for gold), whereas the longitudinal LSPR peak will be red-shifted and strongly dependent on the aspect ratio of the nanorod.

When light matching the plasmon resonance wavelength is incident on a nanoparticle the scattering and absorption of this light is strongly enhanced. However, the properties of the LPSR in a particle, such as plasmon resonance wavelength, mode of oscillation, and damping characteristics, can further vary widely depending on other particle properties such as size and material but also with the surrounding of the particles. For example, an increased refractive index of the surrounding medium will lead to a reduced restoring force on the plasmon oscillation, which in turn will result in a red-shift of the plasmonic peak.

2.1.1 Quasi-static approximation

Under the assumption that the particle of interest is considerably smaller than the wavelength of the incident light ($d \ll \lambda$), one can to a first approximation describe the particle in the so-called *quasi-static approximation*. Here, the optical properties of the particle are characterized by their induced dipole moments and spatial variations of the field across the nanoparticle is neglected. The derivations and formulas in the following two sections are mainly summarized from references [1, 3] and the treatment can be regarded as accurate for nanostructures with dimensions below 100 nm. For particles larger than this limit a more rigorous electrodynamic description is needed (not discussed further here), which is captured in Mie theory for spherical particles and in Mie-Gans theory for spheroidal particles.

By visualizing the plasmon oscillation in the nanoparticle as a driven damped harmonic oscillator the following equation can be set up for the motion of the collective electron oscillation

$$\ddot{x} = \frac{q}{m}E(t) - \omega_0^2 x - \gamma\dot{x}, \tag{2.1}$$

where $E(t) = E_0 \cos\omega t$ is an oscillatory electric field, q and m are the charge and mass of the displaced oscillator (proportional to the number of changes in the nanoparticle), ω_0

the resonance frequency, and γ the damping rate. By solving this differential equation we obtain an expression for the induced dipole moment as

$$p(\omega, t) = \frac{q^2/m}{\omega_0^2 - \omega^2 - i\omega\gamma} E(t), \tag{2.2}$$

which we identify to be on the form of a Lorentzian function, where the peak position is related to the resonance frequency and the width of the peak is related to the damping rate of the oscillation.

2.1.1.1 Spherical case

The most simple case to consider is without a doubt an isotropic homogeneous sphere of radius a with the dielectric function $\varepsilon(\omega)$ that is located in an isotropic and non-absorbing medium with the dielectric constant ε_m. By solving the Laplace equation for the electrostatic case and applying appropriate boundary conditions one can after some manipulation (presented in detail in [3]) arrive at an expression for the induced dipole moment for the sphere by a driving electric field $\mathbf{E}$ as

$$\mathbf{p} = 4\pi\varepsilon_0\varepsilon_\mathrm{m} a^3 \frac{\varepsilon(\omega) - \varepsilon_\mathrm{m}}{\varepsilon(\omega) + 2\varepsilon_\mathrm{m}} \mathbf{E} = \varepsilon_0\varepsilon_\mathrm{m}\alpha(\omega)\mathbf{E}, \tag{2.3}$$

where $\alpha = 4\pi a^3 \frac{\varepsilon(\omega)-\varepsilon_\mathrm{m}}{\varepsilon(\omega)+2\varepsilon_\mathrm{m}}$ is defined as the polarizability of the sphere, which is on the same form as the Clausius-Mossotti relation. From the appearance of the expression for $\alpha(\omega)$ it is realized that as $\varepsilon(\omega) \to -2\varepsilon_m$ the polarizability will reach a resonance condition and the quantity will become very large.

Under the quasi-static approximation the interesting and experimentally measurable properties of scattering and extinction cross sections for a particle can be derived as the corresponding properties for a point dipole. These read

$$\sigma_\mathrm{scat} = \frac{\omega^4 n_\mathrm{m}^4}{6\pi c^4} \left|\alpha(\omega)\right|^2, \tag{2.4}$$

$$\sigma_\mathrm{ext} = \frac{\omega n_\mathrm{m}}{c} \mathrm{Im}\{\alpha(\omega)\}, \tag{2.5}$$

where n_m is the refractive index of the medium and c the speed of light. From these two equations, one can also reach the absorption cross section as $\sigma_\mathrm{abs} = \sigma_\mathrm{ext} - \sigma_\mathrm{scat}$.

2.1.1.2 Spheroidal case

The nanorods which are studied in most applications are of a capsule shape, also called a hemispherically capped cylinder. There has not yet been found any analytical solutions to the Laplace equation for this geometry. Therefore, we approximate the shape of the nanoparticle as a prolate spheroid with semi-major axis a and semi-minor axis b, a case that is solvable analytically. By then solving Laplace equation in spheroidal coordinates with appropriate boundary conditions for a particle with dielectric function $\varepsilon(\omega)$ in a medium with dielectric constant ε_m, we obtain a description on the same form as in

Equation (2.3) with the modification of separate polarizabilities of the longitudinal and transverse plasmon modes on a Clausius-Mossotti form as

$$\alpha_{\mathrm{j}}(\omega) = \frac{4\pi ab^2}{3P_{\mathrm{j}}} \frac{\varepsilon - \varepsilon_{\mathrm{m}}}{\varepsilon + \left(\frac{1-P_{\mathrm{j}}}{P_{\mathrm{j}}}\right)\varepsilon_{\mathrm{m}}}, \quad \mathrm{j} = \mathrm{L} \text{ or } \mathrm{T}, \tag{2.6}$$

where P_{L} and P_{T} are depolarization factors for the longitudinal as well as transverse direction of the spheriod, expressed in terms of the eccentricity $e = \sqrt{1 - \left(\frac{b}{a}\right)^2}$ by

$$P_{\mathrm{L}} = \frac{1-e^2}{e^2}\left[\frac{1}{2e}\ln\left(\frac{1+e}{1-e}\right) - 1\right], \tag{2.7}$$

$$P_{\mathrm{T}} = \frac{1-P_{\mathrm{L}}}{2}. \tag{2.8}$$

Just as in the spherical case it is from here possible to access the scattering as well as absorption cross sections. The difference between this system and the one described above is that we have polarizabilities for different oscillatory modes. For unpolarized or circularly polarized light that is incident on the spheroid along the direction of one of its axis these polarizabilities are decoupled from each other and adds linearly to the total polarizability. In the case where the long axis of the particle is orthogonal to the illumination light, the two polarizabilities are added without any scaling factors between them[1] as

$$\sigma_{\mathrm{scat}} = \frac{\omega^4 n_{\mathrm{m}}^4}{6\pi c^4}\left(|\alpha_{\mathrm{L}}(\omega)|^2 + |\alpha_{\mathrm{T}}(\omega)|^2\right), \tag{2.9}$$

$$\sigma_{\mathrm{ext}} = \frac{\omega n_{\mathrm{m}}}{c}\mathrm{Im}\{\alpha_{\mathrm{L}}(\omega) + \alpha_{\mathrm{T}}(\omega)\}. \tag{2.10}$$

It is for isotropic particles useful to construct a three dimensional matrix containing the polarizabilities of the three separate axes. As the axes of the spheroid are aligned with the Cartesian axes of the current coordinate system (e.g. incoming light interacting with the particle), the matrix that is often referred to as the polarizability tensor will be diagonal. The tensor can further be decomposed into a real and imaginary part according to $\boldsymbol{\alpha} = \boldsymbol{\alpha}' + i \cdot \boldsymbol{\alpha}''$.

2.1.1.3 MLWA correction

The equations discussed above are derived from a particle that can be assumed to be a point dipole with no spatial distribution, where electrostatics are enough to obtain the scattering and absorption characteristics. Since this is a strong assumption for particles larger than about 1% of the wavelength of light [47], a correction to the description is necessary and can be made in the so-called *Modified long-wavelength approximation* (MLWA) [48]. This theory accounts for two main effects that will alter the properties of

[1] This results from the fact that for illumination orthogonal to the long axis of the rod, one of the transverse directions is parallel with the k-vector of the illumination light, and hence the oscillation of the illumination light does not drive a plasmon oscillation in that transverse direction. If the illumination instead falls in parallel to the long axis of the rod, the plasmon oscillation in this direction is not excited and does not contribute to the cross sections. For an arbitrary angle in between, a scale factor for how much each mode is excited needs to be calculated. This is done in the supporting information of reference [36].

an actual particle compared to its point dipole description. The first one being radiative damping, that arises from the increasing emission of radiation from the induced dipole as the size of the particle increases. This leads to a decrease in the dipole oscillation, and broadening of the plasmon peak (i.e. increased plasmon damping). The second MLWA effect accounts for dynamic depolarization, which comes from the fact that the particle has a finite size and radiation emitted from different points in the particle will interfere and lead to a depolarization. MLWA is summarized in the expression for D that is multiplied with the polarizabilities derived above.

$$D = \left(1 - \frac{k_{\mathrm{m}}^2}{4\pi l_{\mathrm{j}}}\alpha_{\mathrm{j}} - \frac{ik_{\mathrm{m}}^3}{6\pi}\alpha_{\mathrm{j}}\right)^{-1}, \tag{2.11}$$

where $k_{\mathrm{m}} = n_{\mathrm{m}}k$ is the wavenumber in the medium, $l_{\mathrm{j}} = a$ or b is the semi-major or semi-minor axis of the spheroid and α_{j} is the polarizability in the L or T direction as derived in Equation(2.6).

2.1.1.4 Calculated cross sections

Using data for the dielectric function of gold measured by Johnson and Christy [49] and inserting that into the Equations (2.3) and (2.6) corrected with the MLWA as presented in Equation (2.11) the polarizability for spheres and spheroids can be estimated. These polarizabilies are entered into the expression for the scattering and extinction cross

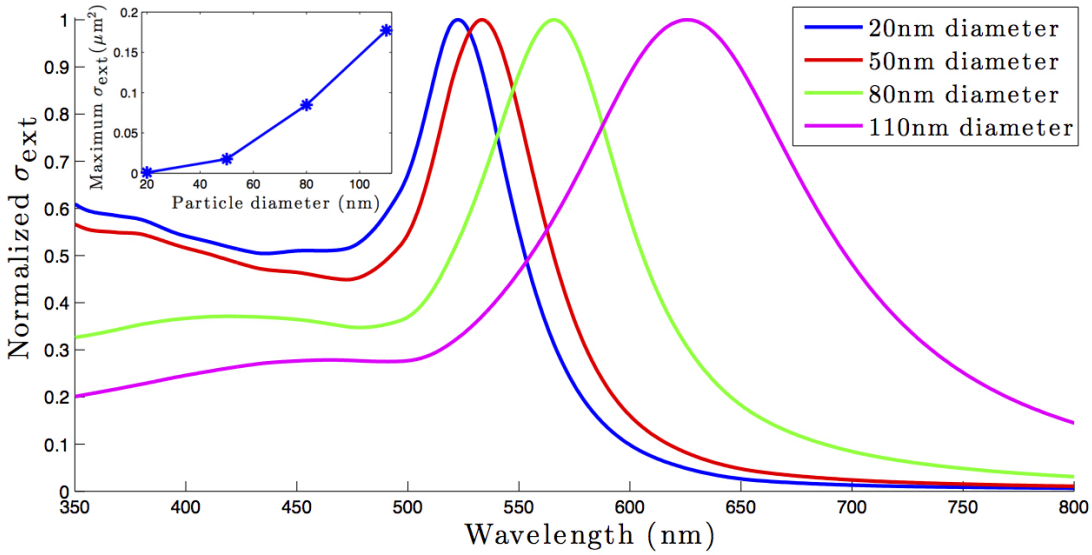

Figure 2.2: Extinction cross section spectra calculated using quasi-static approximations for a range of spherical gold particles with increasing diameter excited by unpolarized light. For increasing diameter, the peak is red-shifted and broadened. It is also important to note the increased extinction at smaller wavelengths corresponding to damping from interband transitions of electrons in the nanoparticle. The inset figure illustrates the increasing maximum of the extinction cross section for increasing size of the sphere.

sections as described in (2.4), (2.5), (2.9) and (2.10). In Figure 2.2 extinction spectra for different sizes of spherical particles, ranging from 20 to 110 nm excited by unpolarized light are displayed. The spectra are normalized to their maximum and the inset in the figure demonstrates the increase in maximum extinction cross section as the particle size increases. Most noticeable in this figure might be that the resonance is red-shifted and severely broadened for an increasing particle diameter. Furthermore, especially for smaller particles, we notice an increase of the extinction cross section for lower wavelengths. This stems from the fact that at energies above 2.5 eV (corresponding to a wavelength of 496 nm) the energy of the photons in the EM radiation are sufficient to excite electrons from the filled bands below the Fermi surface to higher bands above it. These transitions are called interband transitions and lead to increased damping and absorption in this energy range [3].

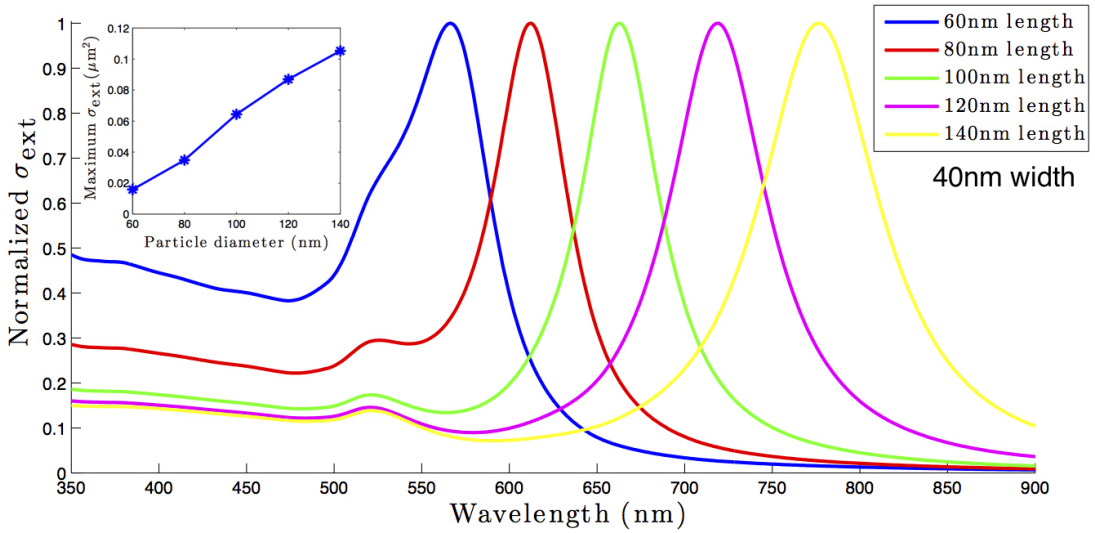

Figure 2.3: Normalized extinction cross section spectra calculated using quasi-static approximations for spheroidal gold nanorods, with a fixed width (40 nm) and increasing length, excited by unpolarized light. The long axis of the rod is assumed to be oriented perpendicular to the propagation direction of the light. The LSP resonance splits into two distinct resonances that are interpreted as a transverse LSPR peak constant at around 525 nm and a longitudinal peak that is red-shifted as the length of the rod is increasing. The inset figure illustrates the increasing maximum of the extinction cross section for increasing the length of the rod.

In the same manner, Figure 2.3 is displaying extinction cross section spectra generated for prolate spheroidal particles with a constant width of 40 nm and a length increasing from 60 to 140 nm, excited by unpolarized light. The long axis of the rod is assumed to be oriented perpendicular to the propagation direction of the light. The spectra are normalized and the inset displays the increasing maximum in extinction cross section as the length of the rod is increasing. As expected from the theoretical understanding of LSPR for spheroids as well as of nanorods two separate plasmon peaks are observed. One peak at around 525 nm corresponding to the transverse oscillation and one that is red-shifted and strongly dependent on the aspect ratio of the particle, which

corresponds to the longitudinal oscillation. We note that for increasing aspect ratio the transverse LSPR peak position, and also its magnitude is rather unaffected, whereas the longitudinal peak is linearly red-shifting and increasing.

2.2 Optical tweezers

The working principle for optical tweezers is elegantly simple: High intensity light will transfer some or all its momentum to a particle via elastic or inelastic collision and through this interaction exert a force on it. Optical tweezers will subject the particle to a force, which can be decomposed into a scattering force component (F_{scat}) and a gradient force (F_{grad}) component. The scattering force arises from scattering of photons against the particle, is proportional to the intensity of light and acts in the propagation direction of the laser light [50]. The gradient force arises from the fact that light polarizes atoms in the particle, which in turn experience a force in the gradient of the electromagnetic field [51]. Stable three dimensional trapping will essentially be obtained when the gradient force is larger than the scattering force. To achieve this microscope objectives with high numerical apertures are predominantly used since the strong deflection of light in these objectives will yield a higher intensity gradient and thus a stronger gradient force [50]. In the case of dielectric particles, the scattering is considerably smaller and stable 3D trapping can often be obtained. The situation for metallic nanoparticles is rather different since scattering and absorption are strongly enhanced close to the LSPR, increasing the scattering force which in turn decreases the trapping stability. Generally, this results in the fact that laser light that is detuned from the LSPR wavelength allows for 3D trapping of metallic particles, in contrast to close to resonant laser light that will push the particle away from the focus.

Normally, the direction of the gradient force is towards high intensity regions. However, for plasmonic particles the polarizability may change sign due to a change in phase of the dipole oscillation with respect to the incident field close to the LSPR. This will lead to the gradient force being attractive for light on the low-frequency (red) side of the LSPR peak whereas repulsive for high-frequency (blue) light [52]. This is a property that is important to consider when selecting particles to study.

For a particle with arbitrary size and shape the force acting on the particle from the optical tweezers can be calculated by integrating Maxwell's stress tensor over a closed surface containing the particle [53]. For most shapes and sizes this demands extensive calculations including solving EM fields in every point, which requires numerical calculations with for example FDTD. However, for some specific particle shapes, types and sizes some simplified models are sufficient.

Large dielectric particles in the Mie regime can be viewed as lenses that redirect photon momentum, resulting in a counter-force on the particle and hence a negative potential is created in the center of the trapping laser [54]. This model is referred to as the Ray optics model, and the concept is illustrated in Figure 2.4. For particles smaller than the wavelength and also for reflective particles the description based on a lensing effect breaks down. In the small particle regime the particle can be described solely

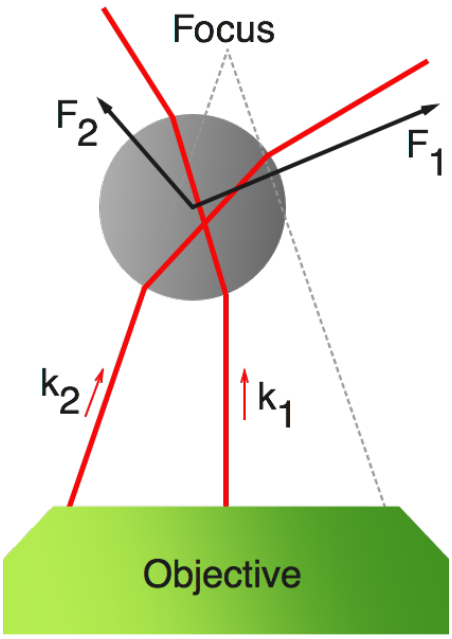

Figure 2.4: A qualitative illustration of the Ray optics model for an optical tweezers setup trapping a large transparent dielectric particle. The particle will refract the two light beams that have the wave vectors k_1 and k_2, which will give rise to the optical forces F_1 and F_2. The resulting force will direct the particle to the focus. Both the reflective and absorptive components of the light are here neglected.

by its induced dipole moments, just as in Section 2.1.1 for the polarizabilities, and the problem can be drastically simplified. The scattering and gradient forces can then be derived under the quasi-static approximation. Here, a Lorentz force model can be used to accurately describe the forces acting on the particle. When the dipole moment $\mathbf{p}$ and the electric field $\mathbf{E}$ are linearly related (as in the quasi-static regime and Equation (2.3)) the total force can be decomposed into its relevant components; namely, the gradient and scattering force, as

$$\mathbf{F}_{\text{grad}}(\mathbf{r}) = \frac{\varepsilon_0 \varepsilon_\text{m}}{4} \nabla \left(\mathbf{E}^*(\mathbf{r}) \cdot \boldsymbol{\alpha}' \cdot \mathbf{E}(\mathbf{r}) \right), \tag{2.12}$$

$$\mathbf{F}_{\text{scat}} = \frac{\varepsilon_0 \varepsilon_\text{m}}{2} \text{Im}\{\mathbf{E}^*(\mathbf{r}) \cdot \boldsymbol{\alpha}'' \cdot \nabla \mathbf{E}(\mathbf{r})\}, \tag{2.13}$$

where $\mathbf{E}(\mathbf{r})$ is the incoming electric field and * denotes the complex conjugate [55]. For a spherical particle, which has a scalar polarizability, the expression can be simplified further to

$$\mathbf{F}_{\text{grad}}(\mathbf{r}) = \frac{n_\text{m}}{2c} \alpha' \nabla I(\mathbf{r}), \qquad \mathbf{F}_{\text{scat}} = \frac{n_\text{m}}{c} \alpha'' \text{Im}\{\mathbf{E}^*(\mathbf{r}) \cdot \nabla \mathbf{E}(\mathbf{r})\},$$

where $I(\mathbf{r}) = \dfrac{\varepsilon_0 n_\text{m} c}{2} \left(\mathbf{E}(\mathbf{r}) \cdot \mathbf{E}^*(\mathbf{r}) \right)$. The same holds true also for a nanorod if its axes are aligned with the Cartesian axes of the incoming light since the polarizability tensor is then diagonal and can be separated into scalar components.

2.2.1 Optical force calculations

In the most common optical trap light is focused in a Gaussian beam. To estimate the optical forces of a nanoscopic metallic particle in a trapping potential, we will below conduct some simplified calculations within a paraxial Gaussian laser beam model. The spatial distribution of the electric field is, as in reference [56], modelled according to the function

$$\mathbf{E}(r,z) = \mathbf{E}_0 \sqrt{\frac{2}{\pi}} \frac{w_0}{w(z)} \exp\left[-\frac{r^2}{w(z)^2} + i\left(\frac{kr^2}{2R(z)} + kz - \phi(z) \right) \right], \tag{2.14}$$

where

$$R(z) = z\left[1 + \left(\frac{z}{z_0}\right)^2\right], \tag{2.15}$$

$$w(z) = w_0 \sqrt{1 + \left(\frac{z}{z_0}\right)^2}, \tag{2.16}$$

$$z_0 = \frac{\pi w_0^2 n_\mathrm{m}}{\lambda}, \tag{2.17}$$

$$w_0 = \frac{\lambda}{\pi \mathrm{NA}}, \tag{2.18}$$

$$\phi(z) = \arctan\left(\frac{z}{z_0}\right), \tag{2.19}$$

$$|\mathbf{E}_0| = \frac{2}{w_0}\sqrt{\frac{\mu_0 P}{\varepsilon_0 \pi}}. \tag{2.20}$$

Here, $R(z)$ is the radius of curvature of the beam front at z and $w(z)$ is the radius at which the field intensity has decreased to $\frac{1}{e}$ of its axial value. z_0 is the distance along the z-axis at which the cross sectional area of the beam is doubled, w_0 is the width of the beam at the focus, $\phi(z)$ is the so-called Gouy phase accounting for increased apparent wavelength near the focus and $|\mathbf{E}_0|$ is the magnitude of the electric field. Equation (2.14) with all its components (2.15)-(2.20) is now combined with the equations for the gradient and scattering force (Eq (2.12) and (2.13)). After some algebra and a coordinate change, one reaches the following equations, which describe r and z components of each of the two optical forces [56].

$$F^r_\mathrm{grad}(r,z) = -\frac{2\varepsilon_0\varepsilon_\mathrm{m}}{\pi}\mathrm{Re}\{\alpha\}\,|\mathbf{E}_0|^2\,\frac{w_0^2}{w^4}\exp\left[-\frac{2r^2}{w^2}\right] r, \tag{2.21}$$

$$F^z_\mathrm{grad}(r,z) = -\frac{\varepsilon_0\varepsilon_\mathrm{m}}{\pi}\mathrm{Re}\{\alpha\}\,|\mathbf{E}_0|^2\,\frac{w_0^4}{z_0^2}\left(\frac{1}{w^4} - \frac{2r^2}{w^6}\right)\exp\left[-\frac{2r^2}{w^2}\right] z, \tag{2.22}$$

$$F^r_\mathrm{scat}(r,z) = \frac{\varepsilon_0\varepsilon_\mathrm{m}}{\pi}\mathrm{Im}\{\alpha\}\,|\mathbf{E}_0|^2\,\frac{w_0^2}{w^2}\frac{k}{R}\exp\left[-\frac{2r^2}{w^2}\right] r, \tag{2.23}$$

$$F^z_\mathrm{scat}(r,z) = \frac{2\varepsilon_0\varepsilon_\mathrm{m}}{\pi}\mathrm{Im}\{\alpha\}\,|\mathbf{E}_0|^2\,\frac{w_0^2}{w^2}\left[k\left(1 - \frac{r^2(z^2 - z_0^2)}{w(z^2+z_0^2)^2}\right) - \frac{w_0^2}{z_0 w^2}\right]\exp\left[-\frac{2r^2}{w^2}\right]. \tag{2.24}$$

As an illustrative example we analyze the optical forces in a cross section along the xz-direction on a gold nanorod with length 80 nm and width 40 nm illuminated by a Gaussian beam focused through an objective with NA = 1.4. Two different laser wavelengths; namely 660 nm and 1064 nm, are analyzed to illustrate the difference between trapping with on- and off-resonance laser light.

For isotropic gold nanospheres the trapping forces will be independent of the orientation of the particle. For nanorods, this will not be the case. Depending on the direction of the nanorod the light will couple differently to the two separate polarizabilities of the rod. In the calculations presented below the nanorod is assumed to be oriented with the long axis in the plane perpendicular to the optical axis. This will result in the fact that in the z-direction light will couple to the transverse polarizability (α_{T}) of the nanorod. Furthermore, it is assumed that the particle is driven to rotate around one of its short axis by circular polarization of the laser light, with a frequency much smaller than the frequency of the light (i.e. the angular frequency of the circular polarization). Hence, in the r-direction (Eq (2.21) and (2.23)) the incoming light will excite both the two directions equally, if the laser light is perfectly circularly polarized ($I_{\mathrm{x}} = I_{\mathrm{y}}$).

In fact, the orientation when the nanorod is instead standing up was also analyzed. However, this produced a trapping potential that for the particular nanorod type is more shallow, and hence the upright direction will not be the preferred trapping direction.

In Figure 2.5 the 1064 nm laser case is displayed. By comparison the scattering force, as seen in the left panel, is weaker than the gradient force (displayed in the middle panel). This results in a three dimensional trap when the two forces are combined into the total optical force, as seen in the rightmost panel. The potential well is displaced by about 100 nm from the focus of the objective because of the scattering force.

It is at this point interesting to define what is meant by stable trapping. Stable trapping occurs when the potential well created by the focused laser beam ($U(\mathbf{r})$) is much larger than the kinetic energy of the particle due to Brownian motion. Therefore, the stability criterion for optical tweezers is defined as when the Boltzmann factor is much smaller than 1; i.e. $\exp\left[-\frac{U(\mathbf{r})}{k_{\mathrm{B}}T}\right] \ll 1$, where k_{B} is the Boltzmann constant. An

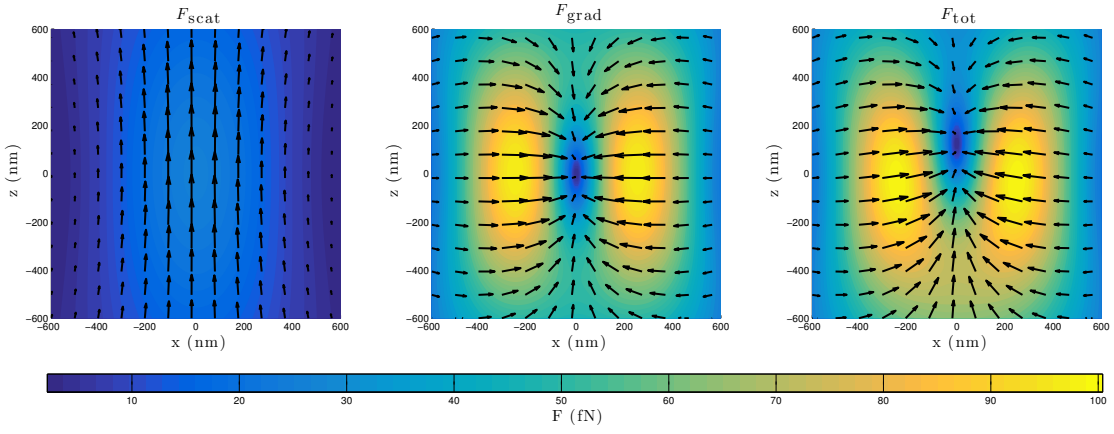

Figure 2.5: Calculated spatial distribution of trapping forces in a laser beam with a paraxial Gaussian distribution affecting a gold nanorod of dimensions 80/40 nm. Here, the laser light has a power of 8 mW and a wavelength of 1064 nm and is focused by an objective with NA = 1.4. The scattering (F_{scat}) and gradient forces (F_{grad}) are presented separately in the left and middle graph. The figure to the right represents the total optical force. For this particular parameter set a stable 3D trap is generated.

estimate to when this criterion is fulfilled can be said to be when $\frac{U(\mathbf{r})}{k_\mathrm{B}T} \geq 10$. In fact, the kinetic energy of a colloidal particle induced by Brownian motion is known to reach peaks around $10k_\mathrm{B}T$, and hence this is a reasonable value to compare with [14]. The trapping potential can be obtained from the gradient force under the assumption that it is conservative. The depth of the potential in the center of the trap (U_0) is then simply obtained by calculating the work needed to bring the trapped particle from the origin to infinity (a distance far enough so the work integral converges). For this parameter configuration and particle the trapping potential is found to be $12.3k_\mathrm{B}T$ in the xy-direction if the temperature is assumed to be $T = 300\,\mathrm{K}$, and stable trapping is thus possible.

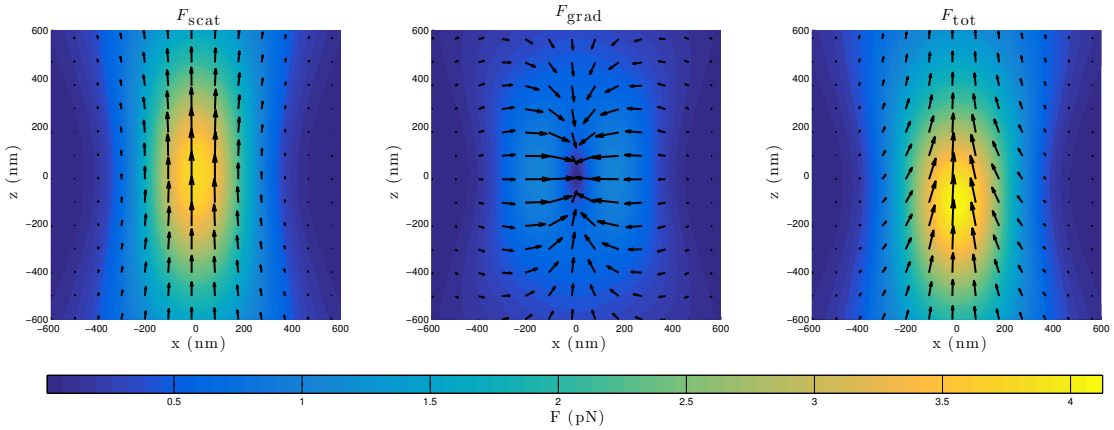

Figure 2.6: Calculated spatial distribution of trapping forces in a laser beam with a paraxial Gaussian distribution affecting a gold nanorod of dimensions 80/40 nm. Here, the laser light has a power of 8 mW and a wavelength of 660 nm and is focused by an objective with NA = 1.4. The scattering (F_{scat}) and gradient forces (F_{grad}) are presented separately in the left and middle graph. The figure to the right represents the total optical force. For this particular parameter set no stable 3D trap can be generated resulting from too high scattering at this wavelength.

In Figure 2.6 the 660 nm laser light case is presented. Contrary to the prior case, here the scattering force is considerably enhanced and indeed larger than the gradient force. This results in a total force where no three dimensional confinement is possible and the particle is instead constantly pushed away from the focus. Nevertheless, if we perform the same work integral in this case we reach a potential well from the gradient force that is $66.1k_\mathrm{B}T$ deep. Therefore, if the particle movement in the z-direction is restricted, for example by a glass surface, the particle will be stably trapped in the xy or radial plane. Since the scattering of a particle scales with its size, any gold particles larger than the one analyzed here will also not be trapped in 3D at this laser wavelength.

It should be mentioned that the validity of the model used in these calculations is decreasing as the angle of incoming radiation is increasing. Hence, for high NA objectives the estimated forces will differ from the their true values [57]. Nevertheless, since the purpose of the calculations performed above is mostly to illustrate the qualitative properties of the Gaussian optical trap the weakness of this model is overlooked.

2.2.2 Trapping stiffness

For small deviations from the trapping center, the force acting on the trapped particle is approximately that of a linear spring. The strength of the restoring force acting on the rod can therefore be described as a Hookean spring with trapping stiffness k. The trapping stiffness is an established method for calibrating and quality testing the optical tweezers setup [58].

Brownian motion of the particle inside the trap will give rise to positional oscillations and these can be described by a stochastic differential equation (the Langevin equation) in the so-called Einstein-Ornstein-Uhlenbeck theory [59]. Within this framework, the Fourier transform of the stochastic oscillatory position of the trapped particle is shown to generate a Lorentzian frequency dependent power spectrum. This power spectrum is one-sided, centered around zero frequency and is given by

$$|\tilde{x}(f)| = \frac{k_{\mathrm{B}}T}{\pi^2\beta\,[f_{\mathrm{c}}^2 + f^2]}. \tag{2.25}$$

Here, β is the hydrodynamic drag coefficient of the particle in the surrounding liquid, $f_{\mathrm{c}} = \left(\frac{k}{2\pi\beta}\right)$ is the corner frequency containing k that is the trapping stiffness of the optical tweezers. Therefore, we can obtain an expression for the trapping stiffness as

$$k = 2\pi\beta f_{\mathrm{c}}. \tag{2.26}$$

The hydrodynamic drag coefficient in a bulk medium of incompressible fluid is given by $\beta = 6\pi\eta r$, where r is the effective radius of the particle and

$$\eta(T) = \eta_0 \cdot \exp\left(\frac{E_{\mathrm{a}}}{N_{\mathrm{a}}k_{\mathrm{B}}[T - T^\star]}\right) \tag{2.27}$$

is the viscosity of the surrounding media, which is approximated through the Arrhenius-type equation [60]. Here, $\eta_0 = 24.2\ \mu$Pa·s, $E_{\mathrm{a}} = 4.74\,$kJ/mol is an activation energy, N_{A} is Avogadro's number, $T^\star = 140$ K is the temperature offset for this particular E_{a} and T is the particle/water interface temperature.

As a particle approaches a surface the hydrodynamic drag is altered and increased because of interface effects between water and glass. In this case, the hydrodynamic drag coefficient can be corrected through the following expression [58]

$$\beta_{\mathrm{surf}} = \frac{6\pi\eta r}{1 - \frac{9}{16}\left(\frac{r}{h}\right) + \frac{1}{8}\left(\frac{r}{h}\right)^3 - \frac{45}{256}\left(\frac{r}{h}\right)^4 - \frac{1}{16}\left(\frac{r}{h}\right)^5}. \tag{2.28}$$

The corner frequency can be determined by fitting the experimentally obtained power spectrum, and the hydrodynamic drag coefficient is estimated as in (2.28). Thereafter, all the quantities in Equation (2.26) are known and the trapping stiffness can thus be determined.

2.3 Optical rotation

In general, angular momentum from light can transfer via absorption and scattering events to a nanoscopic particle in an optical trap. In the dipole limit within the quasi-static approximation, we can understand this as a torque that arises as a way to align the direction of the dipole with the polarization of the electric field. For a circularly polarized electric field no stationary direction of polarization exists and the particle will instead of aligning with a certain polarization direction be driven to rotate along with the polarized wavefront. For rotation around a single axis, we can set up an equation of motion as

$$J\left(\frac{\mathrm{d}\omega}{\mathrm{d}t}\right) = M_{\mathrm{opt}} + M_{\mathrm{f}} + M_{\mathrm{s}}, \tag{2.29}$$

where J is the moment of inertia for the particle, ω is the angular velocity, M_{opt} is the total driving optical torque, M_{f} the breaking friction torque from the surrounding liquid and M_{s} a stochastic torque due to rotational Brownian motion.

The frictional torque from the surrounding liquid is counteracting the driving optical torque. For small particles, the flow of liquid around the object is laminar due to the low Reynolds number of microscopic objects in liquid medium. Consequently, the friction torque can be expressed as $M_{\mathrm{f}} = -\pi\eta(T)L^3\omega\gamma$, where L is the length of the particle and $\eta(T)$ is the viscosity of the surrounding water, calculated as above in Equation (2.27) [36]. γ is a shape correction for a spheroidal case from the spherical case as derived in [61] and expressed in terms of the reciprocal eccentricity of a spheroid with semi-major and -minor axis a and b; $\xi_0 = \dfrac{1}{e} = \dfrac{1}{\sqrt{1-\left(\frac{b}{a}\right)^2}}$ and $\hat{\xi_0} = \ln\left(\dfrac{\xi_0+1}{\xi_0+1}\right)$ as

$$\gamma = \frac{-e^3}{-2\xi_0 + (\xi_0^2+1)\hat{\xi_0}} \cdot \left[2\xi_0(\xi_0^2-1)\tanh^{-1}\left(\frac{1}{\xi_0}\right) + \frac{-4+8\xi_0^2-3\xi_0(\xi_0^2-1)\hat{\xi_0}}{3}\right]. \tag{2.30}$$

In the model used throughout this thesis we neglect the frictional interaction between the particle and the interface against which it is trapped.

Assuming the particle is rotating in a steady state where the optical torque is exactly counteracted by the friction torque, we can derive an expression for the rotation frequency of the nanoparticles. For spherical particles it can be done as in reference [35], and in the anisotropic spheroidal case we get an expression as in [36]

$$f_{\mathrm{avg}} = \frac{M_{\mathrm{opt}}}{2\pi^2\eta(T)\gamma L^3}. \tag{2.31}$$

A general expression for the total optical torque is not attainable analytically for more complex particles than spheres and spheroids or those larger than to fit within the quasi-static regime. M_{opt} for these cases should instead be obtained using Maxwell Stress Tensor (MST) method through numerical simulations [34]. However, the time-averaged optical torque perpendicular to the direction of propagation of the laser light

and within the dipolar regime can be expressed as

$$M_{\text{opt}} = \langle \mathbf{p} \times \mathbf{E}_{\text{tot}} \rangle = \frac{1}{2}\text{Re}\left[\mathbf{p}^* \times \mathbf{E}_{\text{tot}}\right], \tag{2.32}$$

where the second equality is reached by performing the time-averaging. In this description $\mathbf{E}$ is the total electric field around the particle. As established in Section 2.1.1.3 the particle will in turn affect the field around itself due to its physical size. Within this framework we know that $\mathbf{p} = \varepsilon_0\varepsilon_{\text{m}}\boldsymbol{\alpha}_{\text{MLWA}} \cdot \mathbf{E}_{\text{inc}} = \varepsilon_0\varepsilon_{\text{m}}\boldsymbol{\alpha}_0 \cdot \mathbf{E}_{\text{tot}}$, where $\boldsymbol{\alpha}_{\text{MLWA}}$ is the MLWA-corrected polarizability and $\boldsymbol{\alpha}_0$ is the uncorrected one. $\mathbf{E}_{\text{inc}}$ is the incident electric field and $\mathbf{E}_{\text{tot}}$ is the total electric field, including radiation from the particle itself. From this equality, we can find an expression for the unknown total field by expressing it in terms of the known incident field and the corrected and uncorrected polarizabilities. From this, we can express Equation (2.32) as

$$M_{\text{opt}} = \frac{1}{2}\text{Re}\left[(\varepsilon_0\varepsilon_{\text{m}}\boldsymbol{\alpha}_{\text{MLWA}} \cdot \mathbf{E}_{\text{inc}})^* \times \boldsymbol{\alpha}_0^{-1} \cdot (\boldsymbol{\alpha}_{\text{MLWA}} \cdot \mathbf{E}_{\text{inc}})\right]. \tag{2.33}$$

The total optical torque will be composed of an absorption component (M_{abs}) and a scattering component (M_{scat}) according to $M_{\text{opt}} = M_{\text{abs}} + M_{\text{scat}}$. The absorption torque can be obtained as $M_{\text{abs}} = \frac{\sigma_{\text{abs}} I_{\text{inc}}}{\omega_0}$ where $I_{\text{inc}} = \frac{\varepsilon_0 c}{2}\left|\mathbf{E}_0\right|^2$ is the intensity of the trapping laser beam at the focus and ω_0 is the angular frequency of the trapping laser. From knowing the total and absorption component of the torque, the scattering component can be arrived at from $M_{\text{scat}} = M_{\text{opt}} - M_{\text{abs}}$.

2.3.1 Torque calculations

Unlike the optical force calculations, which required an electric field with Gaussian distribution, here a plane wave is sufficient to generate valid results. Hence, the incident electric field used for the torque calculations is expressed as $\mathbf{E}_{\text{inc}} = \frac{E_0}{\sqrt{2}}(\hat{x} + i\hat{y})$. For ease of calculation, it is now assumed that the particle is oriented with its long axis along the x-direction and one of its short axis along the y-direction. This makes the polarizability tensor diagonal. In order to illustrate the optical torque on a nanorod in a circularly polarized optical trap this expression for the incident electric field is inserted in Equation (2.33). By using Equation (2.31), the average rotation frequency can be estimated from knowing the optical torque. In Figure 2.7 the calculated torques (2.7a) and estimated average rotation frequency (2.7b) are presented for a nanorod with dimensions 80/40 nm driven at a laser power of 8 mW through a 1.4 NA objective at a range of laser wavelengths. At this particular nanorod size we see that the absorption and scattering torques are approximately equal. This is not generally the case, but rather an eventuality for this particle size. For small particles the absorption torque is strongly dominating over scattering, but for large particles the scattering is dominating [36]. It seems the dimension 80/40 nm is essentially the size when the two regimes meet. The rotation frequency is for the optimal driving wavelength on the order of tenth of kHz as seen in previous experiments.

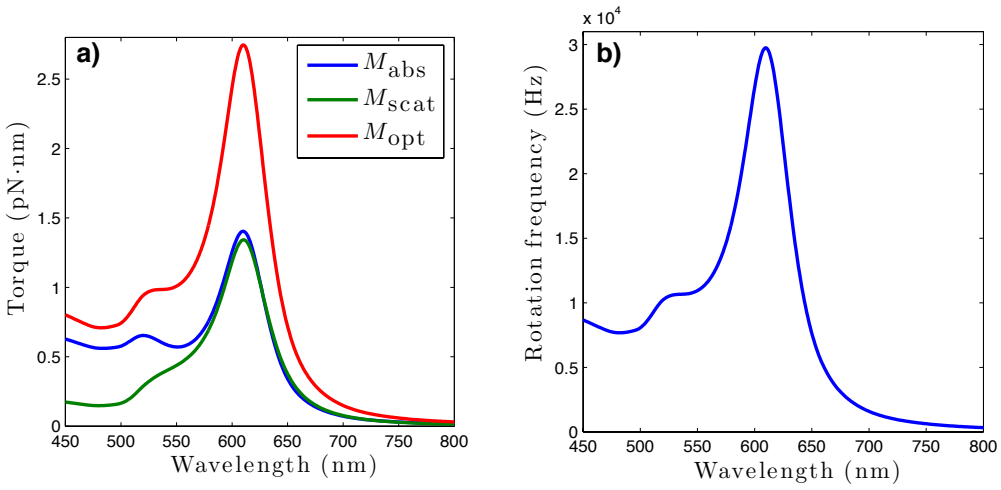

Figure 2.7: Calculated optical torques (a) as well as rotation frequency (b) for a nanorod with dimensions 80/40 nm within the quasi-static regime. For this particular nanorod the optical torques from absorption and scattering are almost equal.

2.3.2 Rotational dynamics through autocorrelation

Generally autocorrelation is the process of cross-correlating a signal with itself after certain lag times. This process can provide information about a periodic signal, which has been concealed by noise, by essentially revealing the tendency of a system to maintain a certain property over time. Autocorrelation has been widely used to detect patterns in signals for example in fluorescence spectroscopy [62].

In the experimental setup described below in Section 3.1.1 some laser light hitting the trapped and rotating particle will be back-scattered, and some light from the white light illumination will be forwardly scattered into the objective again. Since all particles (even spheres) have some irregularities, the scattering will be dependent on the orientation of the particle. If we take the illustrative example of a gold nanorod we understand from the discussion above in Section 2.1 the rod will be scattering light most effectively polarized in the direction of its long axis. By passing the scattered light through a polarizer, if the particle is rotating, it is understood that there will be a fluctuation in the collected scattered light with a maximum corresponding to when the long axis of the particle is aligned with the direction of the polarizer. Since the nanorod has a twofold rotational symmetry (the long axis of the particle will align two times with the direction of the polarizer during one revolution) the intensity fluctuations will be twice as frequent as the rotation frequency of the trapped rotating rod. With the same deduction it is realized that for a cube with fourfold rotational symmetry, the polarized scattered light will oscillate four times faster than one revolution of the cube is performed, supposing that the cube is rotating around one of its faces.

Information about the rotational dynamics of the trapped particle is contained in the fluctuations in the linearly polarized scattered intensity in itself. However, this signal might yield rather noisy and ambiguous information. Hence, it is preferable to

perform autocorrelation on the intensity collected to obtain a correlogram. The intensity correlated signal yields information about an oscillatory behaviour of the data that is not always accessible from the polarized scattering signal.

For a single-frequency sinusoidal signal (no matter if obscured by noise or not) the autocorrelation signal should be oscillatory without any decay. However, if the signal that is autocorrelated is modulated with other frequency signals, that is to say the oscillatory frequency is not constant, then the correlation will decrease as lag time increases. The amplitude decay of the autocorreleation signal can be described with an exponential term, which provides information about the time scale of the frequency change. In the case of a rotating particle in an optical trap rotational Brownian motion will create a stochastic torque on the particle generating a fluctuation in the rotation frequency, which in turn will lead to a decay in the autocorrelation signal.

We assume rotation in only one plane and that the scattering intensity varies as $I(\tau) = I_0 + I_1 \cos N\psi$, where ψ is the rotation angle and N is the degree of detectable rotational symmetry (that for a rod is $N = 2$). By solving the equation of motion expressed in (2.29) under certain assumption, as done in reference [35], one obtains an expression for the autocorrelation signal of a rotating nanoparticle as

$$C(\tau) = I_0^2 + \frac{I_1^2}{2} \exp\left[-\frac{\tau}{\tau_0}\right] \cos(2N\pi f_{\text{avg}}\tau), \tag{2.34}$$

where τ is the lag time and f_{avg} is the average rotation frequency. The term

$$\tau_0 = \frac{8\pi\eta(T)\gamma a^3}{N^2 k_{\text{B}} T} \tag{2.35}$$

describes the autocorrelation decay time, providing information of the rotational Brownian motion. Here, a is the semi-major axis of the spheroid, T is the particle surface temperature, J is the moment of inertia and γ is as above in Equation (2.30) the shape correction for a spheroidal case from the spherical case.

From fitting Equation (2.34) to the measured autocorrelation data, values for average rotation frequency f_{avg} and τ_0 can be extracted.

2.3.2.1 Temperature estimation

When examining Equation (2.35) for the autocorrelation decay time associated with the rotational Brownian motion, it is noticed that when τ_0 is obtained from the fitting of the correlogram, an equation is obtained with temperature as the only unknown. Therefore, the measurement of τ_0 gives us a way to estimate the temperature of the immediate water environment around the particle after solving equation (2.35) with (2.27) describing $\eta(T)$.

This method for estimating temperature of the particle environment is the one used in the results below when referring to; “extract temperature form the autocorrelation decay time”, or simply, “estimate temperature”.

3

Experimental methods

In the chapters above the stage has been set for the project performed in this thesis, by a thorough introduction to previous seminal studies in the field as well as the theoretical framework necessary to understand and extract results. These components are essential to draw conclusions that will continue to push the forefront of scientific understanding. However, there is another fundamental step from the background and theory to reach the results. This is the collection of the data necessary to validate or falsify any hypothesis that the study sets out from. These data can be generated in a wide range of ways from computational work to experiments performed in a laboratory.

The research performed in this thesis is based on the latter of these two; namely, experimental work. Laboratory studies as the ones conducted here set out to gather data on a specific system, with a proposed experimental setup. During the realization of this setup, it is far from unusual that initial ideas are revised. Experimental studies are unpredictable, and detours are often taken along the way in order to reach an effective and working setup. The following chapter aims to summarize the setup created, and the undertakings performed in the lab, necessary to obtain the results of this study.

3.1 Construction of Optical tweezers

Construction of the optical tweezers system is made around a Nikon Eclipse Ti inverted microscope, with white-light dark-field illumination for dark-field imaging and detection of nanoparticles. The setup does to a high degree resemble the one presented in references [35, 36]. Inspiration to the tweezers system has also been taken from [54, 63]. A generic setup of optical tweezers can be seen in Figure 3.1. A laser beam is first expanded to the appropriate beam diameter, and then introduced into a microscope objective with a dichroic mirror or beamsplitter. Both the laser light and the illumination light are scattered by the trapped object and collected by the objective; whereafter the light can be analyzed to interrogate the trapped object. One common system employed in many setups is some sort of position detection such as a fast camera or a so-called quadrant photodiode.

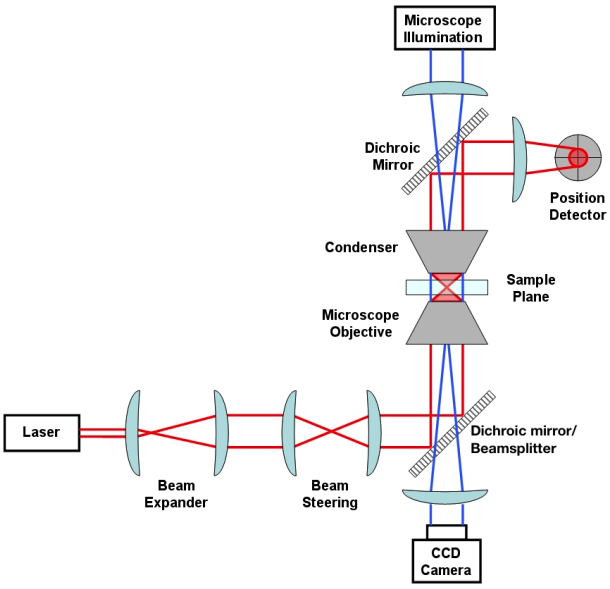

Figure 3.1: A generic optical tweezers setup. A laser is through the use of a lens pair expanded to an appropriate size and collimated (to parallel rays). Thereafter, another lens pair denoted as beam steering will enable movement of the optical tweezers with respect to the sample. Hereafter, the beam is introduced into the optical path of the microscope by a dichroic mirror or a beamsplitter. After the microscope objective and trap, the light from the laser will be collected into a position detection system. Since dichroic mirrors are used, the microscope can be used for imaging in parallel with the trap.

3.1.1 Trapping system

The trapping laser used in this setup is a Cobolt Flamenco 05-01 Series with a variable power output between 35 and 500 mW of 660 nm monochromatic light. This light should be vertically linearly polarized (100:1 polarization ratio) so no additional linear polarizer is introduced to the optical path.

Similarly to in Figure 3.1 the laser in this setup will be passed through a dual lens system in a Keplerian telescope configuration as displayed in more detail in Figure 3.2, which will expand and collimate the beam. The degree of expansion is calculated from Ray optics and becomes the simple expression

$$M = \frac{h_2}{h_1} = \frac{f_2}{f_1}, \tag{3.1}$$

where f_1 and f_2 are focal lengths of the two lenses, h_1 and h_2 are the size of the beam before and after the lens system, and M is the magnification factor. The beam diameter should be slightly larger than the microscope objective entrance for maximum trapping stability since this enables use of the entire NA of the objective and will produce a tightly focused diffraction limited focus of the trap [63, 64]. To correctly overfill the back aperture of the objective we calculate the size of the back focal plane of the objective (d). This can be derived from Ray optics where the microscope is a two lens system with

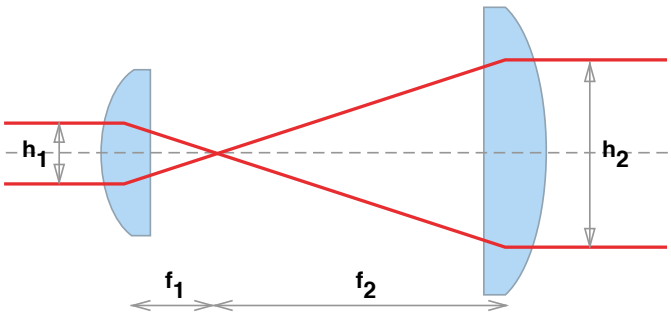

Figure 3.2: A Keplerian telescope where two lenses are separated by their focal lengths. The telescope is expanding the width of the laser beam by a magnification factor of M from h_1 to h_2 through the relation $M = \frac{h_2}{h_1} = \frac{f_2}{f_1}$.

the objective as a single lens (focal length f_o) and a tube lens (focal length f_t, which for Nikon objectives is $f_\mathrm{t} = 200\,\mathrm{mm}$) as in [65].

$$\begin{cases} M = \frac{f_\mathrm{t}}{f_\mathrm{o}} \\ d = 2 f_\mathrm{o} \sin\theta \end{cases} \Rightarrow d = 2\mathrm{NA}\frac{f_\mathrm{t}}{M}, \tag{3.2}$$

where $NA = n \sin\theta$ is the numerical aperture, θ is the largest angle that the objective can collect light from and M is the magnification of the objective. The objective that is used to create our trap is a 40x/0.95NA objective (Nikon CFI Plan Apo Lambda 40X) with a working distance of $0.25 - 0.16\,\mathrm{mm}$. Hence, for this objective the back aperture is calculated to be $d_{40\mathrm{x}/0.95\mathrm{NA}} = 2 \cdot 0.95 \cdot \frac{200\,\mathrm{mm}}{60} = 9.5\,\mathrm{mm}$. Knowing the size of the back aperture of the objective, two lenses with focal lengths of $f_1 = 30\,\mathrm{mm}$ and $f_2 = 400\,\mathrm{mm}$ are chosen. With these, the beam diameter is expanded from its initial diameter of $750\,\mu\mathrm{m}$ to $d_\mathrm{beam} = 750\,\mu\mathrm{m} \cdot \frac{400}{30} \approx 10\,\mathrm{mm}$. In this configuration, the full NA of the objective is utilized to obtain a diffraction limited focal spot. The size of this spot can be estimated from Abbes criteria to be $d_\mathrm{min} = \frac{\lambda}{2\mathrm{NA}} = \frac{660\,\mathrm{nm}}{2 \cdot 0.95} \approx 350\,\mathrm{nm}$.

Since this project lacks the need for beam steering, and rather relies on the translational movement of the sample stage, the subsequent lens pair in Figure 3.1 is omitted. Now through the use of mirrors the beam is made to enter the microscope so that it is aligned with the Cartesian axes of the microscope. On the way into the microscope, the light will be passed through a quarter-wave plate (QWP) and a half-wave plate (HWP) that will convert the linearly polarized light into circularly polarized light at the sample plane (these waveplate can easily be removed to retain the linear polarization if needed). Laser light is now reflected by a 50T/50R (50% transmission and 50% reflection) beamsplitter and enters the objective.

During trapping and rotation, laser light as well as white illumination light will be scattered into the objective. This light will be passed down the optical path of the microscope. A part of the light will be reflected by a beamsplitter (70T/30R) through a linear polarizer and a band pass filter (filtering out the white light) and collected via a fiber. The fiber will couple the light to an Avalanche Photo Diode (APD) and the

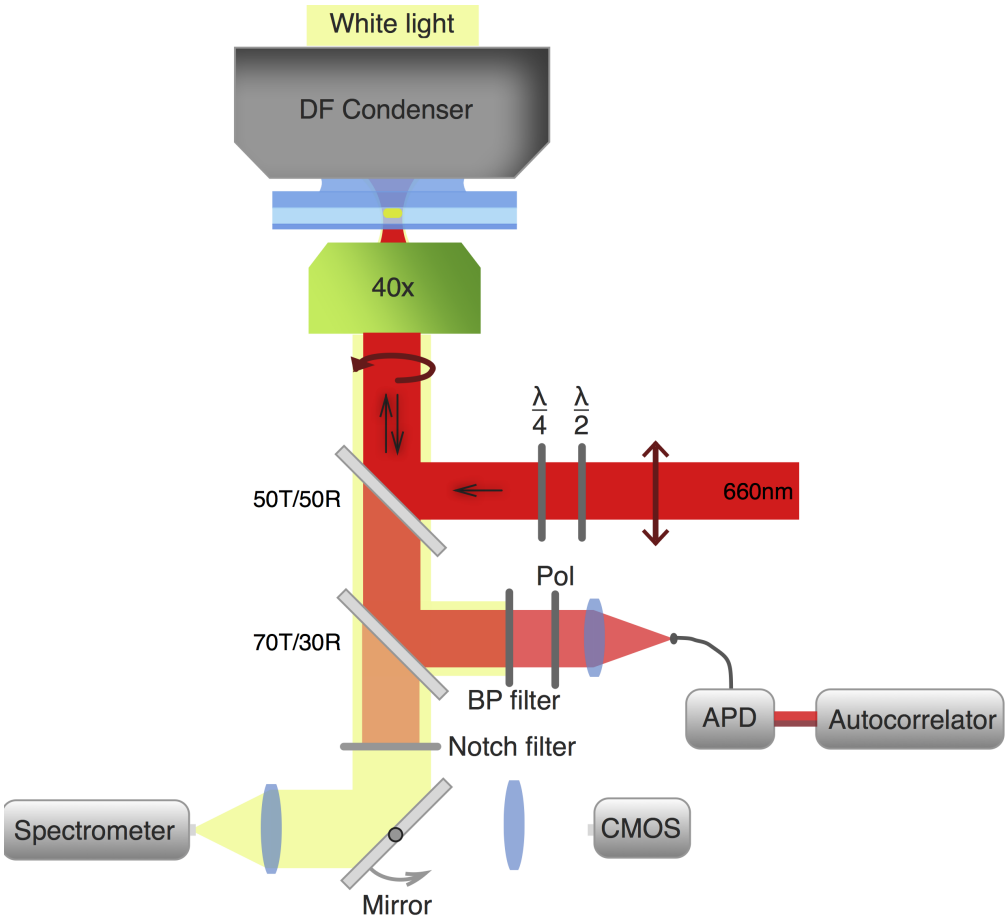

Figure 3.3: An illustration of the setup realized in this project combining an optical trap with instrumentation for spectroscopic measurements as well as autocorrelation analysis. Collimated laser light is circularly polarized using a sequence of two waveplates and then guided to the objective with a beamsplitter. Dark-field illuminated white light and laser light is scattered by the trapped nanoparticle and collected by the objective. The scattered laser light will be guided by a beamsplitter (70T/30R) to an APD, which creates a signal that is analyzed in an autocorrelator. The scattered white light is passed to a spectrometer after the laser light has been filtered away.

signal will thereafter be analyzed with an autocorrelator (ALV-5000) system to deduce the rotational dynamics of the nanoparticle, as described in Section 2.3.2. This method of detection is sometimes referred to as correlation spectroscopy. If the rotation of the particle is sufficiently slow, the rotation can be monitored using a high-speed CMOS camera (Andor Neo 5.5 sCMOS) with a sampling rate of 4.76 kHz. If the rotation is faster than this, other methods need to be utilized, for example an APD coupled to an autocorrelator as in this work.

The remaining light after the beamsplitter to the APD will be passed through laser line filters (Semrock 658 nm Stopline and Thorlabs 658 nm Notch filter) to filter away the laser light from the white light scattered from the particle. At the base of the

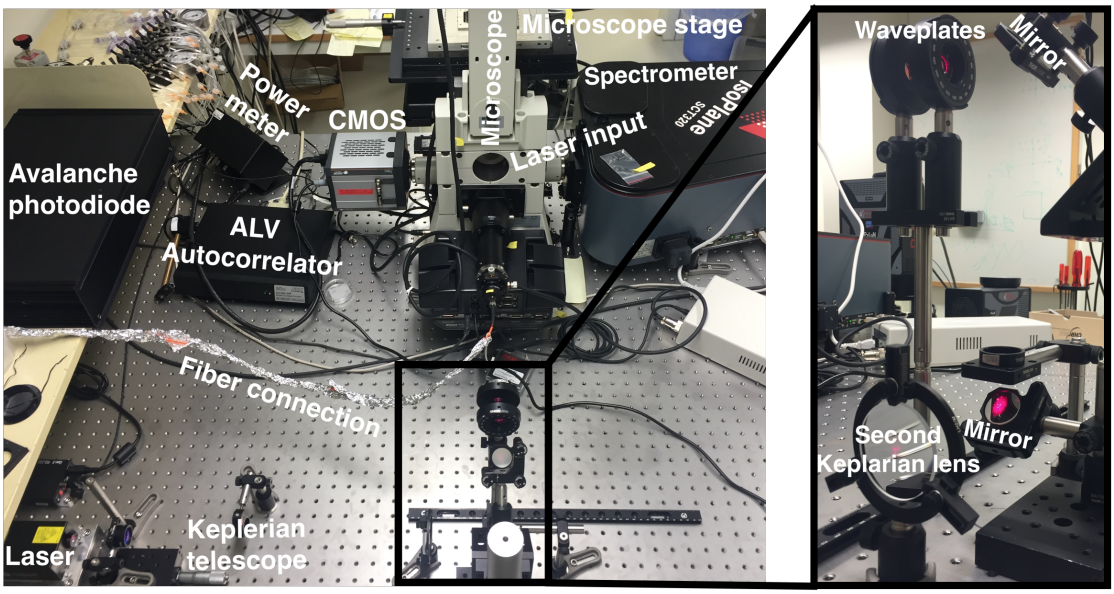

Figure 3.4: Photographs of the setup described in the text. The left picture shows the setup of the entire system from behind the microscope, and the most important parts of the setup have been marked for clarity. The inset image displays the mirror-waveplate configuration that directs and polarizes the light.

microscope, a mirror can direct light to two different exit ports (right or left). In one of these exit ports of the microscope, a free space coupled grating based spectrometer (Princeton Instruments IsoPlane SCT320) with a liquid nitrogen cooled CCD camera (Princeton Instruments PyLoN) is connected in which DF scattering spectra can be recorded. In the other exit port, the fast CMOS camera is connected and can image and record the of particle position. An overall schematic setup of the optical tweezers system with its surrounding measurement instrumentation can be seen in Figure 3.3. In Figure 3.4 two photographs of the setup are presented, where the large one shows an overall image of the entire setup from behind whereas the inset shows a close-up image of the mirror-waveplate system.

The Cobolt laser as well as the PI spectrometer has the possibility to communicate with a computer via LabVIEW. Dr. Srdjan Acimovic has constructed a working VI for the spectrometer, and hence a subprogram is constructed and included in preexisting code, which allows control over the laser simultaneously as the spectrometer. The autocorrelator requires a 32-bit computer (the computer controlling the spectrometer and laser is a 64-bit one) and is thus not possible to control from the same computer as the two other instruments. The two continuous measurements, spectral (and laser) as well as autocorrelation, are instead linked by two parallel time measurements during data processing. This results in a setup that can continuously and parallelly measure DF scattering spectra and autocorrelation signals at a well-controlled range of different laser powers for trapped and rotating particles.

3.1.2 Laser intensity

The output power of the laser can be tuned between 35 and 500 mW. However, all the optical components in the beam path from output to the sample plane will attenuate the intensity of the laser power. To obtain the laser power that is applied to the sample after the objective, the power is measured with a power meter. The power at the sample plane is linearly dependent on the laser output power, and a linear model is fitted to the data that yields a dependence according to $y = 0.019824x + 0.087373$. The data and fit can be seen in Figure 3.5 and this linear dependence is used to calculate applied power to the particle in future measurements.

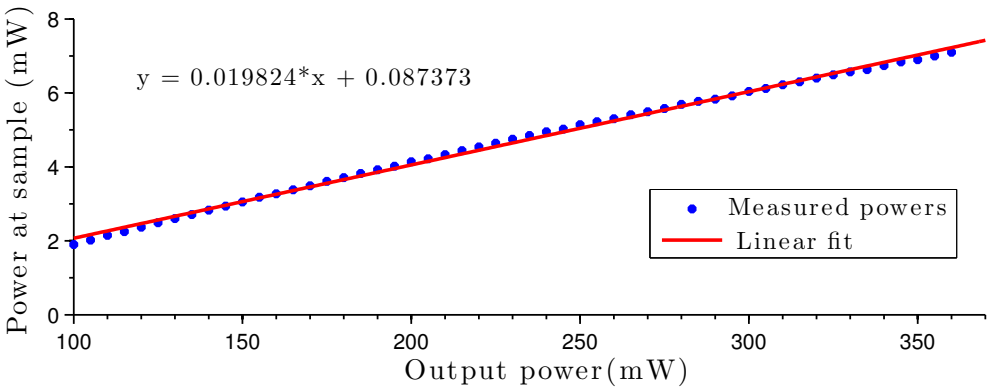

Figure 3.5: Measured laser power at the sample plane after the objective, depending on output laser power. A linear model is fitted to the data and yields a dependence according to $y = 0.019824x + 0.087373$.

3.2 Circular polarization of laser

To obtain the optimal single beam optical trapping system for spinning gold nanoparticles the laser light reaching the specimen plane should be perfectly circularly polarized. The first approach to this is known from basic optics, and it involves using a QWP with its fast axis in a 45 degree angle from the linear polarization direction of incoming light. This should in theory introduce a phase shift of 90 degrees between two orthogonal polarization components of the linear polarizations resulting in circular polarization.

3.2.1 Measurement of polarization phase

Using a polarizer and a power meter in sequence after the objective the ellipticity of the light transmitted can be measured. By rotating the polarizer and noting the maximum and minimum powers transmitted one can obtain the ratio between the lengths of the semi-major and semi-minor axis of the polarization ellipse ($\frac{a}{b}$). In the Jones vector

formalism where the two polarization directions are described as

$$\begin{cases} E_x = E_{0x}e^{i(kz-\omega t+\varphi_x)} \\ E_y = E_{0y}e^{i(kz-\omega t+\varphi_y)} \end{cases} \Rightarrow \tilde{\mathbf{E}}_0 = \begin{bmatrix} E_{0x}e^{i\varphi_x} \\ E_{0y}e^{i\varphi_y} \end{bmatrix}, \tag{3.3}$$

where z is the propagation direction, ω is the angular frequency, E_{0x} and E_{0y} are amplitudes and φ_x and φ_y are phases of the two components. We assume that the two decomposed polarization directions are of equal magnitude ($E_{0x}^2 = E_{0y}^2 = 1$) and will thus get a polarization ellipse oriented at 45 degrees from the Cartesian coordinate axes[1], as in Figure 3.6. Here, the angle ψ defines the angle between the x-axis and the major axis of the ellipse (A) and through a geometrical consideration also between the y-axis and the minor axis (B). This ellipse will vary with respect to the phase difference δ and can be described with the equation

$$\begin{aligned} \frac{E_x(t)^2}{E_{0x}^2} + \frac{E_y(t)^2}{E_{0y}^2} - \frac{2E_x(t)E_y(t)}{E_{0x}E_{0y}} \cos\delta &= \sin^2\delta \\ \Rightarrow x^2 + y^2 - 2xy\cos\delta &= \sin^2\delta. \end{aligned} \tag{3.4}$$

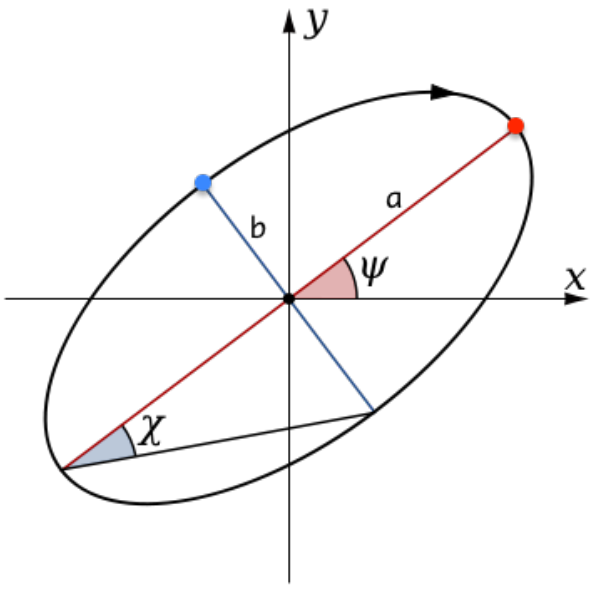

Figure 3.6: A polarization ellipse where the amplitude of the two polarization directions are assumed to be equal ($E_{0x}^2 = E_{0y}^2 = 1$). The angle ψ defines the angle between the major axis of the ellipse and the x-axis and also between the minor axis and the y-axis, and a and b are the lengths semi-major and semi-minor axis.

[1] If this assumption is not made, the polarization ellipse can have an arbitrary angle with respect to its coordinate axis. This case is not discussed further here, but rigorously in [66].

Equation (3.4) is reached from the Jones vector with some algebraic steps presented in [66]. The implication in (3.4) is reached by changing variables to the coordinate system of Figure 3.6 as $x = \frac{E_x(t)}{E_{0x}}$ and $y = \frac{E_y(t)}{E_{0y}}$. If we in (3.4) input the coordinate for points on the ellipse in the ψ direction from the x- and y-axis, i.e. the red and blue points, we get

$$\left.\begin{aligned}(a\cos\psi, a\sin\psi) \Rightarrow a^2 - 2a^2\cos\psi\sin\psi\cos\delta = \sin^2\psi \\ (-b\sin\psi, b\cos\psi) \Rightarrow b^2 + 2b^2\cos\psi\sin\psi\cos\delta = \sin^2\psi\end{aligned}\right\}$$
$$\Rightarrow \sin^2\delta = \frac{2a^2b^2}{a^2+b^2}. \tag{3.5}$$

The last equation is reached from eliminating $\cos\psi\sin\psi$, which is a similar term in both equations above. From definition, we know that the squared sum of the semi-major and semi-minor axis is a constant ($a^2 + b^2 = C$) and since circular polarization is a special case of elliptical polarization we get that $E_{0x}^2 + E_{0y}^2 = 2 \Rightarrow C = 2$. As this goes into Equation (3.5) we get

$$\sin\delta = ab. \tag{3.6}$$

The ratio $\frac{a}{b} = \frac{A}{B}$ together with $a^2 + b^2 = C$ gives us two equations that can be used to expand (3.6) to

$$\sin\delta = 2\frac{B}{A}\frac{1}{1+\left(\frac{B}{A}\right)^2} = \frac{2}{\frac{A}{B}+\frac{B}{A}} \Rightarrow \delta = \arcsin\frac{2}{\frac{A}{B}+\frac{B}{A}}. \tag{3.7}$$

Hence, we have related the measured ratio between the major and minor axes of the ellipse to the phase shift between two orthogonal polarizations.

3.2.2 Phase correction

Introducing other optical components into the beam path, will sometimes alter the phase state of the two orthogonal polarization components, thus changing the polarization state of the light from for example circular to elliptical. In the setup described above in Section 3.1.1 the beamsplitter that allows the laser to enter the objective is inducing a phase shift to the light. A phase shift so severe that the light that is circularly polarized ($\delta = 87°$) before the beamsplitter cannot reach more than elliptically polarized light with a phase difference of $\delta = 74°$. Rotating the QWP away from 45° does not compensate for this beamsplitter-induced phase shift. To mend this issue a method illustrated by Chou *et al.* is employed [67]. By inserting a HWP in sequence with the QWP in the optical path, as in Figure 3.7, the phase shift produced by the beamsplitter can be corrected for. This is done through an iterative process where the polarization state for each angular configuration of QWP and HWP is checked with the polarizer and power meter. For each position in increments of five degrees of the QWP, the HWP is rotated through its entire angular range (90 degree) in steps of five degrees and the polarization is checked. This process essentially means continuously, and controllably probing the

Poincaré sphere[2] for a configuration where the phase shifts from the QWP, HWP, and beamsplitter together will sum up to 90 degrees. Via this process, a polarization of the light at the specimen plane is reached that has a phase difference of 89 degrees between its two components.

The polarization after the beamsplitter was measured both before and after the objective without any difference. Therefore, it is safe to assume that the objective in itself conserves the polarization of the light well enough. However, if this was not the case, the polarizer/power meter configuration could easily have been placed after the objective instead, and the phase shift of the beamsplitter and objective could have been corrected for simultaneously.

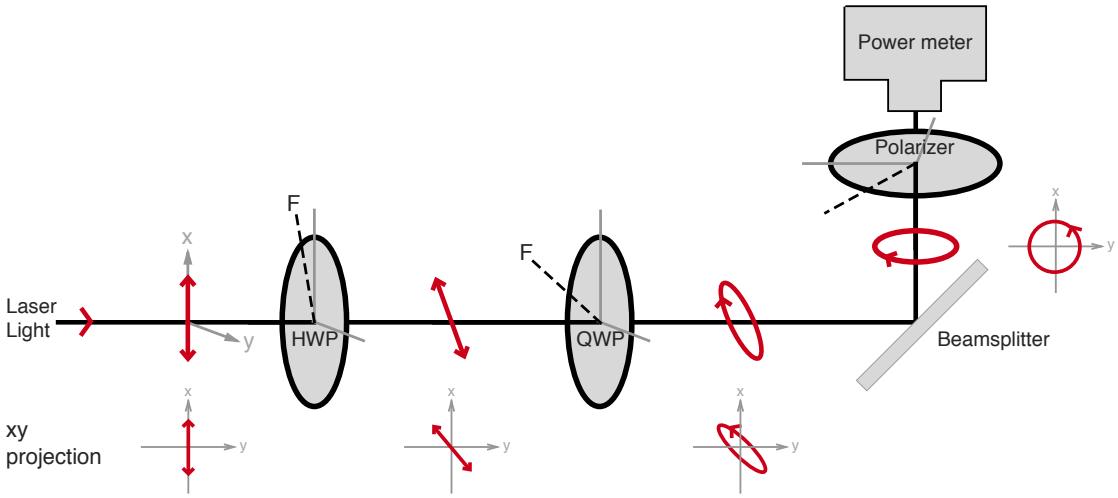

Figure 3.7: Illustration of the setup used to correct for the phase shift induced by the beamsplitter, as the laser light is focused at the sample plane. A half-wave plate in sequence with a quarter-wave plate is used to continuously probe the Poincaré sphere to find the combination of three phase shifts that add up 90 degrees (the F denotes the fast axis). A polarizer and power meter together are employed to check the outgoing polarization state of the laser by measuring the major and minor axis of the polarization ellipse. In the figure for simplicity we also display the xy-projection of the polarization state.

3.3 Nanorod selection criteria

To perform experiments on gold nanorods in optical tweezers it is necessary for the main LSPR peak (in this case being the longitudinal peak) to be on the blue wavelength side of the trapping laser, to produce an attractive gradient force [52]. We are using a 660 nm laser light and are thus limiting our selection of rods to low aspect ratio (AR) rods,

[2]The Poincaré sphere provides a graphical interpretation of the Stokes formalism for polarization, where each point on the sphere represents a unique polarization state; linear polarization states lie on the equator whereas right and left circular polarization states occupy the north and south poles, and in between are the elliptical states. An optical component subjecting the light to a phase shift can be viewed as to translate the polarization state across the Poincaré sphere. To study this further, see [68].

since the longitudinal LSPR red-shifts for increasing AR. The position of the transverse LSPR will also redshift for an increasing width of the nanorod. To maximize the LSPR peak separation it would then seem reasonable to choose a thin and long rod to get the optimal spectroscopic properties for this investigation. This is indeed true; however, one additional consideration is necessary. To reach stable trapping, the size of the nanoparticle cannot be too small. The increasing Brownian motion together with the decreasing drag force from the water environment will make small particles increasingly difficult to contain in the potential well created by the laser [15]. Hence, the optimal particle for this project is one that is small and long enough to have a sufficient spectral separation in a wavelength region lower than the trapping laser, and at the same time be wide enough to be stably contained in our optical potential well.

Figure 3.8 summarizes the search for an optimal particle and is presenting extinction spectrum measurements performed in a spectrophotometer (Cary 5000 UV-Vis-NIR) as well as SEM images for three nanorods, which each characterize one of the considerations expressed above. NR02 (blue) shows excellent trapping stability. However, the width of the particle is large, which produces an extinction spectrum with large overlap between

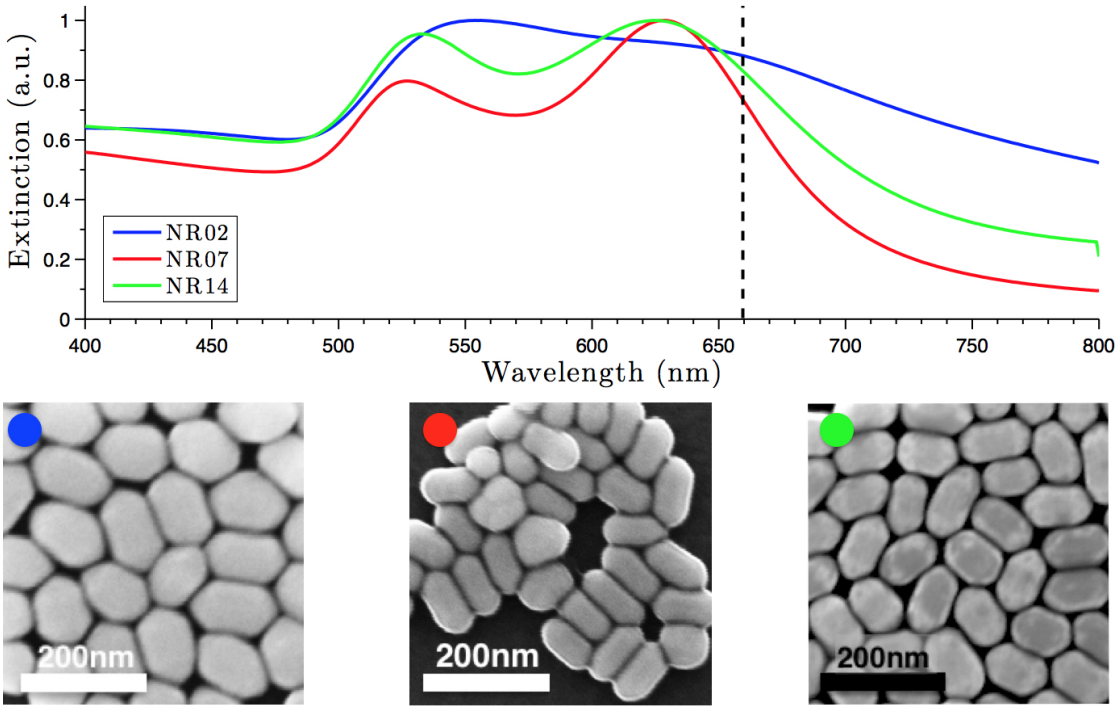

Figure 3.8: Extinction spectra together with SEM images of the corresponding particles. The dashed line in the spectral plot corresponds to the 660 nm wavelength of the trapping laser light. The larger, stably trapped, NR02 (blue) has a spectral shape that is suboptimal for our investigations because of the large overlap between the two LSPR. NR07 (red) has a very pronounced longitudinal LSPR; however, its small size makes it difficult to trap. NR14 (green) combines the two advantageous properties of the prior two particles; stable trapping characteristics and a rather distinct longitudinal LSPR. Hence, NR14 is the particle utilized in this study.

the two LSPR peaks, forcing us to discard it. NR07 (red) on the other hand demonstrates excellent LSPR peak separation, but is sadly too small to be stably trapped. NR14 (green) combines the two preferable properties of the previous samples, being stably trapped and still maintaining the LSPR peak separation enough to yield a distinct longitudinal peak. Hence, NR14 is the particle chosen for investigation in this project.

3.3.1 Selective shortening of nanorods

Nanoparticles used in this work have been synthesised by Dr. Lei Shao, using a wet-chemical method involving seed-mediated growth. The exact recipe and procedure of this process are not discussed in detail during this thesis, but are well described in references [4, 69]. The synthesis yields particles with a certain width and length depending on concentrations of different chemicals during growth. Despite some control over the width and length of the rod, it is not possible in this synthesis to obtain particles with an exactly predetermined size or aspect ratio. Luckily, the length of the nanoparticle and thus also the position of the longitudinal LSPR resonance can be tailored after growth by using an anisotropic oxidation procedure [70]. This process starts with a structure where the length of the nanorod is larger than the desired structure. 3 ml of initial nanorod solution, CTAB (0.1 M), HCl (0.8 M) and HAuCl4 (1 mM) are mixed. CTAB preferentially attaches to the body of the nanorod and to a lesser degree to the ends. Consequently, in this process it acts as a directional agent inhibiting etching on the sides of the rod more than on the ends. The acid in the solution will determine the speed of the process, and the gold salt will govern the oxidation and hence the degree of blue-shift of the resonance peak. The anisotropic etching process was monitored by continuously measuring the extinction spectrum of the particles in solution, and could be terminated by washing through centrifugation and re-dispersion in water as the desired longitudinal LSPR resonance had been obtained.

In Figure 3.9a) we see the extinction spectra measured for colloidal solutions of nanorods prior to, and after, the oxidation process. We observe that the longitudinal LSPR peak has been blue-shifted by around 50 nm. The transverse LSPR peak before the etching procedure is distorted from a plain Lorentzian curve shape, which is explained by inhomogeneities such as spheres and irregularly shaped particles. The etching and washing procedure homogenizes the colloidal solution resulting in the fact that the low-wavelength peak is becoming more symmetrical, stemming from a reduction of the polydispersity of the solution. The shift could easily be misinterpreted as a decrease in the width of the rod since the peak is apparently shifting. This is, however, not the case, which is verified by SEM imaging and measurement. In Figure 3.9b) we see SEM images taken before and after the oxidation process. These images confirm the spectral measurements by showing a rod with smaller aspect ratio after the oxidation. The dimensions of the particles prior to, and after the process are $115 \pm 7/65 \pm 4$ nm and $108 \pm 7/65 \pm 5$ nm, measured from 100 particles in each batch. The latter of these samples is NR14 from Figure 3.8, which is used in this study.

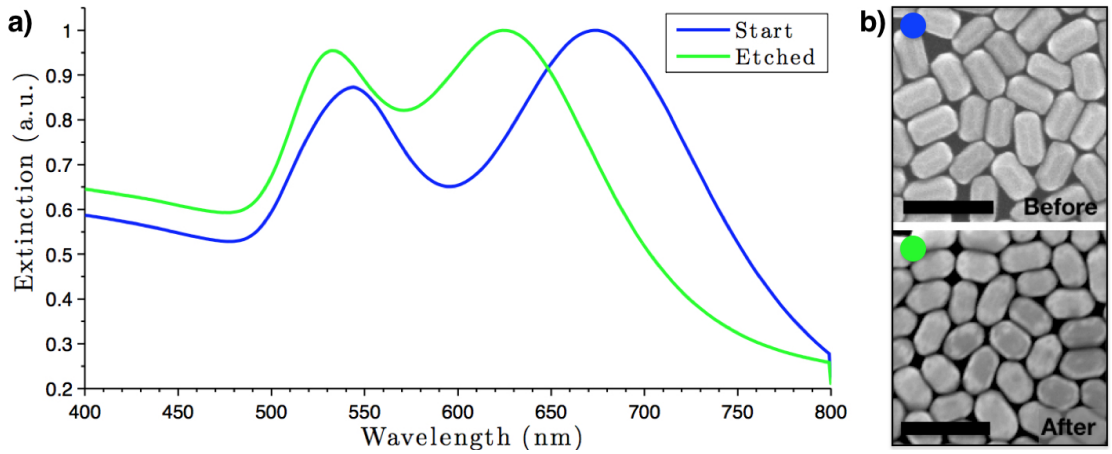

Figure 3.9: Selective etching of nanorods in solutions through the process of anisotropic oxidation. a) Extinction spectra taken before and after the etching process. The longitudinal LSPR blue-shifts from 673 nm to 625 nm. This indicates a shortening of the length of the rod and a decreased aspect ratio. b) SEM images taken before and after the etching process also show a shortening of the gold rods. Before the process the particles have the dimension $115 \pm 7/65 \pm 4$ nm, and after $108 \pm 7/65 \pm 5$ nm.

3.4 Trapping stiffness measurement

To measure the oscillations in position of the trapped particle, some type of position sensitive detector should be used. A setup that has become common in the optical tweezers community is the quadrant photodiod (QPD) setup, which allows for high bandwidth measurements of the positional fluctuations. In that configuration four light sensitive detectors are assembled in a square pattern. Thereafter, the position is extracted from subtracting intensity counts between separate detectors [58].

Another simply implemented method for measuring the position fluctuations of a trapped particle is to record high-speed video of the particle and extract the position of the particle for each frame of the video. This is the method that is utilized in this thesis. The mirror that directs light either to the spectrometer or the CMOS camera, as can be seen in Figure 3.3, is arranged so that light is passed to the CMOS camera. Thereafter, a particle is trapped by the optical tweezers at a certain constant laser power and a video of the trapped particle is recorded for 30 seconds. This is repeated for several particles and for linearly increasing power.

After the video recording of positional fluctuations for the particle is recorded, the exact position of the particle is determined by calculating the intensity weighted centroid in the x- and y-directions for each frame. This positional data is Fourier transformed, and the Lorentzian power spectrum is fitted to Equation (2.25) and the corner frequency is determined, in a MATLAB-program presented in [71]. The trapping stiffness of the optical tweezers for this particular type of particle can now be calculated as described in Section 2.2.2.

3.5 Single nanoparticle spectroscopy

There is a wealth of different spectroscopic methods. Each method can be classified from the nature of the interaction between the radiation and the medium in that particular case [72]. For LSPR sensitive spectroscopy, measurements can be made either on an array of nanoparticles [73] or a single nanoparticle [74]. In this project, the latter of these is the method employed. Working with plasmonic nanoparticles on a transparent surface the most commonly used method for both illumination and spectroscopy is the dark-field (DF) configuration, because of the strongly enhanced scattering of plasmonic particles.

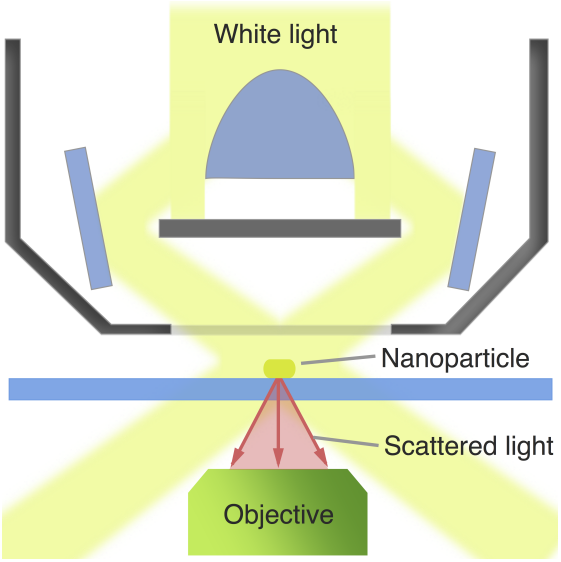

Figure 3.10: In dark-field spectroscopy, light is passed through a dark-field condenser and incident on the nanostructure of interest at a high angle. Light scattered at an angle inside the collection cone defined by the numerical aperture of the objective will be collected. The obliquely incident illumination light will, however, be excluded from the detection since it is outside detection cone of the objective. Hence, the criteria for DF illumination becomes $\mathrm{NA_{obj}} < \mathrm{NA_{cond}}$.

3.5.1 Dark-field scattering spectroscopy

Dark-field (DF) scattering spectroscopy is extremely powerful for single particle spectroscopy. White light is passed through a dark-field condenser (high numerical aperture, here 1.2-1.43), which will direct the light to the sample at a high angle. Together with this, an objective with NA smaller than the condenser's is used ($\mathrm{NA_{obj}} < \mathrm{NA_{cond}}$). The incoming light that scatters from the studied nanoparticle will be collected by the objective and passed to a spectrometer extracting a scattering spectrum. The direct light from the source will be omitted since it is not possible for the objective to collect it [7]. This setup yields a spectral measurement setup that has a low background and good signal to noise ratio. A schematic illustration of this can be seen in Figure 3.10.

3.5.2 Calibration of spectra

In the ideal case, the white excitation light would be equally intense for all wavelengths contained in the light; thus, providing a correct scattering spectrum instantly. Sadly this is not the case in any experimental environment, and the white light spectrum will have some intensity variations depending on wavelength. In the setup constructed in this project the white light spectrum is by estimate Gaussian with a peak at around 690 nm, see the blue curve of Figure 3.11.

Moreover, to further increase the signal to noise ratio one utilizes a reference or background spectrum that is removing stray light and other noise sources that are not related to the scattering of the particle itself. This is obtained by recording a spectrum in a similar position as where the measurement is planned to take place, see the green curve of Figure 3.11. The background spectrum is noticed to be considerably noisier than the white light signal. This is a result from the strongly reduced count rate of the background signal produced in the DF scattering configuration.

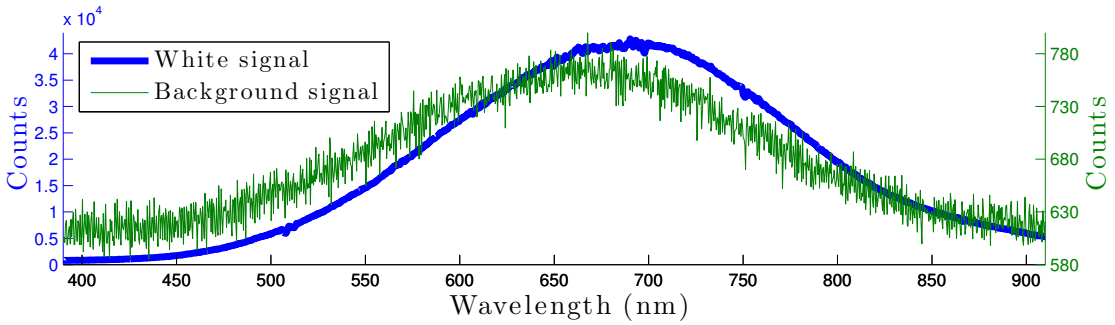

Figure 3.11: Two spectral measurements used to calibrate the final single particle scattering spectrum. The blue graph represents the white light spectrum from the excitation light used in the illumination and spectroscopic ray path of the setup. The spectrum is approximately Gaussian and has an intensity maximum around 690 nm. The green curve displays the background spectrum with the laser turned off. It contains significantly more noise than the white signal owing to the much lower count rate of the signal, making shot noise more pronounced.

Hereafter, by using the recorded white light spectrum ($I_{\text{white}}(\lambda)$) and background spectrum ($I_{\text{ref}}(\lambda)$) we can obtain a calibrated correct scattering spectrum ($I_{\text{scatt}}(\lambda)$) from the raw scattering data ($I_{\text{raw}}(\lambda)$) by subtracting the background and normalizing the spectrum with the white light spectrum data at each wavelength, according to

$$I_{\text{scatt}}(\lambda) = \frac{I_{\text{raw}}(\lambda) - I_{\text{ref}}(\lambda)}{I_{\text{white}}(\lambda)}. \tag{3.8}$$

From this analysis we obtain a spectrum as the green curve in Figure 3.12, which can be seen to have a distinct longitudinal resonance peak as well as a bump corresponding to the transverse LSPR peak.

3.5.2.1 Self-fluorescence of glass slide

Fluorescence in general is a process where incident light is absorbed by a structure and almost instantly (after $10^{-9} - 10^{-7}$ s) re-emitted again at a wavelength longer than the incident light. This process is used extensively in many different imaging and labeling applications by incorporating dedicated fluorescent entities in the sample. However, at sufficiently high light intensities even objects in the optical path that are not stained with these fluorescent elements can absorb light and emit this in a fluorescent manner, called self-fluorescence (or autofluorescence) [62, 75]. In the configuration applied in this project, a high intensity laser beam is focused to a diffraction limited spot. The intensity of the light in the focal spot of the trap is enough to excite self-fluorescence of the glass against which the particle is trapped and rotated.

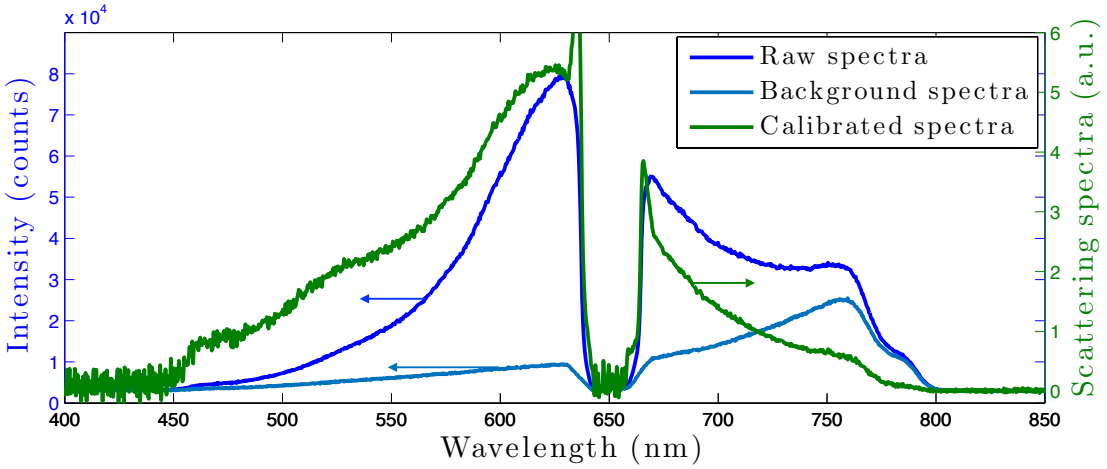

Figure 3.12: Raw data spectrum (blue), background spectrum containing self-fluorescence (light blue) and calibrated spectrum (green) for a single measurement. The focused laser beam is producing autofluorescence radiation from the glass slide, which is strong enough to distort the measured DF scattering spectrum. Therefore, spectra for a laser power sweep with an empty trap are recorded to create a library of background signals for different laser powers, which can continuously be subtracted for the current trapping power. The dip in the spectrum around 660 nm is a result of the notch filter blocking these wavelengths of light in the optical path.

The self-fluorescence of microscope slides is a huge issue when working with single particle scattering spectroscopy since it will distort the recorded spectra and render any post-experiment data-analysis pointless. Hence, the issue needs to be addressed. One option to minimize self-fluorescence is to purchase special glass slides, which are optimized to have low fluorescence (e.g. Ted Pella provides a microscope slide that they claim performs well in this respect). However, since the laser beam is highly focused and intense there is a risk that the effect will still be present. The second alternative, the one used in this study, is to record the self-fluorescence spectrum as part of the background and calibrate the measurement with it. This is simple enough for light at constant power, though for an experiment where the laser power is varied it demands some more thought. To solve this, before the actual experiment is performed, we record

self-fluorescence spectra for a complete laser power sweep in an empty trap to generate a library of background signals. Then, during data-analysis we can continuously subtract the background corresponding to the present laser power. Normalized raw spectrum and corrected spectrum, together with the self-fluorescence spectrum itself for one laser power is seen in Figure 3.12.

3.6 Determination of LSPR peaks

As the DF scattering spectrum is recorded it is necessary to determine the positions of the two LSPR peaks supported in the gold nanorod. This is done to extract valuable information from the measurement, especially during continuous measurements when the spectral properties of the nanorod is expected to change, depending on environmental or morphological changes.

The spectrum is recorded in wavelength regime so the first step in calculation becomes to convert it to energy scale since the Lorentzian description of the LSPR peak is, as we saw from Equation (2.2) described in Section 2.1.1, done in frequency domain, which maps linearly to energy (whereas inversely to wavelength). We obtain the following expression for this conversion

$$\begin{cases} E = h\nu \\ c = \nu\lambda \end{cases} \Rightarrow E = \frac{hc}{\lambda} \approx \frac{1240\,[\mathrm{Jm}]}{\lambda}. \tag{3.9}$$

We define a model function as a bi-Lorentzian equation since two separate peaks related to the longitudinal and transverse plasmon oscillations are observed. Also, a linear term is added to the model function. This linear term serves as a first approximation to accounts for the interband transitions at short wavelengths, as discussed in Section 2.1.1.4. The entire expression reads

$$I(E) = I_0 + kE + \frac{2}{\pi}\left(\frac{A_1 G_1}{4(E-a_1)^2 + G_1^2} + \frac{A_2 G_2}{4(E-a_2)^2 + G_2^2}\right), \tag{3.10}$$

where E is the energy, I_0 is a baseline intensity, k the slope of the linear term, A_i are intensity maxima, G_i the full width at half maxima (FWHM) and a_i the peak positions of the two Lorentzian peaks. We hereafter deselect the energy range where the notch filters are blocking the laser light ($1.85 - 1.97\,\mathrm{eV}/630 - 670\,\mathrm{nm}$) and employ a non-linear regression model in MATLAB with Equation (3.10) as a model function to fit the measured normalized DF scattering spectrum. In Figure 3.13 a fitted spectrum is seen together with the fitting components. In this spectrum, the peak positions are determined within a 95% confidence intervals to be $539.2 \pm 1.1\,\mathrm{nm}$ and $594.7 \pm 0.6\,\mathrm{nm}$ respectively. The peaks are found to have FWHM within a 95% confidence intervals of $93.9 \pm 3.6\,\mathrm{nm}$ and $84.7 \pm 2.3\,\mathrm{nm}$. The fit has a coefficient of determination (R^2) of 0.9988. The confidence intervals as well as R^2 are calculated to check the validity of each fit and a spectral measurement is discarded if any of these properties are atypical.

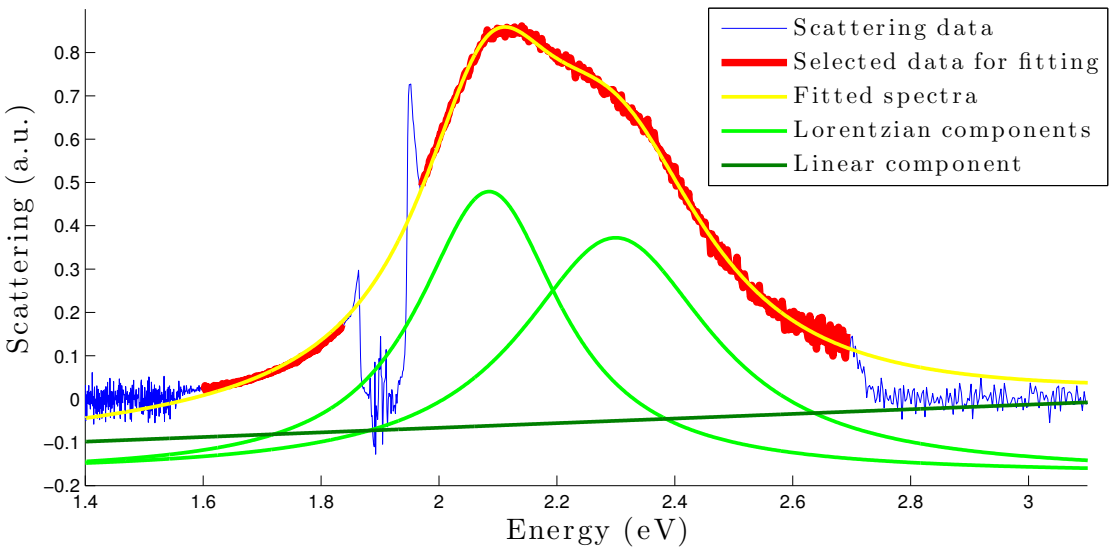

Figure 3.13: Normalized DF scattering spectrum from a trapped rotating nanorod. The energy range that is blocked by the notch filter is deselected. The spectrum is fitted by a bi-Lorentzian model function with a linear interband transition correction term. The fit is shown in yellow. The three components to the fit are seen in green.

Single particle DF scattering spectrum from 20 trapped particles are recorded, and the mean value and standard deviation for the longitudinal and transverse peak positions are determined to $601.3 \pm 6.4\,\text{nm}$ and $535.5 \pm 4.5\,\text{nm}$. There is an apparent difference between the longitudinal LSPR position extracted from these DF spectra compared to the ensemble extinction measurements performed in the spectrophotometer, where the longitudinal peak position can be estimated in Figure 3.9 to be at 620 nm. The reason for this discrepancy is possibly that during extinction measurements the density of particle in solution is high, necessitating a high CTAB concentration to stabilize the colloidal suspension. CTAB has a higher refractive index than plain water and the LSPR peaks will therefore red-shift. Furthermore, particles that provide the best rotational and spectroscopic properties are selectively trapped. In this selection process particles that have longitudinal resonances closer to the laser line might be discarded owing to worse rotational or spectroscopic properties.

3.7 Experimental procedure

Particles are strongly diluted in DI-water to a concentration where trapping of multiple particles is avoided. Around $4\,\mu\text{L}$ of the dispersion is transferred to a microscope cover glass/objective glass geometry with a $100\,\mu\text{m}$ spacer in between. The sample is put in the optical path, and trapping and rotation against the top glass surface is performed in the setup described above.

A particle is selected through observation in the DF imaging system, and thereafter

the laser is unblocked and allowed to enter the objective, effectively creating the optical tweezers. Through a series of stage movement and focus corrections the chosen particle can be pushed up to the upper glass surface. A PFS (Perfect Focus System) with a predetermined focus for optimal trapping stability is then turned on and final corrections are made to the stage to make the particle enter the laser beam and become stably trapped. As the particle is trapped, one DF scattering spectrum as well as an autocorrelation signal is collected to verify that the trapped particle is in fact a gold nanorod and that it has reasonable spectroscopic and rotational properties. The spectrometer and autocorrelator are thereafter started to continuously record data.

To investigate properties such as long-term reshaping as well as temperature effects of the trapped and rotating particles continuous measurements are performed. During these extended measurements autocorrelation signal are recorded once every 1.2 seconds, which is as fast as the instrument allows, whereas a DF spectrum is recorded every 1.3 seconds. The time between the spectral measurements is dependent on the operator-set exposure time for the spectrometer, which here is set to one second to obtain a good signal-to-noise ratio.

To probe the steady state characteristics of trapped particles, measurements are performed for an extended time with a constant laser power. Long-term dynamic effects are studied in two different laser power ramping schemes being; a single triangular ramp (blue curve in Figure 3.14) as well as consecutive triangular ramps with linearly increasing maxima (green curve in Figure 3.14). Here, the power ramps are plotted against steps, and during the experiment the time at each step is user-specified. The overall maximum power of the triangular ramps is chosen to be just below the critical power of the trapped particle. This critical power is defined as the power where the particle is subjected to an amount of laser power high enough for it to become stuck on the glass which it is rotating against, effectively terminating the experiment. This power varies from particle to particle, but an estimate can be made by averaging results from previous particles.

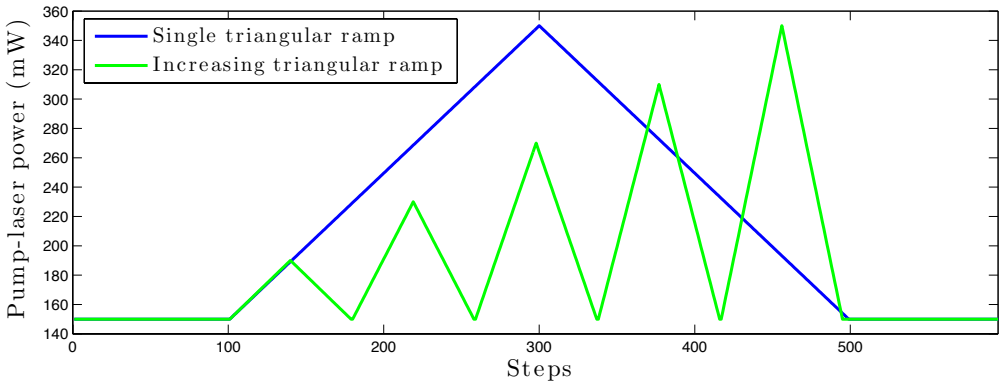

Figure 3.14: Triangular power ramp schemes that are utilized to study the long-term dynamic heating and reshaping effects of trapped particles. A single triangular ramp (blue), and consecutive triangular ramps with a linearly increasing maximum (green).

4

Results and Discussion

The result and how it is interpreted is the keystone to every investigation. It is what the previous chapters have been building up to. Physics in general is a quantitative research field. The beauty of such is that the results obtained through a properly performed experimental study and analysis should be considered the truth until another result is attained that contradicts it. Researchers who might distrust the correctness of the results can recreate the well-described experimental procedure and should attain the same results if they are in fact correct.

In the chapter below we present initial characterization of the constructed optical tweezers setup, to verify the quality of the trap and ensure that the planned investigation can continue. Thereafter, some interesting findings regarding the rotational dynamics autocorrelation measurements are introduced and discussed. Hereafter, results from the main investigation about spectroscopic studies of optically trapped and rotating gold nanorods are presented. These results are discussed in detail with respect to photothermal processes, reshaping and other effects necessary for a complete understanding of the system.

4.1 Trapping stiffness measurement

To verify the quality of the constructed optical tweezers, the trapping stiffness for the particle of interest is measured. Positional oscillations were recorded with the CMOS camera for five particles at a constant power of 3.9 mW and for one particle the laser power was swept from 3.9 to 6.85 mW. Following that, the xy-oscillation data was extracted according to the procedure established in Section 3.4. In Figures 4.1a) and 4.1b) position fluctuation distribution data recorded in the x- and y-directions for a trapped and rotating nanorod are displayed. The distributions are fitted to normal distributions and the correspondence is high. In Figure 4.1c) and 4.1d) the translation Brownian motion data has been Fourier transformed and in frequency domain the power spectrum is fitted to a one-sided Lorentzian curve to extract the corner frequency in both directions.

Since the particle is rotating fast, the translational Brownian motion of the nanorod is estimated to be close to that of a spherical particle with the radius that is the mean value of the length and width of the rod. Hence, the calculations of trapping stiffness for a rotating nanorod are performed as for the spherical case discussed in Section 2.2.2. Since the particle used has the average dimensions 108/65 nm, we estimate it as a sphere

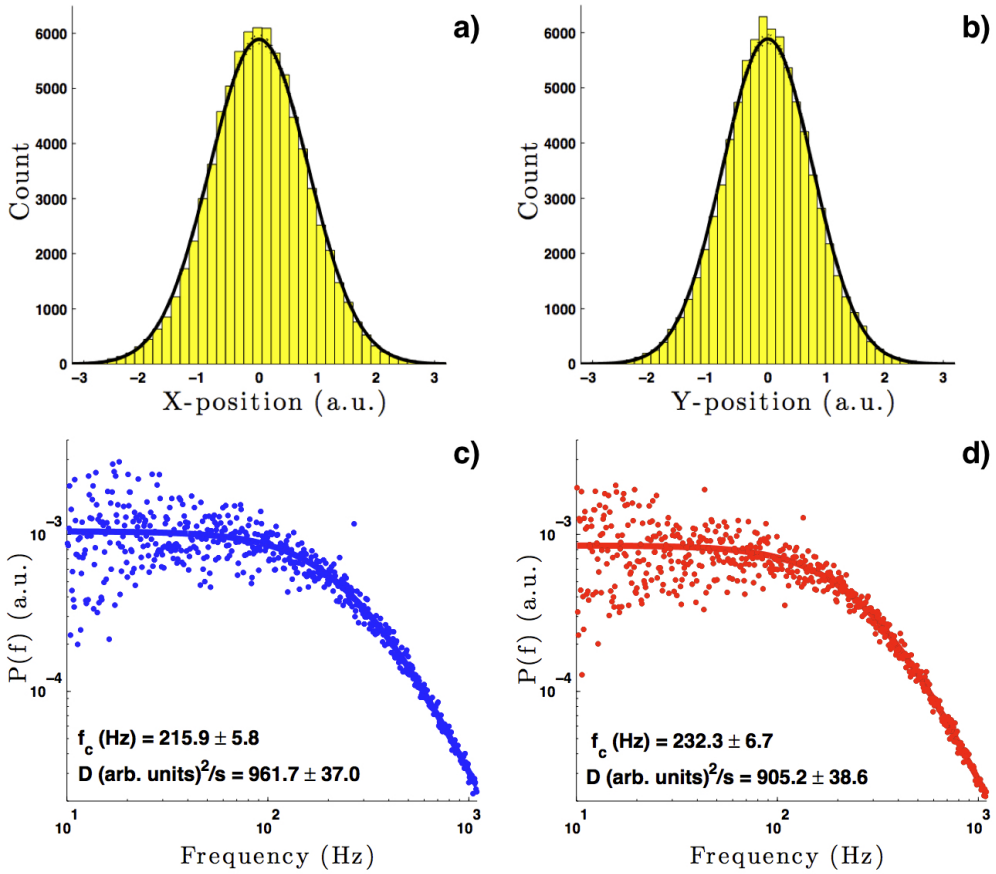

Figure 4.1: Data recorded with the CMOS camera for a trapped particle. a) and b) give position distributions in the x- and y-directions (in units of pixels on the CCD of the camera). These distributions are fitted with good agreement to Gaussian distribution curves. In c) and d) power spectra in the x- and y-directions are displayed together with fitted Lorentzians. From the fit the corner frequency is determined, which can be used to estimate the trapping stiffness.

with diameter $\frac{108\,\text{nm}+65\,\text{nm}}{2} = 86.5\,\text{nm}$. The exact distance between the particle and the surface against which it is rotated is not known, and an investigation regarding this should be executed. Scattering forces are pushing the nanorod towards the water-glass interface; however, no restriction in movement of the particle due to the glass is observed. For this reason, we can assume that the particle is nearly in contact with the glass slide, but there exists a non-negligible distance separating the nanorod from the glass. A separation of 5 nm is assumed in subsequent calculations as a representative value. With these two quantities β_{surf} is estimated from Equation (2.28), and the trapping stiffness k is found.

For the five particles trapped at 3.9 mW power the mean value for the trapping stiffness is calculated to be $k_{\text{x}} = 1.16 \pm 0.08 \cdot 10^{-3}\,\text{pN/nm}$ and $k_{\text{y}} = 1.25 \pm 0.07 \cdot 10^{-3}\,\text{pN/nm}$. The results of the power increase for one particle is summarized in Figure 4.2 and we notice a linearly increasing relation between the

trapping power and the stiffness. The second interesting feature of this graph is that k_y is consistently slightly larger than k_x. The difference is explained by a minor deviation from 90 degree phase difference between the two polarization components of the trapping light, resulting in a small deviation from circular polarization into elliptical polarization. This leads to a reduced trapping stiffness along the major axis of the ellipse (which seems to be close to the x-direction in this case) and will also result in larger oscillations of the particle in this direction. Upon reexamination of the position distributions in Figure 4.1a) and 4.1b) it is noticeable that the distribution in the x-direction is marginally broader.

Furthermore, it is acknowledged that the error bars for the trapping stiffnesses are becoming larger as power increases. This likely stems from the fact that at higher laser power the stiffness of the trap is larger, and the corner frequency of the power spectrum will be pushed into higher frequency regions. The problem with using a CMOS camera instead of a QPD is that the sampling rate of the camera is significantly lower. As the corner frequency is increasing, it is getting closer to the sampling frequency of the CMOS, and thus important data after the corner of the Lorentzian is lost and the error bars from the fit are expected to increase.

These values for trapping stiffness can be compared to previously measured values for trapping stiffness performed in works such as [22, 27]. It is noted that the values obtained through this analysis are almost one order of magnitude larger than prior results. It should be noted that the measurements our results are compared to are collected from

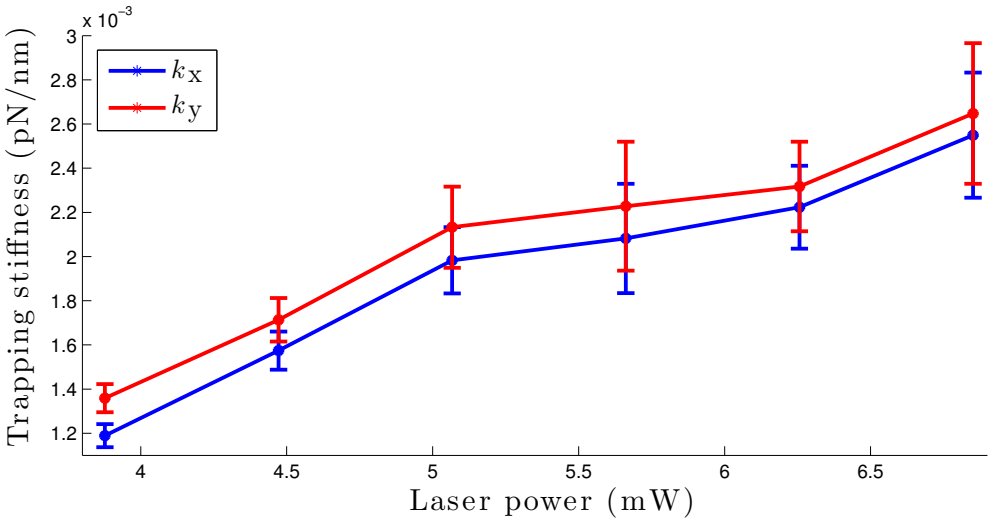

Figure 4.2: Trapping stiffness in the x- and y-directions determined for a particle trapped at powers that are linearly increasing from 3.9 to 6.85 mW in six steps. The stiffness is approximately linearly increasing with increasing laser power. It is noted that the y-direction stiffness is consistently slightly larger than the x-direction stiffness. This is attributed to a polarization state of the laser that is deviating a bit from perfectly circular polarization, resulting in a lower trapping stiffness in the direction of the major axis of the polarization ellipse.

gold particles trapped in 3D. The proximity to the surface in our experiments leads to increased hydrodynamic drag and thus a higher trapping stiffness than the one measured in a 3D trapping geometry is expected. Moreover, the spectral separation between the trapping laser and the LSPR resonance will affect the stiffness. The fact that the laser is trapping almost at resonance in our experiments will increase the trapping stability, compared to prior results where a detuned laser is used. To the author's best knowledge, trapping stiffness measurements on trapped gold nanorods in the 2D geometry utilized here has not been reported in the literature, and hence no comparison to such results can be made.

The measured trapping stiffnesses lead us to trust the constructed trap for this specific particle batch since it is established that it has a comparably and sufficiently good trapping stability. Thus, the further planned experiments are continued using this setup.

One could argue that to make better statistics for the trapping stiffness additional data should be collected. However, it should be noted that during the 30 second measurement needed to generate one power spectrum 80000 images are taken. The data processing time needed to obtain a trapping stiffness measurement from these 80000 images is about five minutes on an ordinary computer. Consequently, the number of measured particles and powers had to be limited. Yet, considering the purpose of the measurement is solely to verify the quality of the constructed optical trap the number of particles and powers measured are considered sufficient.

4.2 Autocorrelation analysis

An integral part of the final experiment, to continuously and parallelly probe the rotational dynamics and the spectral changes of the particle, is the autocorrelation data analysis. During the experimental work it was found that by controlling the diameter of the fiber core, different correlogram were obtained. The different possible information included in the autocorrelation signal is discussed in the following section and in relation to experiments conducted in [23, 25].

4.2.1 Fiber size dependence

As mentioned above in Section 2.3.2 the decay of the autocorrelation function provides information about the fluctuation of the rotary motion due to rotational Brownian motion. The autocorrelation function usually oscillates around $C(\tau) = 0$ as the blue curve in Figure 4.3. However, during the run of these experiments it is noticed that if one decreases the fiber core diameter from $400\,\mu$m to $62.5\,\mu$m the oscillation of the autocorrelation signal is pushed up from the x-axis, as for the red curve in Figure 4.3. This is understood as the fact that not only rotational but also translational Brownian motion is detected in the thin fiber case. The particle will not be immobilized in the potential well it is subjected to. Rather, it will oscillate or perform a random walk in the trap, characterized by its translational Brownian motion. As the fiber core diameter is de-

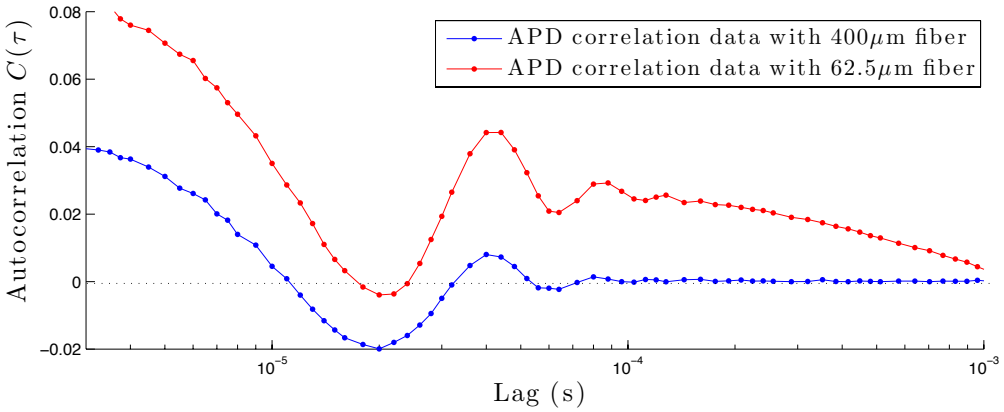

Figure 4.3: Autocorrelation signals from scattering of a rotating nanoparticle recorded using fibers with a small (62.5 μm) as well as a large (400 μm) core diameter. For the thick fiber the autocorrelation is oscillating around $C(\tau) = 0$ whereas in the thin fiber case the signal is pushed up into the upper right quadrant of the coordinate system, oscillating while it is decaying close to $C(\tau) = 0$ as the lag time increases. The lines connecting the data points serve as guides for the eye.

creasing, the collection area for scattered light is decreasing. If the particle, during its translational Brownian motion in the trap, is traveling outside the detection volume this will result in a decrease in the collected intensity at that time. This will be reflected in the autocorrelation signal as a decaying signal, where the length of the decay will be related to the characteristic time of the translational Brownian motion of the particle in the trap. The two cases are illustrated schematically in Figure 4.4a) and 4.4c). In Figure 4.4b) and Figure 4.4d) images emphasising the difference in sizes between the two fiber spots are displayed. These were recorded by coupling laser light to the exit of the fiber and imaging the reflection from a glass surface with the CMOS camera. The scale bars in these two images are 2 μm. Therefore, the width of the collection area is estimated to 8.9 μm and 1 μm for the large and small fiber respectively.

Regardless of fiber diameter the rotational Brownian motion decay term will always be present (as long as an autocorrelation signal is detected and the particle is rotating) since it is a property localized at, and intrinsic to the particle. However, information about the translational Brownian motion will be lost if a large collection volume is used and the translational oscillation of the particle in the potential well is always inside the collection volume.

In the trapping experiments performed during this thesis the translational Brownian motion is found to be occurring on a time scale that is about one order of magnitude larger than the rotational Brownian motion. Hence, the complete autocorrelation collected from a small fiber is including information on the complete motion of the particle in the trap. The signal is built up of a slow exponential decay combined with an oscillatory exponentially decaying signal that is decaying on a shorter timescale.

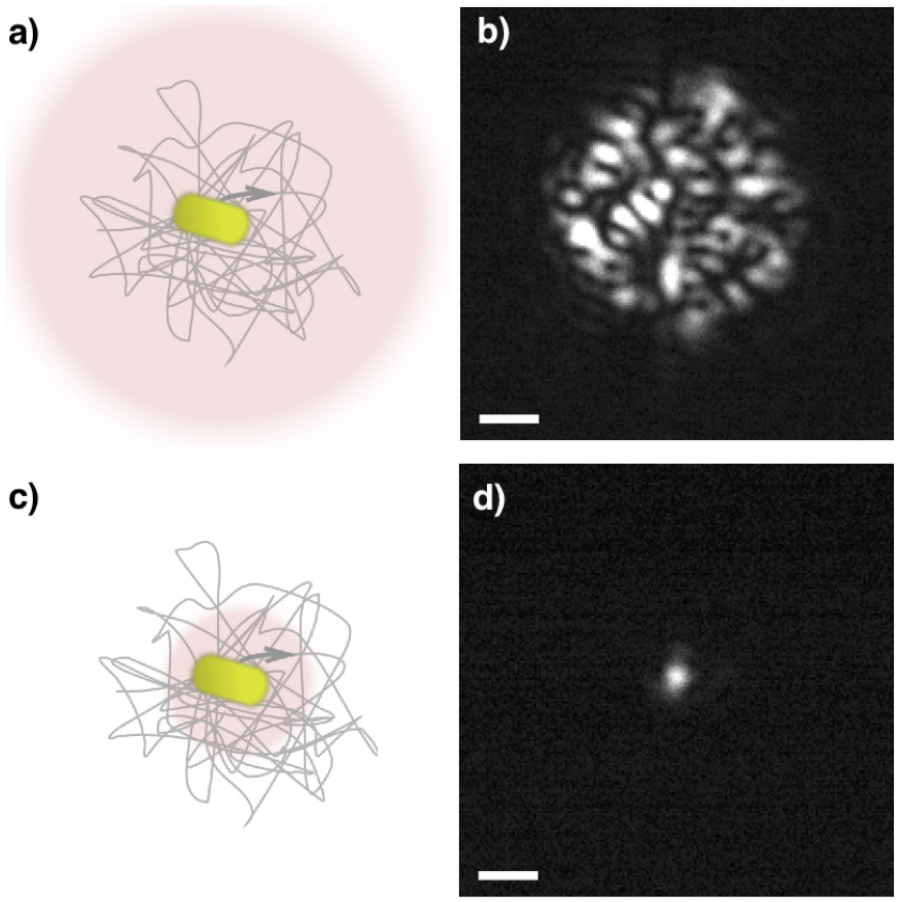

Figure 4.4: Two different fiber core diameters and thus collection volumes. Schematic illustrations for the fiber size with respect to translational motion of the nanorod (a and c). Images of fiber spot as laser light is coupled in from the back of the fiber (b and d). The scale bar in these two images is 2 μm and the diameter of the collection area can hence be estimated to 8.9 μm for the large fiber and 1 μm for the small. For the large fiber the translational motion in the trap will always be contained within the sensitive region. However, for the small fiber the translation will at times move the particle outside the detection region and hence lead to an intensity oscillation, characteristic to the translational Brownian motion. It should be mentioned that the apparent size difference between the collection area and the particle is not to scale. The size of the particle is strongly increased for the sake of the illustration.

4.2.1.1 Correction to autocorrelation fitting equation

Due to the deviation from oscillation around zero correlation of the autocorrelation signal, which results from decreasing the fiber diameter, it is no longer possible to obtain a good fit to the model previously used (Eq (2.34), Section 2.3.2). To mend this issue the model is modified by adding an additional term that account for the intensity variations due to translational Brownian motion. If we assume that the rotational and translational components of the Brownian motion are uncorrelated this should be done in an additive

fashion and the new model function obtained becomes

$$C(\tau) = I_0^2 + \frac{I_1^2}{2}\exp\left[-\frac{\tau}{\tau_{\text{rot}}}\right]\cos(4\pi f_{\text{avg}}\tau) + \frac{I_2^2}{2}\exp\left[-\frac{\tau}{\tau_{\text{trans}}}\right], \tag{4.1}$$

where the τ_{rot} is the decay time of the exponential decay associated with the rotational Brownian motion whereas τ_{trans} is the decay time of translational motion. In Figure 4.5 fitting has been performed on data collected with the small fiber using both the herein proposed model function and the previous equation for only rotational Brownian motion. The correspondence between Equation (4.1) and the measured data, compared to the Equation (2.34) shows a considerable improvement from a fit with $R^2 = 0.9628$ to one with $R^2 = 0.9994$. Furthermore, the determination of parameters gives, for the updated (previous) model, a rotation frequency of $10091 \pm 43\,\text{Hz}$ ($9641 \pm 410\,\text{Hz}$), a rotational autocorrelation decay time of $35.94 \pm 0.85\,\mu\text{s}$ ($27.86 \pm 4.97\,\mu\text{s}$) and a translational autocorrelation decay time of $661.28 \pm 29.60\,\mu\text{s}$ (not described in the model). The uncertainties are corresponding to a 95% confidence interval calculated from the fit and are seen to be considerably lower for the herein proposed model function fit.

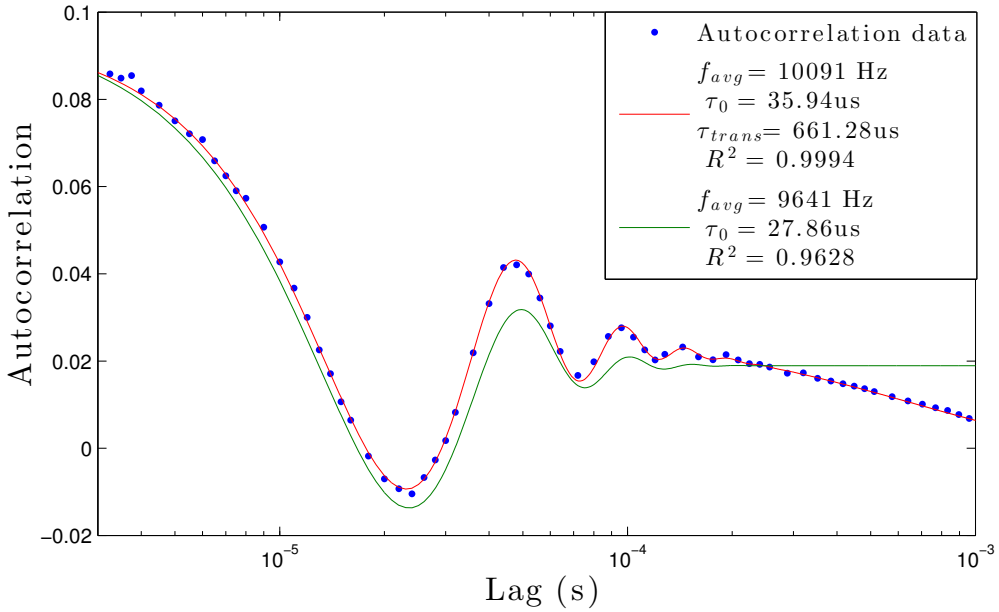

Figure 4.5: Data from autocorrelation of scattered light collected with a thin fiber from a rotating particle and fitted with the two different models, the herein proposed Eq(4.1) as well as the previous Eq(2.34). From these two model functions it is seen that the first one (red curve) fits the measured data to a much higher degree, with $R^2 = 0.9994$, than the second (green curve) that has a $R^2 = 0.9628$.

4.3 Parallel continuous measurements

Measurements described in Section 3.7 are conducted with the setup as in Figure 3.3. Results for the three unique cases investigated are presented in the subsections below.

A large amount of data is generated for each run of the experiment including scattering spectra and autocorrelation signals. These data-sets are processed according to above described methods to extract information such as the shift of the longitudinal and transverse LSPR peak as well as rotation frequency and correlation times. The time evolutions of these four quantities are presented in graphs below. For the ease of reading a selection of the more detailed experimental data is presented in Appendix A. Several particles have been measured and displayed similar properties as the ones presented below. The specific measurements displayed below were selected since they nicely illustrate the properties studied.

4.3.1 Constant laser power

In Figure 4.6 the time evolution of spectroscopic as well as rotational and temperature properties of a gold nanorod trapped at constant laser power are presented, specifically the peak positions of the two LSPR resonances (4.6a and 4.6b) and the rotation frequency (4.6c) and calculated temperature from the autocorrelation decay time (4.6d). During the length of the measurement a constant red-shift of the longitudinal LSPR peak and blue-shift of the transverse LSPR peak are seen, together with a decrease in the rotation frequency and calculated surrounding temperature.

This is a steady state process regarding energy flux from the laser; hence, no changes in the environment containing the particles are expected that can explain these shift. Since the quantities are demonstrating a continuous change the most reasonable explanation to this behaviour is a constant migration of surface atoms of the gold rod from the ends to the waist of the rod, essentially reshaping the rod towards lower AR. Lowering the AR, still maintaining constant volume, would result in the observed spectral shifts presented in Figure 4.6. Also, as the peaks are shifting in this fashion the rotational speed and temperature are expected to decrease since the rod is more resembling a sphere and the longitudinal LSPR is moving away from the wavelength of the trapping laser, hence producing less heating and optical torque.

Assuming that the reshaping and LSPR peak shift will continue at this constant rate as in Figure 4.6a) and that the volume of the particle is conserved, the time until the particle has fully reshaped into a thermally stable sphere can be estimated. For this estimation we model our nanorod as a cylinder that is capped with hemispherical ends, and its volume can therefore be calculated as

$$V = \pi \left(\frac{D}{2}\right)^2 (L - D) + \frac{4}{3}\pi \left(\frac{D}{2}\right)^3 = \frac{\pi}{12} D^2 (3L - D), \tag{4.2}$$

where $D = 65\,\text{nm}$ is the width of the nanorod and $L = 108\,\text{nm}$ is the total length of it, determined from SEM-images. A sphere with the same volume as the starting rod calculated with Equation (4.2) would have a diameter of about 82 nm. Hereafter we

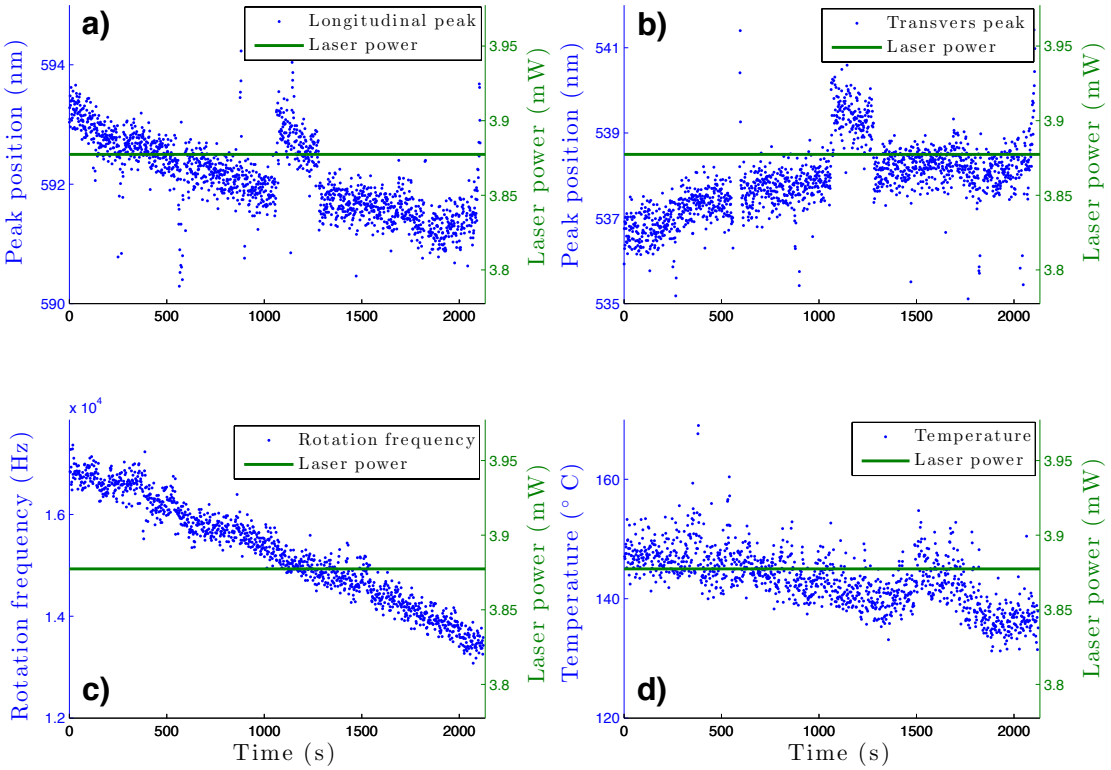

Figure 4.6: A trapped rotating nanorod in constant laser power tweezers. The figure shows time evolution of the four parameters; longitudinal (a) and transverse (b) LSPR peak positions as well as rotation frequency (c) and calculated temperature (d). A continuous blue-shift of the longitudinal, red-shift of the transverse LSPR, as well as decrease in the rotation frequency and temperature is observed.

utilize Equation (2.3) to estimate the scattering cross section of this gold sphere and find it has a plasmon peak at a wavelength of 572 nm. From Figure 4.6a) reshaping of the rotating particle in the trap results in a longitudinal LSPR peak shift of about 3.8 nm/h and starting from a peak position of 591 nm. Hence, we estimate that the trapped particle will become a sphere in $\frac{591\,\text{nm}-572\,\text{nm}}{3.8\,\text{nm/h}} \approx 5\,\text{h}$. This can be compared to the results presented in [39] where rods reshape to spheres due to thermal heating on the time scale of several hours, similar to this estimate[1].

During the time interval $t = 1170 - 1280\,\text{s}$ a step in the peak positions is observed in both the longitudinal and transverse peaks. These are attributed to a small contamination particle that is observed being simultaneously trapped with the gold particle. Upon realization that this unwanted particle was in fact also trapped (at $t = 1280\,\text{s}$) the stage was moved to where the measurement was no longer affected by it. However, instead of

[1]It should be mentioned that these particles had the average length of 73 nm, which is significantly smaller than the particles studied in this project. The size does certainly play an important role in relation to the reshaping times and heating properties.

discarding the entire measurement at this point this event in a nice way demonstrates the sensitivity of the resonance peaks of the interrogated structure to its environment.

The particles in colloidal solution are stabilized by the surfactant molecule cetyltrimethylammonium bromide (CTAB) that forms a layer around the particle, protecting it from aggregation. One could argue that the continuous longitudinal LSPR blue shift observed is not due to the reshaping of the nanorod in the trap, but rather a continuous desorption of the surfactant molecules from the surface of the nanorod. The first strong argument against this theory is as follows: If desorption of molecules was the case, it would lead to a change in refractive index of the environment of the nanorod, in turn indeed creating a peak shift of the plasmon peaks. However, a change in refractive index of the environment would induce a blue shift of both the longitudinal as well as transverse peak position, contrary to what was observed in Figures 4.6a) and 4.6b). Hence, since we are observing peak shifts of the longitudinal and transverse peaks in different directions, this speaks for peak shift induced by reshaping and goes against the explanation of peak shift induced by desorption of molecules. A second argument discussing estimated surface density of CTAB molecules bound the gold nanorod in relation to layers of CTAB formed on the rod, can be found in Appendix B.

4.3.2 Single triangular power ramp

A single triangular ramp is employed that varies the trapping laser power from a considerably low value up to a high value, chosen to be as close to the critical power as possible. The results from one of these experiments are seen in Figure 4.7. As the laser power is ramped the longitudinal peak position (4.7a) is blue-shifted to a maximum of 13.5 nm with respect to its starting value. A part of this peak shift is attributed to lowering of the refractive index of the surrounding medium due to the increased temperature of the particle, from the increased laser power. When the laser power is again decreased to its initial value, the peak does not shift back to the original position, but is remaining at a considerably bluer wavelength. The long-term, irreversible peak shift turns out to be around 8 nm. This long-term shift is attributed to reshaping of the particle occurring during the laser ramp.

The transverse peak is sadly not pronounced for the spectral measurements of this particle. Therefore, the fitted transverse peak of each spectrum has to be disregarded owing to large confidence intervals, which is why this graph is omitted in this case. Nevertheless, the longitudinal peak position data seen in Figure 4.7a) is a strong indication of the reshaping taking place because of the significant irreversible peak shift during the course of the measurement.

Furthermore, both the rotation frequency (4.7b) and calculated temperature (4.7c) are seen to increase. The increases are linear in the beginning and as the laser power is becoming high the slopes of the rotation frequency and the temperature are deviating from their linearity. This is an effect that has been observed in previous experiments at Chalmers, and presented in [36]. Therein, the rotation frequency was found to deviate from the theoretically predicted frequency, which is hypothesised to be attributed to reshaping of the rod or even nanobubble formation. In these results, we can very clearly

link the deceasing slope of the rotation frequency with the severe irreversible peak shift and thus reshaping that is occurring as the laser power is ramped to a high power. Whether the peak shift corresponding to the highest laser power is solely an effect from heating of the surrounding water or if there is some envelope of vapor forming around the particle is discussed below as the results are analyzed further.

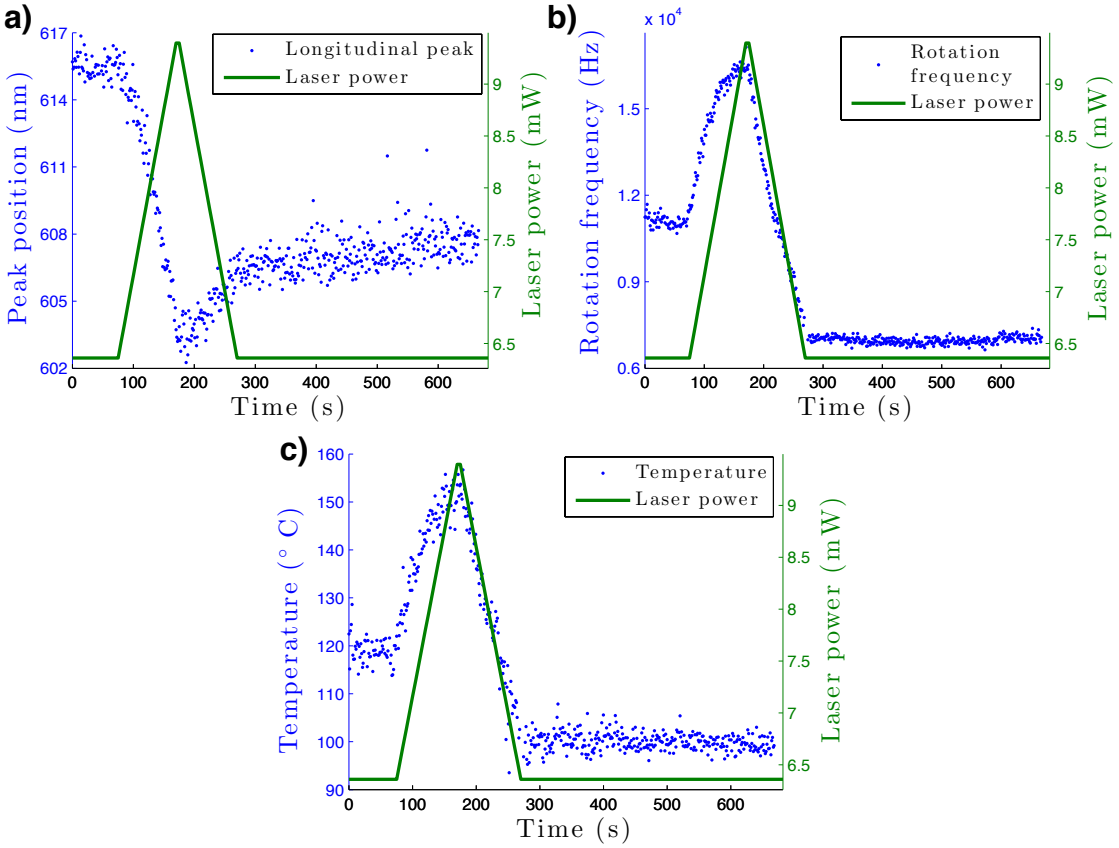

Figure 4.7: A trapped and rotating nanorod during a single high triangular laser power ramp. For the particle longitudinal LSPR peak (a), rotation frequency (b) and surrounding medium temperature (c) are extracted from the DF scattering spectrum and autocorrelation signal. A dip in the LSPR peak position at the time of the laser ramp is observed and followed by a large irreversible spectral shift. The rotation frequency and temperature both reach a crest as the power is ramped, and are thereafter stabilized on values lower than at the start of the experiment.

4.3.3 Linearly increasing triangular power raps

The last and most complex laser power ramping scheme employed is the linearly increasing triangular ramps. In Figure 4.8 the four quantities, longitudinal (4.8a) and transverse (4.8b) LSPR peak position, rotation frequency (4.8c) and calculated temperature (4.8d) are presented for a particle. The first impression of these graphs is an excellent correspondence between the peaks in the power ramp with peaks in all the

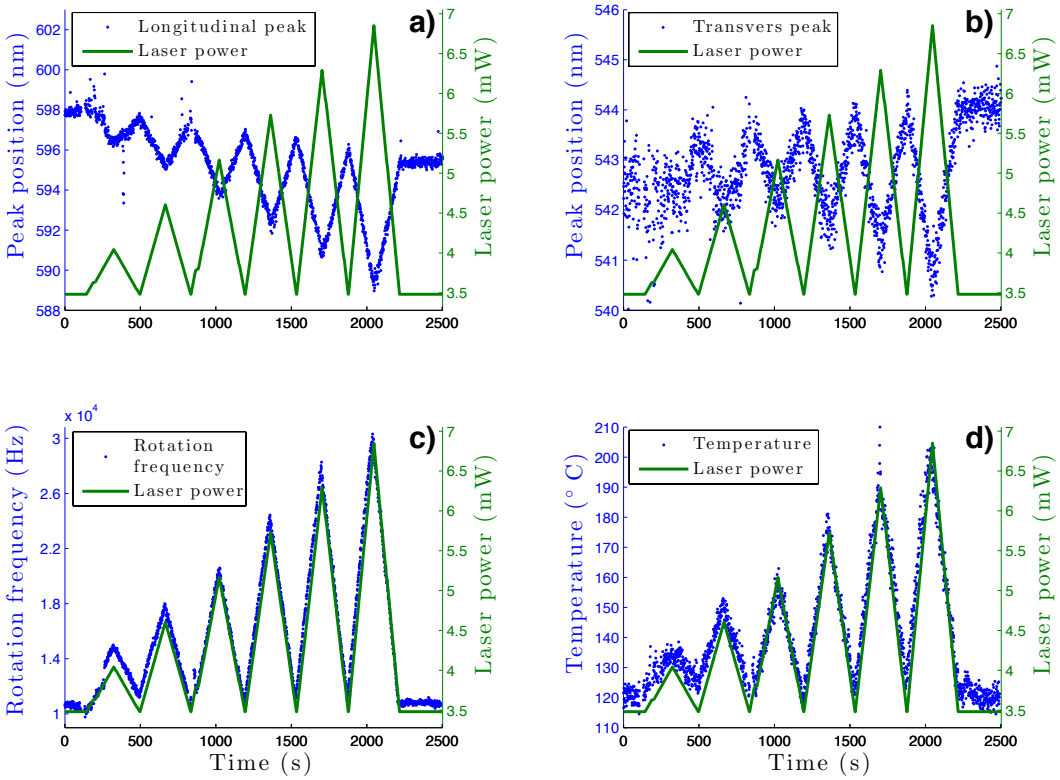

Figure 4.8: Data obtained during continuous measurements on a trapped and rotating nanorod when applying several triangular power ramps with linearly increasing maximum power. Displayed are the longitudinal (a) and transverse (b) LSPR peak shifts during the experiment, together with rotation frequency (c) and estimated temperature (d). As with the previous experiments the long-term spectral trend is indicating continuous reshaping of the trapped rod, with blue- and red-shift respectively of the longitudinal and transverse peak. During the laser ramps both peak exhibit blue shift, again indicating lowering of the RI due to photothermal effects. The rotation frequency and estimated temperature also follow the ramps to a high degree.

measured values. Considering the longitudinal LSPR, just as before, the long-term trend attests to a reshaping that is continuous during the experiments. In the same fashion the transverse peak is over the course of the experiment red-shifting, strengthening the explanation of a reshaping rod. Moreover, as the laser power is ramped both the LSPR peaks are blue-shifting in correspondence to the triangular ramp. This short-term shifts are, just as for the single triangular ramp, attributed to reduced RI from increasing ambient temperature.

At first glance, the results presented in Figure 4.8 might seem not to provide more information about the system than is already provided in the single ramp result above. Nevertheless, they are of interest due to the impressive correspondence between the power ramps and the trends in the measured quantities. Furthermore, the frequency in this case does not deviate from the linear behaviour it is exhibiting. Hence, there is reason to believe that the physical processes governing this experiment are not entirely

the same as the ones responsible for the results displayed in Figure 4.7. Below these two cases will be analyzed further, compared and discussed.

4.3.4 Decouple reshaping and heating effects

From Figures 4.7a) and 4.8a) irreversible peak shifts of the longitudinal plasmon peak of two trapped rotating particles are observed. We now make the assumption that during the triangular laser power ramps the same continuous reshaping of the particle is taking place as in the constant laser power case presented in Section 4.3.1, producing linear plasmonic peak shift resulting from reshaping. Then the two effects; namely, continuous reshaping and the heating induced peak shift (which stems from reduced refractive index of the surrounding as laser heating increases) can then be decoupled and separated. In Figure 4.9 this decoupling of reshaping and photothermal induced peak shift has been done for the two triangular power ramp experiments. In 4.9a) and 4.9c) the longitudinal peak position is displayed as it was measured in the experiments presented in Figures 4.7a) and 4.8a) respectively (blue data points). Together with this is the linear estimate

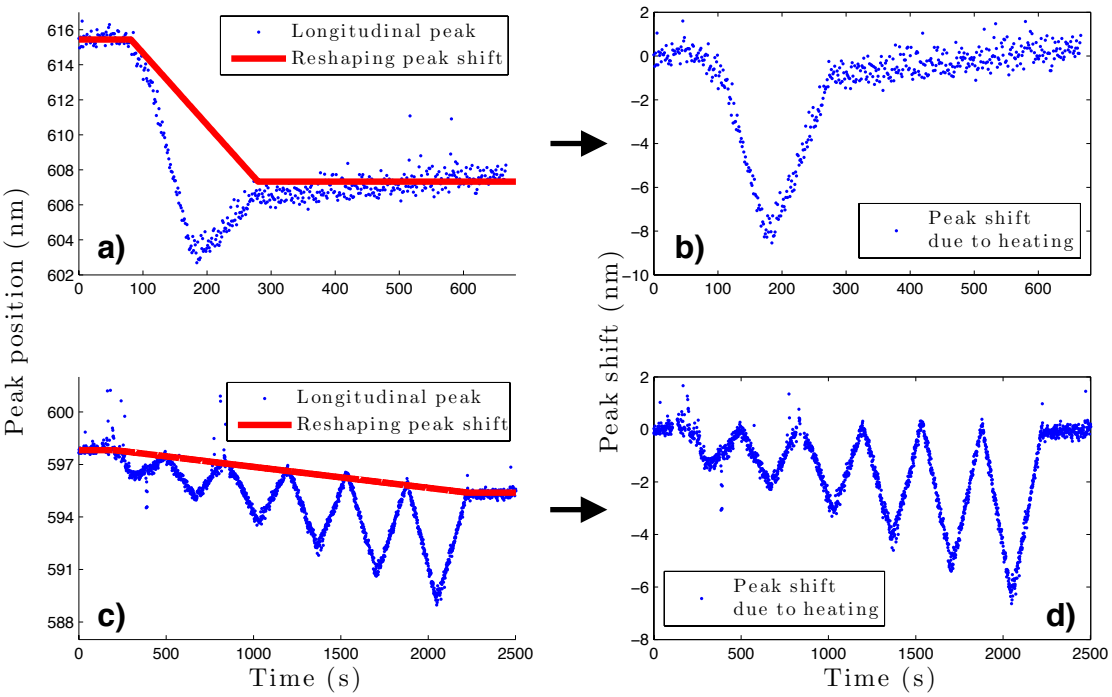

Figure 4.9: Illustration showing how the reshaping and temperature LSPR peak shifts can be decoupled in the triangular power ramp experiments. Figures a) and c) show longitudinal peak shift as displayed in Figures 4.7a) and 4.8a) (blue data points) together with an estimate of the reshaping induced peak shift (red line). Once the peak shift from reshaping is approximated this can be subtracted from the total peak shift, thus, obtaining a measurement of the peak shift induced only by the change in refractive index due to increased laser heating. This is done and displayed for a single high power triangle ramp (b) as well as the linearly increasing triangular ramps (d).

of the peak shift induced by shape change of the particle (red line). By subtracting the value of red curve from the blue data points the graphs of Figure 4.9b) and 4.9d) are reached. These two figures illustrate the peak shift solely attributed to the heating of the environment by the particle, altering its refractive index.

For the estimate of the reshaping induced peak shifts in these two cases it is assumed for ease of calculation that the particle is only reshaped during the laser ramp and not at constant low power. The peak position resulting from reshaping is; hence, unchanged before and after the ramps in Figures 4.9a) and 4.9c). This seems to contradict the results attained for constant laser power. However, when analyzing the slopes of the red curve during the ramp it is apparent that the change is occurring at a time scale much faster than the reshaping at constant power (4.9a) or the constant laser power interval is so short as to not produce any significant reshaping (4.9c).

After separating the two effects, it is possible to more in depth analyze the two processes affecting the nanorod. Changes to the aspect ratio (reshaping) and the refractive index of the surrounding (heating in this case) are common reasons for LSPR peak shifts. For a rod that is small, and retardation effects in the plasmon oscillation can be neglected, it is safe to assume that the LSPR peak position is depending linearly upon changes in the aspect ratio and the surrounding refractive index. Therefore, from either calculations made in the quasi-static approximation for a prolate spheroid or more accurate FDTD simulations for a hemispherically capped cylinder, the LSPR peak position sensitivity to changes in these two properties can be estimated. To obtain sensitivity of the LSPR peak position to these two property changes FDTD simulations were made by Ph.D. student Nils Odebo Länk. It was found that the longitudinal LSPR peak position for a nanorod, with the same dimensions as the one we study in this thesis, displays a peak shift of 122 nm/AR upon changing the aspect ratio with one unit as well as 243 nm/RIU upon changing the refractive index with one unit.

4.3.4.1 Reshaping

The reshaping can from the above sensitivity be analyzed since from the continuous measurements the rate at which the plasmon peaks are changing is a measured quantity. By dividing the longitudinal peak shift change rate attributed to reshaping (red curves in 4.9a and 4.9c) with the sensitivity of the plasmon peak position we obtain the aspect ratio change rate (dAR). If the volume is again assumed to be conserved during the reshaping and the initial aspect ratio ($\frac{L}{D}$) is known, the following equation system can be found and used to extract the new particle dimensions.

$$\begin{cases} \frac{L}{D} - \mathrm{dAR} = \frac{L'}{D'} \\ V = \frac{\pi}{12} D^2 (3L - D) = \frac{\pi}{12} D'^2 (3L - D') \end{cases} \Rightarrow \begin{cases} D' = \left(\frac{3D^2 L - D^3}{3\frac{L}{D} - 3\mathrm{dAR} - 1} \right)^{\frac{1}{3}} \\ L' = \frac{3D^2 L - D^3 + D'^2}{D'^2} \end{cases}, \tag{4.3}$$

where, as before, $D = 65\,\mathrm{nm}$ is the width of the nanorod and $L = 108\,\mathrm{nm}$ is the total length of it, determined from SEM-images. D' and L' are the width and length of the reshaped nanorod. From these formulas, the size of the particle at the end of the three

experiments as well as the rate of reshaping during the constant power illumination and laser ramps are calculated. These results are presented in Table 4.1. The most noticeable aspect of this table is the fact that the single ramp reshaping rate is one order of magnitude larger than the other two. This should be seen as a further indication that different processes govern the reshaping in this case, compared with the other two experiments. Both the constant power and the increasing ramps display considerably smaller and slower changes in the particle dimensions.

Table 4.1: Estimated length and width of reshaped particles after the three experiments, as well as the rate at which the reshaping of the length and width of the rod is taking place. The single ramp reshaping rate being one order of magnitude larger than the other two is noteworthy, and is a further indication that different process govern this reshaping, compared with the other two experiments. Both the constant power and the increasing ramps display small and slower change in the particle dimensions.

Experiment	End L (nm)	Rate L (nm/h)	End D (nm)	Rate D (nm/h)
Constant power	107.33	-1.2	65.27	0.5
Single ramp	105.4	-42.0	66.1	18.4
Increasing ramps	107.2	-1.5	65.3	0.6

4.3.4.2 Refractive index

In the same fashion, we can estimate the change in refractive index due to the photothermal heating of the immediate environment to the particle. As we divide the longitudinal peak position change rate because of heating (as presented in 4.9b and 4.9d) with the plasmon peak sensitivity to RI changes, the refractive index change rate dRI during the experiment is obtained. As it is well studied and known how refractive index of water changes due to temperature changes, the data obtained for dRI can be plotted against the temperature extracted from the decay time of the autocorrelation signal. In Figure 4.10 this is done for the triangular ramp experiments (blue data points) and compared with an expression for refractive index depending on temperature (red curve) derived in reference [76]. Since the calculated values for dRI only give the change in refractive index, these data points are offset in the y-direction to match the formula data in this direction. The slope of the data is of course unchanged by this operation. For the linearly increasing power ramps (4.10b) the slope of the data is corresponding well with the tabulated values for temperature dependent refractive index of water. This provides a good indication that the LSPR peak shift in this case is indeed due to changes in refractive index resulting from increased temperature of the water environment. The same graph for the single, high power, triangular power ramp (4.10a) on the other hand demonstrates a good correspondence between the slope of the tabulated temperature dependent RI value and the now measured data points at certain parts of the measurement (indicated by the red dashed lines). Yet, for one interval of the measurement (indicated by the dashed blue line), corresponding to the high laser power region, the slope of the herein

extracted RI data deviate from the one expected from water. This is an additional piece of evidence suggesting a phase shift of the material in the immediate environment to the particle since the temperature dependent RI is producing a slope different from that of water.

One should mention the fact that the estimated temperature of the environment to the nanorod where we argue that bubble formation is occurring is actually lower that the temperature of the particle in the linearly increasing ramp experiment. Why is bubble formation not occurring in this higher temperature case then? The explanation probably lies in the temperature estimation procedure, and the heterogeneity of the particles studied. When estimating the temperature the average dimensions extracted from SEM imaging are used. However, if a particle smaller or larger than average is trapped the temperature estimation will be slightly off. The real temperature of the nanorod in Figure 4.7 might very well be higher than the Figure 4.8 case, but the size difference between them will create an error in our temperature estimation. Hence, it should again be stressed that this route to obtain the temperature should be seen not as a measurement, but rather an estimation of the quantity.

RI effects on the spectroscopic properties of the nanorod can be calculated by changing ε_m in either the quasi-static approximation or in FDTD simulations. Though this is possible, one has to remember that these models only take in a static dielectric constant,

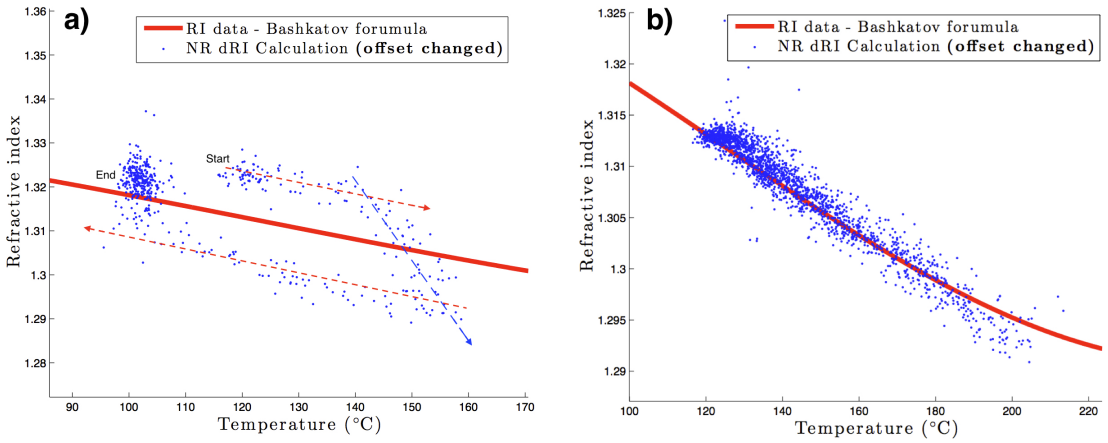

Figure 4.10: Values for refractive index plotted against temperature. The red lines correspond to an experimentally obtained expression for the refractive index of water derived in reference [76]. Blue data points are offset-corrected estimations of the change in refractive index of the surrounding from the heating attributed LSPR peak shift, plotted against the calculated surrounding temperature. These plots are generated for the single high power triangular laser ramp (a) and the linearly increasing laser power ramp (b). For b), the slope of the estimated heating induced refractive index change corresponds very well to the experimentally measured values for the refractive index of water at varying temperature. For a) most of the measured data points (marked with red dashed lines to guide the eye), the slope corresponds well to the red curve. However, there is a passage (dashed blue line) that exhibits a different slope. This indicates that the RI properties of the medium here are different, possibly owing to a phase change of the environment. The arrows are indicating the temporal direction of the measurement.

which describes the entire environment outside the particle. The real case is more complex than this simplified model since a gradient in temperature, and therefore also in refractive index, is arising from the particle. This will create a system more difficult to model with simply electrodynamic simulations. FDTD simulations in combination with heat conduction simulations performed in COMSOL could possibly resolve this question, and such are planned for the continuation of this study.

Nanoscopic vapor bubbles formed around gold nanospheres immobilized on glass substrate has been studied by Fang et al. in reference [37]. Herein, they observe shifts of the LSPR peak position of a sphere, with volume comparable to the rods used in this investigation, of around 16 nm. The magnitude of the shift is certainly dependent upon the shape of the particle. However, the peak shift at the crest of the laser ramp in Figure 4.6 is estimated to be 13.5 nm, which is comparable to the shifts observed in [37]. Yet another indication that what we are observing here is formation of a vapor layer around a trapped and rotating particle.

4.4 Possible changes to experimental procedure

As experiments have been performed and results have been collected and analyzed, it is almost unavoidable to evaluate the experimental procedure and in hindsight realize that some aspects of the collection possibly should have been done differently. Below, the two main considerations are discussed.

4.4.1 Centroid tracking

Another common technique to determine the spectral peak position is to fit a high order polynomial curve to the recorded scattering spectrum and calculate the centroid of the spectrum. The centroid will shift as the LSPR shifts and this can be tracked. Centroid tracking is frequently used in biosensing systems based on LSPR spectrosopy and is well-described in reference [77]. The method is considered to track the spectral changes of a particle with better accuracy and lower noise than the Lorentzian fitting routine employed in this thesis. Therefore, one might argue that it would have been advantageous to use this routine in the experiments performed in this work. However, since this method only calculates a single centroid for the entire curve it does not provide the possibility of separately tracking the shifts of the longitudinal and transverse peak positions when these two are overlapping as significantly as in the above results. In this case, the compromise was made to enable separate tracking through bi-Lorentzian fitting instead of centroid tracking. Also, since the shifts observed are on the order of nanometers and the noise is at least one order of magnitude lower, the trade-off seemed reasonable.

4.4.2 Revised laser power ramps

The triangular laser power ramps did prove to be useful to interrogate the trapped and rotating particle. Several interesting underlying processes were observed and allowed to be separated and analyzed in detail. Nevertheless, the ramps could have been even more useful if they were engineered with even more consideration. If one would integrate the graph generated by the laser power ramps one would obtain an estimate of the total energy subjected to the particle during the experiment. Then, the laser power during the different experiments (constant power, single ramp, and linearly increasing ramps) could be constructed to subject the particle to equal amounts of energy flux. One could argue that some of the differences observed between the experiments possibly come from the fact that the total energy subjected to the different particles is not equal. Through further engineering of the laser ramps, this can be controlled and eliminated as a free variable.

Moreover, it could be of interest to study other types of laser power profiles. For example, step functions or pulses could possibly yield information about the speed at which morphological changes are taking place in the particle and even provide an understanding on how the reshaping rate is affected by laser power.

4.5 Preliminary results for continued investigations

During the laboratory work some experiments that were not exactly part of the main project were performed. For example, when some unexpected effect is found, a small detour can be taken to try to resolve an issue or study the effect a bit further. Experimental work is unpredictable, and this can be seen as a natural part of it in order to reach novel and interesting findings. Below follows account of two such unexpected results that were found from experiments conducted on the same setup, but not exactly related to the main topic of the thesis.

4.5.1 Rapid reshaping of long rods

As mentioned in the introduction, continuous reshaping of nanorods immobilized on a substrate during illumination with continuous wave laser has been studied previously. Nevertheless, during a complimentary experiment on such a system some unexpected results were obtained. Nanorods with a longitudinal resonance that is on the red wavelength side of the trapping laser were immobilized on the glass substrate. A single particle was then illuminated with the trapping laser light at a power of 3.9 mW. As seen in Figure 4.11 the spectral peak position of one of these longer particles is during some time considerably stable and shifts only a few nanometers. Then, around 20 seconds into the experiment the nanorod goes through a morphological change that induces a rapid spectral shift of almost 150 nm within less than three seconds. Similar results are reproduced for a number of particles and for laser powers all the way down to 2 mW. The time until the large rapid peak shift occurs was found to vary substantially from a

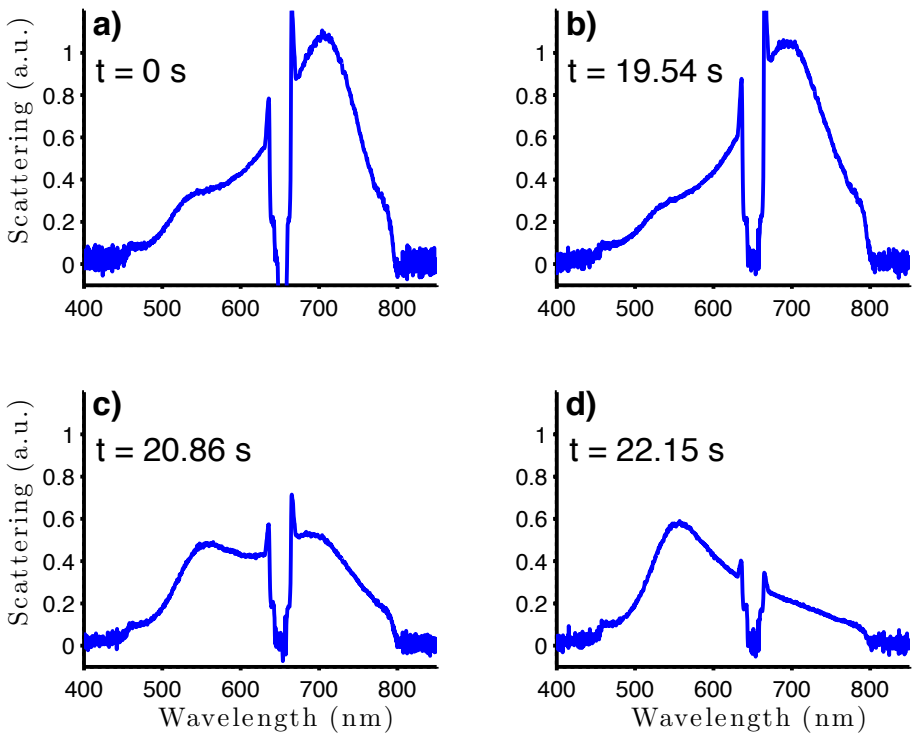

Figure 4.11: Four scattering spectra taken of a long nanorod immobilized on the substrate. At time $t = 0\,\mathrm{s}$ laser illumination is turned on at the power of 3.9 mW. During the following 19.5 seconds there is a continuous slight blue-shift of the longitudinal LSPR peak. Thereafter, at $t = 20.86\,\mathrm{s}$ something initializes a process where rapid peak shift of about 150 nm is accompanied with a decrease in the integrated scattered intensity.

few seconds to several minutes, and no apparent relation between the power and time until the rapid change was found.

This is a fascinating preliminary result that alludes to interesting underlying effects that should be studied further. One hypothesis regarding the reason for the effect is that the nanoparticle split into several pieces, which would explain the appearing decrease in scattered intensity. This could possibly occur due to a phase shift in the plasmon oscillation. Another theory is that something is inducing a vapor bubble to form, wherein the long rod is rapidly reshaped into a nanosphere. To investigate the process experiments are planned that involve SEM imaging of specific particles before and after the laser illumination experiments.

4.5.2 Laser induced particle release

An effect where particles, which are immobilized on a glass surface, can be made to release from its static state and become free in solution through the use of laser illumination was first observed during the experiments conducted above. Particles can be immobilized on the top surface, so that they remain trapped when they are released.

Furthermore, the sample geometry can be inverted and the particles are immobilized on that bottom side of the experiment chamber, and upon laser illumination they are released and shot upwards by radiation pressure out into the water environment. The effect presumably depends on the surface properties of the substrate onto which the particles are immobilized. In Figure 4.12 an image sequence from a video recording of such a particle being released and pushed into the water environment. These observations do not fall within the subject of this thesis, which is why it is not expanded on above. However, it is an interesting effect, which could be thoroughly studied further. Several interesting applications of this property could be imagined, for example in applications where a high degree of control over the density of particles in solution or the homogeneity is necessary. Furthermore, the range of possible biofunctionalizations performed on particles can potentially be widened by immobilizing particles on a substrate, perform the functionalization and then release it back into solution. This is due to the fact that many such functionalization processes involve the use of salts or other agents that will alter the charge balance of a colloidal nanoparticle solution and; hence, the nanoparticles stand a high risk of aggregating [78]. This risk would be eliminated if the particles were instead immobilized during the functionalization step.

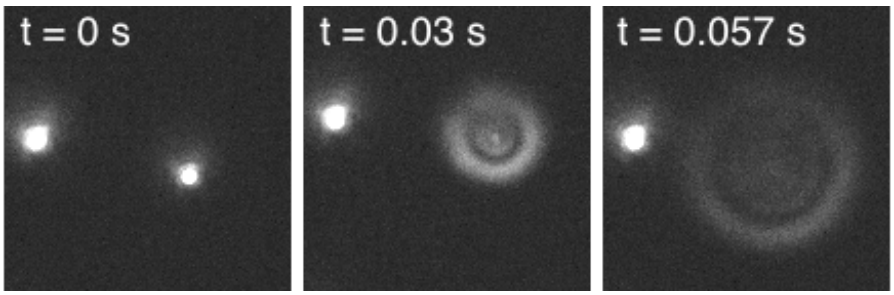

Figure 4.12: High-speed image sequence taken during a light induced particle release from the bottom surface of a sample cell. At time $t = 0$ the laser illumination is started, and in the following two frames the particle is seen to be released and pushed away from the substrate and from focus by the radiation pressure of the laser light. It is thereafter free in solution and can be trapped and manipulated as previously described.

5

Conclusion and outlook

The results have now been presented and thoroughly discussed. Essentially what is now remaining is to put the findings of this study into a broader context and to reach some conclusions on what the results will bring to the overall knowledge in the field. Additionally, some further studies that would be rewarding to conduct together with possible routs towards applications are discussed as concluding remarks in this master's thesis.

5.1 Summary and conclusion

In the work presented above the construction of a circularly polarized optical tweezers setup was realized. In this setup, particles were trapped against a glass substrate and were made to rotate at frequencies of several thousands of hertz. Instrumentation enabling detection of rotational dynamics as well as single particle dark field scattering spectra was included in the experimental setup. The quality of the trap was ascertained via measurements of the trapping stiffness. These measurements yielded characteristics comparable to ones presented in previous trapping studies.

Hereafter, the dependence of the core diameter of the collection fiber for scattered laser light was analyzed with respect to the recorded autocorrelation signal. Through results collected in this sub-project and following discussion it was found that information regarding translational Brownian motion is included in the autocorrelation signal collected using a thinner fiber. To finish up the discussion on this topic, a new model equation for fitting the correlogram was proposed, and its validity was tested. The ability to detect translational as well as rotational Brownian motion of trapped nanoparticles using autocorrelation has been reported previously in the literature [23, 25]. However, it has never been studied in detail for rotating particles in optical traps. Brownian motion of trapped rods is indeed interesting, and the analysis performed here is merely scratching the surface of this complex process. Nevertheless, this technique for studying the system holds great promise and should be utilized to perform deeper studies of Brownian motion of gold nanorods in optical tweezers.

The main results of this thesis relate to the parallel and continuous measurements of spectroscopic and rotational properties of trapped nanorods. The rods are analyzed by applying three different laser power ramps to deduce the photothermal effects acting on said rods. Constant laser power, a single high power triangular ramp and consecutive triangular ramps with linearly increasing maximum were applied, and the spectroscopic

and rotational response to these were analyzed. It was found that rods continuously reshape during trapping at constant laser power and that this reshaping is happening on the same timescale as previously measured reshaping of nanorods due to thermal heating. Also during the triangular power ramp experiments continuous reshaping is observed. Moreover, another process is introduced by the ramp that leads to a detectable spectral shift of the LSPR peaks. This is attributed to change in refractive index of the surrounding to the particle from changed temperature of the particle as the laser power is changing. For the linearly increasing power ramps the measured quantities are following the linear shape of the laser ramps to a high degree. However, in the high power laser regime close to the critical power, there is some deviation from the linearity as power is maximized. This is attributed to strong reshaping and vapor bubble formation around the particle. By analyzing the spectral shift of the longitudinal LSPR, the reshaping and refractive index induced shifts could be decoupled. This results in calculation of the reshaping rates during the different experiments and also in an estimation of the change in refractive index responsible for the measured peak shift. Several arguments are put forth to demonstrate that the high power ramp leads to vapor bubble formation around the trapped particle.

In order for the claims presented in this thesis to be further reinforced, an additional method for measuring the temperature of the environment around the particle is needed. This property has been measured in a range of different publications [46, 79, 80] and in the beginning of 2016 a paper was published that even claimed to be able to measure the temperature distribution around the particle [81]. It is possible that methods such as these ones are useful in determining the true surface temperature of the trapped rotating nanorod.

The purpose of this project was two-parted. The first goal, to construct a functional optical tweezers setup with the possibility to conduct spectroscopic investigations, was certainly reached. The second goal included to study spectroscopic and rotational properties of the particles and study the photo-induced effects of the rotary motor. Several interesting photothermal effects (e.g. reshaping, refractive index change and vapor bubble formation) were observed and illustrated through the measurements. Therefore, it is deemed that also the second goal of the thesis work was reached. To the author's best knowledge there has to date not been any spectroscopic studies conducted on trapped gold nanorods to deduce the photothermal effects, which matches the ones performed here, in terms of temporal or spatial resolution or complexity. The separation of irreversible peak shift attributed to reshaping and reversible peak shift caused by temperature change together with the rotational dynamics measurements are providing clear insights into the process governing the nanorod during trapping and rotation.

5.2 Outlook and future applications

The fundamental findings presented in this thesis are indeed interesting and novel in the plasmonic and optical tweezing community. Hence, the results should hopefully be published in a peer reviewed scientific journal in the near future. Some complementary

experiments need to be performed to substantiate the findings and clear out some of the remaining ambiguities. This should also include more in-depth investigations of the fascinating preliminary results of rapid reshaping and laser induced particle release as discussed above.

The platform for trapping and rotating particles with the possibility to perform both spectroscopic investigations and correlation spectroscopy holds hope to be useful in several different possible applications. Some of these will potentially be researched during a continuation of this project. In the following paragraphs, a few of the most promising directions are considered.

Many successful applications based on plasmonics can be found as sensors [7]. It has previously been demonstrated that also the rotation frequency of a trapped rotating nanorod can be used as a sensor for a range of different interactions in solutions; e.g. viscosity of the solution, flow rate within a fluidic channel, and also binding of molecules to the particle surface [36]. It would be of high interest to further investigate in what sensing schemes the rotating particle is most useful. For example, gold nanorods could be functionalized with specific molecular linkers to detect a range of different molecular binding processes. The plasmonic sensing region is governed by the decay of the evanescent fields of the plasmon oscillation within the surrounding medium that is on the scale of a few nanometers. The rotation frequency is hypothesised to complement the plasmonic sensing by expanding the sensitive region in for instance molecular binding sensing. Another possible experiment to explore the benefits of using a rotating nanorod as a sensor compared to an immobilized nanoparticle could be performed by measurements of, for example, molecular binding for these side by side and simultaneously.

In the field of photonic force microscopy (PFM) the possibility to use an optically trapped particle as a probe in a similar manner as the sharp-tipped cantilever is used in an AFM environment is explored. A trapped particle would, while probing a structure, subject it to forces that are several orders of magnitude smaller than what an AFM tip does. The trapped particle might thus be suitable to be used to image softer and more fragile structures. The possibility to use trapped particles to reach imaging below the diffraction limit was suggested already in 1992 [82]. In a recent Nature publication this is in fact realized in a very nice way by using trapped particles of both polystyrene and gold [83]. By using gold as the material of the probing particle not only will the particle be sensitive to the force interactions of the structure being imaged but also to refractive index adding another dimension the probe function. Potentially the rotation of the particle could provide additional information for example about friction and roughness of a surface. In this configuration a PFM using a rotating particle could potentially be used in a way comparable to that of the AFM based lateral force microscope, but still maintaining the gentle characteristic of the PFM.

To get reliable measurements in the two applications suggested above one would like the particle to be as stable and inert as possible. Consequently, it might seem strange to work with a probe as unstable as the one demonstrated in this work. It should be mentioned in response to this; the stability of the particle is related to the heating of it, which is dependent on the spectral separation between the LSPR peak position and the

laser light used for trapping. In this study, we work with a 660 nm laser that is close to the LSPR peak of the particle in order to get larger, more easily detectable, photothermal effects. If the system were to be used for the type of measurements proposed above it is necessary to use a laser of longer wavelength, so as not to photothermally affect the particle too much.

A common application of gold nanoparticles that hold high hopes is using them as carriers of drugs for example in *in vivo* treatments, due to low cytotoxicity, ease to functionalize and advantageous plasmonic properties [9, 84]. Using a CW optical tweezers setup, gold particles have been injected into living cells in an *in vitro* environment [85]. This could potentially be an interesting way to reach single cell targeted drug delivery and is suggested to be used in a nanotheranostic platform [86]. The rotation of nanorods presented in this thesis might aid the injection into cells by acting as a nanoscopic drill. Moreover, optical injection of drug carrying particles might be combined with the above discussed laser induced release of nanoparticles to reach a dynamic platform for injection of functionalized gold nanoparticles into living cells and assessment of treatment efficiency. A proposed setup for this that also includes a plasmonic tweezers substrate for momentarily immobilization of a cell during injection is presented in Figure 5.1.

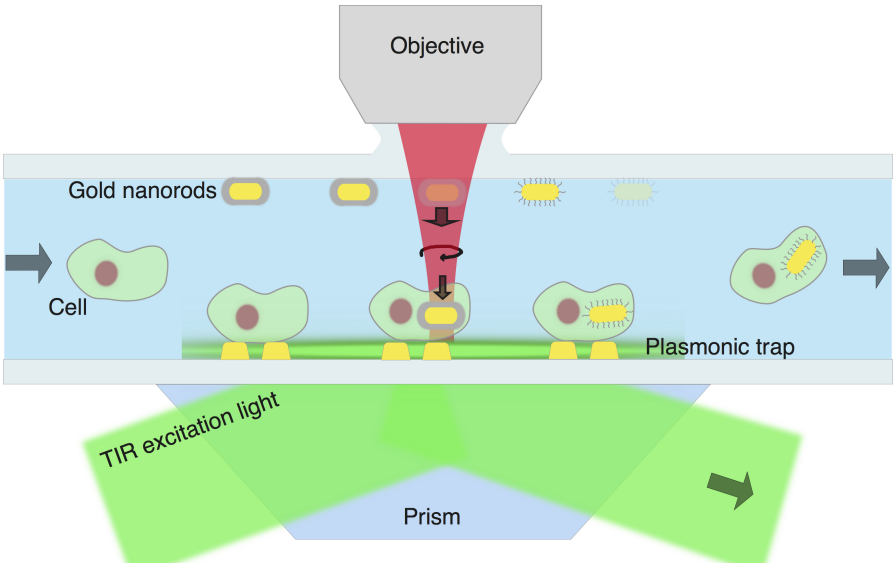

Figure 5.1: A schematic illustration of a proposed measurement and drug injection system. In an upright microscope configuration functionalized or drug-carrying gold nanorods are immobilized on the top surface in a microfluidic channel and can be released at will with a tightly focused laser beam. After being released, a particle can be rotated as it is approaching a cell, which has been trapped at the bottom surface of the channel. The cell could be immobilized momentarily by nanoscopic plasmonic tweezers, which are excited in a total internal reflection configuration. As the nanoparticle reaches the cell, it can be optically injected through the cell wall. The cell can be studied for as long as required and thereafter be released.

Bibliography

[1] C. F. Bohren, D. R. Huffman, Absorption and scattering of light by small particles, John Wiley & Sons, 2008.

[2] A. M. Fox, Optical properties of solids, Vol. 3, Oxford university press, 2001.

[3] S. A. Maier, Plasmonics: fundamentals and applications, Springer Science & Business Media, 2007.

[4] H. Chen, L. Shao, Q. Li, J. Wang, Gold nanorods and their plasmonic properties, Chemical Society Reviews 42 (7) (2013) 2679–2724.

[5] M. Faraday, Xlvii. experimental relations of gold (and other metals) to light — the bakerian lecture.

[6] G. Mie, Beiträge zur optik trüber medien, speziell kolloidaler metallösungen, Annalen der Physik 330 (3) (1908) 377–445.

[7] K. A. Willets, R. P. Van Duyne, Localized surface plasmon resonance spectroscopy and sensing, Annu. Rev. Phys. Chem. 58 (2007) 267–297.

[8] X. Huang, P. K. Jain, I. H. El-Sayed, M. A. El-Sayed, Plasmonic photothermal therapy (pptt) using gold nanoparticles, Lasers in Medical Science 23 (3) (2008) 217–228.

[9] P. Ghosh, G. Han, M. De, C. K. Kim, V. M. Rotello, Gold nanoparticles in delivery applications, Advanced Drug Delivery Reviews 60 (11) (2008) 1307–1315.

[10] P. Zijlstra, J. W. Chon, M. Gu, Five-dimensional optical recording mediated by surface plasmons in gold nanorods, Nature 459 (7245) (2009) 410–413.

[11] K. Catchpole, A. Polman, Plasmonic solar cells, Optics Express 16 (26) (2008) 21793–21800.

[12] D. K. Cheng, Field and wave electromagnetics, Vol. 2, Addison-Wesley New York, 1989.

[13] A. Ashkin, Acceleration and trapping of particles by radiation pressure, Physical Review Letters 24 (4) (1970) 156.

[14] A. Ashkin, J. Dziedzic, J. Bjorkholm, S. Chu, Observation of a single-beam gradient force optical trap for dielectric particles, Optics Letters 11 (5) (1986) 288–290.

[15] M. Woerdemann, Structured Light Fields: Applications in Optical Trapping, Manipulation, and Organisation, Springer Science & Business Media, 2012.

[16] P. C. Ashok, K. Dholakia, Optical trapping for analytical biotechnology, Current Opinion in Biotechnology 23 (1) (2012) 16–21.

[17] F. M. Fazal, S. M. Block, Optical tweezers study life under tension, Nature Photonics 5 (6) (2011) 318–321.

[18] W. D. Phillips, Nobel lecture: Laser cooling and trapping of neutral atoms, Reviews of Modern Physics 70 (3) (1998) 721.

[19] P. Galajda, P. Ormos, Complex micromachines produced and driven by light, Applied Physics Letters 78 (2) (2001) 249–251.

[20] A. Ashkin, Applications of laser radiation pressure, Science 210 (4474) (1980) 1081–1088.

[21] K. Svoboda, S. M. Block, Optical trapping of metallic rayleigh particles, Optics Letters 19 (13) (1994) 930–932.

[22] P. M. Hansen, V. K. Bhatia, N. Harrit, L. Oddershede, Expanding the optical trapping range of gold nanoparticles, Nano Letters 5 (10) (2005) 1937–1942.

[23] M. Pelton, M. Liu, H. Y. Kim, G. Smith, P. Guyot-Sionnest, N. F. Scherer, Optical trapping and alignment of single gold nanorods by using plasmon resonances, Optics Letters 31 (13) (2006) 2075–2077.

[24] C. Selhuber-Unkel, I. Zins, O. Schubert, C. Sönnichsen, L. B. Oddershede, Quantitative optical trapping of single gold nanorods, Nano Letters 8 (9) (2008) 2998–3003.

[25] P. Ruijgrok, N. Verhart, P. Zijlstra, A. Tchebotareva, M. Orrit, Brownian fluctuations and heating of an optically aligned gold nanorod, Physical Review Letters 107 (3) (2011) 037401.

[26] A. Lehmuskero, P. Johansson, H. Rubinsztein-Dunlop, L. Tong, M. Käll, Laser trapping of colloidal metal nanoparticles, ACS nano 9 (4) (2015) 3453–3469.

[27] J. Prikulis, F. Svedberg, M. Käll, J. Enger, K. Ramser, M. Goksör, D. Hanstorp, Optical spectroscopy of single trapped metal nanoparticles in solution, Nano Letters 4 (1) (2004) 115–118.

[28] R. A. Beth, Mechanical detection and measurement of the angular momentum of light, Physical Review 50 (2) (1936) 115.

[29] M. Friese, T. Nieminen, N. Heckenberg, H. Rubinsztein-Dunlop, Optical alignment and spinning of laser-trapped microscopic particles, Nature 394 (6691) (1998) 348–350.

[30] P. Galajda, P. Ormos, Rotors produced and driven in laser tweezers with reversed direction of rotation, Applied Physics Letters 80 (24) (2002) 4653–4655.

[31] S. L. Neale, M. P. MacDonald, K. Dholakia, T. F. Krauss, All-optical control of microfluidic components using form birefringence, Nature Materials 4 (7) (2005) 530–533.

[32] Y. Arita, M. Mazilu, K. Dholakia, Laser-induced rotation and cooling of a trapped microgyroscope in vacuum, Nature Communications 4.

[33] L. Tong, V. D. Miljkovic, M. Käll, Alignment, rotation, and spinning of single plasmonic nanoparticles and nanowires using polarization dependent optical forces, Nano Letters 10 (1) (2009) 268–273.

[34] Y. E. Lee, K. H. Fung, D. Jin, N. X. Fang, Optical torque from enhanced scattering by multipolar plasmonic resonance, Nanophotonics 3 (6) (2014) 343–350.

[35] A. Lehmuskero, R. Ogier, T. Gschneidtner, P. Johansson, M. Käll, Ultrafast spinning of gold nanoparticles in water using circularly polarized light, Nano Letters 13 (7) (2013) 3129–3134.

[36] L. Shao, Z.-J. Yang, D. Andrén, P. Johansson, M. Käll, Gold nanorod rotary motors driven by resonant light scattering, ACS Nano 9 (12) (2015) 12542–12551.

[37] Z. Fang, Y.-R. Zhen, O. Neumann, A. Polman, F. J. García de Abajo, P. Nordlander, N. J. Halas, Evolution of light-induced vapor generation at a liquid-immersed metallic nanoparticle, Nano Letters 13 (4) (2013) 1736–1742.

[38] S. Iijima, T. Ichihashi, Structural instability of ultrafine particles of metals, Physical Review Letters 56 (6) (1986) 616.

[39] H. Petrova, J. P. Juste, I. Pastoriza-Santos, G. V. Hartland, L. M. Liz-Marzán, P. Mulvaney, On the temperature stability of gold nanorods: comparison between thermal and ultrafast laser-induced heating, Physical Chemistry Chemical Physics 8 (7) (2006) 814–821.

[40] C. Nordling, J. Österman, Physics handbook, Studentlitteratur, 1987.

[41] A. B. Taylor, A. M. Siddiquee, J. W. Chon, Below melting point photothermal reshaping of single gold nanorods driven by surface diffusion, ACS Nano 8 (12) (2014) 12071–12079.

[42] D. Harris-Birtill, M. Singh, Y. Zhou, M. E. Gallina, T. Cass, D. S. Elson, Gold nanorod reshaping using a continuous wave laser, in: CLEO: Applications and Technology, Optical Society of America, 2014, pp. JTh2A–95.

[43] W. Ni, H. Ba, A. A. Lutich, F. Jäckel, J. Feldmann, Enhancing single-nanoparticle surface-chemistry by plasmonic overheating in an optical trap, Nano Letters 12 (9) (2012) 4647–4650.

[44] H. Xu, E. J. Bjerneld, M. Käll, L. Börjesson, Spectroscopy of single hemoglobin molecules by surface enhanced raman scattering, Physical Review Letters 83 (21) (1999) 4357.

[45] K. Kneipp, Y. Wang, H. Kneipp, L. T. Perelman, I. Itzkan, R. R. Dasari, M. S. Feld, Single molecule detection using surface-enhanced raman scattering (sers), Physical Review Letters 78 (9) (1997) 1667.

[46] A. Andres-Arroyo, F. Wang, W. J. Toe, P. Reece, Intrinsic heating in optically trapped au nanoparticles measured by dark-field spectroscopy, Biomedical optics express 6 (9) (2015) 3646–3654.

[47] T. Jensen, L. Kelly, A. Lazarides, G. C. Schatz, Electrodynamics of noble metal nanoparticles and nanoparticle clusters, Journal of Cluster Science 10 (2) (1999) 295–317.

[48] E. J. Zeman, G. C. Schatz, An accurate electromagnetic theory study of surface enhancement factors for silver, gold, copper, lithium, sodium, aluminum, gallium, indium, zinc, and cadmium, Journal of Physical Chemistry 91 (3) (1987) 634–643.

[49] P. B. Johnson, R.-W. Christy, Optical constants of the noble metals, Physical review B 6 (12) (1972) 4370.

[50] E. Fällman, O. Axner, Design for fully steerable dual-trap optical tweezers, Applied Optics 36 (10) (1997) 2107–2113.

[51] S. Chu, Laser manipulation of atoms and particles, Science 253 (5022) (1991) 861–866.

[52] J. Arias-González, M. Nieto-Vesperinas, Optical forces on small particles: attractive and repulsive nature and plasmon-resonance conditions, JOSA A 20 (7) (2003) 1201–1209.

[53] L. Novotny, B. Hecht, Principles of nano-optics, Cambridge university press, 2012.

[54] A. Ranaweera, Investigations with optical tweezers: construction, identification, and control, Ph.D. thesis, University of California - Santa Barbara (2004).

[55] A. Ashkin, J. P. Gordon, Stability of radiation-pressure particle traps: an optical earnshaw theorem, Optics letters 8 (10) (1983) 511–513.

[56] R. R. Agayan, F. Gittes, R. Kopelman, C. F. Schmidt, Optical trapping near resonance absorption, Applied optics 41 (12) (2002) 2318–2327.

[57] J. Barton, D. Alexander, Fifth-order corrected electromagnetic field components for a fundamental gaussian beam, Journal of Applied Physics 66 (7) (1989) 2800–2802.

[58] K. C. Neuman, S. M. Block, Optical trapping, Review of scientific instruments 75 (9) (2004) 2787–2809.

[59] K. Berg-Sørensen, H. Flyvbjerg, Power spectrum analysis for optical tweezers, Review of Scientific Instruments 75 (3) (2004) 594–612.

[60] R. Fogel'son, E. Likhachev, Temperature dependence of viscosity, Technical Physics 46 (8) (2001) 1056–1059.

[61] D. Kong, W. Lin, Y. Pan, K. Zhang, Swimming motion of rod-shaped magnetotactic bacteria: the effects of shape and growing magnetic moment, Intracellular biomineralization in bacteria (2014) 41.

[62] J. R. Lakowicz, Principles of fluorescence spectroscopy, Springer Science & Business Media, 2013.

[63] S. P. Smith, S. R. Bhalotra, A. L. Brody, B. L. Brown, E. K. Boyda, M. Prentiss, Inexpensive optical tweezers for undergraduate laboratories, American Journal of Physics 67 (1) (1999) 26–35.

[64] A. Samadi, N. S. Reihani, Optimal beam diameter for optical tweezers, Optics Letters 35 (10) (2010) 1494–1496.

[65] J. Pawley, B. R. Masters, Handbook of biological confocal microscopy, Optical Engineering 35 (9) (1996) 2765–2766.

[66] M. Plewicki, Phase, amplitude, and polarization pulse shaping in order to influence molecular processes, Ph.D. thesis, Freie Universität Berlin (2007).

[67] C.-K. Chou, W.-L. Chen, P. T. Fwu, S.-J. Lin, H.-S. Lee, C.-Y. Dong, Polarization ellipticity compensation in polarization second-harmonic generation microscopy without specimen rotation, Journal of Biomedical Optics 13 (1) (2008) 014005–014005.

[68] G. Malykin, Use of the poincare sphere in polarization optics and classical and quantum mechanics. review, Radiophysics and quantum electronics 40 (3) (1997) 175–195.

[69] X. Ye, C. Zheng, J. Chen, Y. Gao, C. B. Murray, Using binary surfactant mixtures to simultaneously improve the dimensional tunability and monodispersity in the seeded growth of gold nanorods, Nano Letters 13 (2) (2013) 765–771.

[70] C.-K. Tsung, X. Kou, Q. Shi, J. Zhang, M. H. Yeung, J. Wang, G. D. Stucky, Selective shortening of single-crystalline gold nanorods by mild oxidation, Journal of the American Chemical Society 128 (16) (2006) 5352–5353.

[71] I. M. Tolić-Nørrelykke, K. Berg-Sørensen, H. Flyvbjerg, Matlab program for precision calibration of optical tweezers, Computer physics communications 159 (3) (2004) 225–240.

[72] D. A. Skoog, D. M. West, Principles of instrumental analysis, Vol. 158, Saunders College Philadelphia, 1980.

[73] A. J. Haes, R. P. Van Duyne, A unified view of propagating and localized surface plasmon resonance biosensors, Analytical and Bioanalytical Chemistry 379 (7-8) (2004) 920–930.

[74] A. D. McFarland, R. P. Van Duyne, Single silver nanoparticles as real-time optical sensors with zeptomole sensitivity, Nano Letters 3 (8) (2003) 1057–1062.

[75] P. Kidwelly (Ed.), Fluorescence of optical filter glass: characterization and measurement results, DGaO 116th Annual Meeting, Brno University of Technology, Kabelíkova 1, 750 02 Přerov, Czech Republic, 2015, iSSN: 1614-8436.

[76] A. N. Bashkatov, E. A. Genina, Water refractive index in dependence on temperature and wavelength: a simple approximation, in: Saratov Fall Meeting 2002: Optical Technologies in Biophysics and Medicine IV, International Society for Optics and Photonics, 2003, pp. 393–395.

[77] A. B. Dahlin, J. O. Tegenfeldt, F. Höök, Improving the instrumental resolution of sensors based on localized surface plasmon resonance, Analytical chemistry 78 (13) (2006) 4416–4423.

[78] R. A. Sperling, W. Parak, Surface modification, functionalization and bioconjugation of colloidal inorganic nanoparticles, Philosophical Transactions of the Royal Society of London A: Mathematical, Physical and Engineering Sciences 368 (1915) (2010) 1333–1383.

[79] A. Kyrsting, P. M. Bendix, D. G. Stamou, L. B. Oddershede, Heat profiling of three-dimensionally optically trapped gold nanoparticles using vesicle cargo release, Nano letters 11 (2) (2010) 888–892.

[80] P. M. Bendix, S. N. S. Reihani, L. B. Oddershede, Direct measurements of heating by electromagnetically trapped gold nanoparticles on supported lipid bilayers, ACS nano 4 (4) (2010) 2256–2262.

[81] M. Šiler, J. Ježek, P. Jákl, Z. Pilát, P. Zemánek, Direct measurement of the temperature profile close to an optically trapped absorbing particle, Optics Letters 41 (5) (2016) 870–873.

[82] L. Malmqvist, H. M. Hertz, Trapped particle optical microscopy, Optics communications 94 (1) (1992) 19–24.

[83] L. Friedrich, A. Rohrbach, Surface imaging beyond the diffraction limit with optically trapped spheres, Nature nanotechnology 10 (12) (2015) 1064–1069.

[84] R. A. Sperling, P. R. Gil, F. Zhang, M. Zanella, W. J. Parak, Biological applications of gold nanoparticles, Chemical Society Reviews 37 (9) (2008) 1896–1908.

[85] M. Li, T. Lohmüller, J. Feldmann, Optical injection of gold nanoparticles into living cells, Nano letters 15 (1) (2014) 770–775.

[86] J. Xie, S. Lee, X. Chen, Nanoparticle-based theranostic agents, Advanced drug delivery reviews 62 (11) (2010) 1064–1079.

[87] L. Shao, Q. Ruan, R. Jiang, J. Wang, Macroscale colloidal noble metal nanocrystal arrays and their refractive index-based sensing characteristics, Small 10 (4) (2014) 802–811.

[88] L. Vigderman, P. Manna, E. R. Zubarev, Quantitative replacement of cetyl trimethylammonium bromide by cationic thiol ligands on the surface of gold nanorods and their extremely large uptake by cancer cells, Angewandte Chemie 124 (3) (2012) 660–665.

[89] S. Gómez-Graña, F. Hubert, F. Testard, A. Guerrero-Martínez, I. Grillo, L. M. Liz-Marzán, O. Spalla, Surfactant (bi) layers on gold nanorods, Langmuir 28 (2) (2011) 1453–1459.

A

Detailed measurement data from Section 4.3

In this Appendix a selection of detailed measurements used to generate the time evolution graphs in Section 4.3 are presented. These include autocorrelation signals which have been fitted to extract the information about the rotational dynamics of the trapped particle as well as DF scattering spectra to determine the LSPR peak positions. The important extracted parameters from these two measurements are presented in the figures.

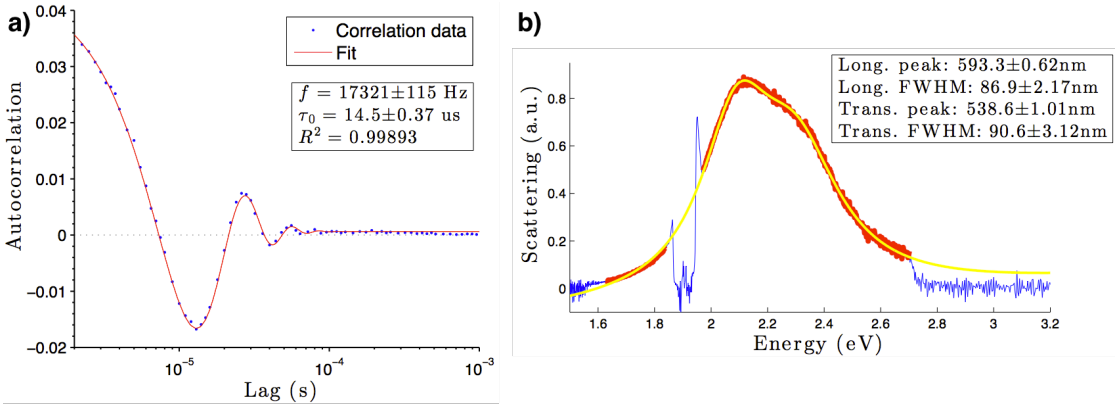

Figure A.1: Examples of detailed measurements for particle in the constant laser power experiment in Section 4.3.1. Measured autocorrelation data together with a fit to the model function (a) and recorded DF scattering spectra together with a fit (b). In the figures the extracted parameter of important are presented.

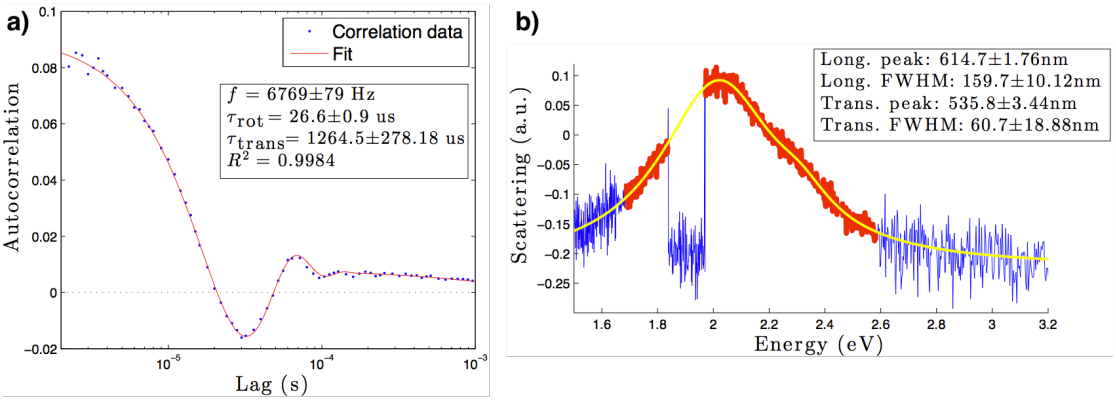

Figure A.2: Examples of detailed measurements for particle in the single triangular power ramp experiment in Section 4.3.2. Measured autocorrelation data together with a fit to the model function (a) and recorded DF scattering spectra together with a fit (b). In the figures the extracted parameter of important are presented.

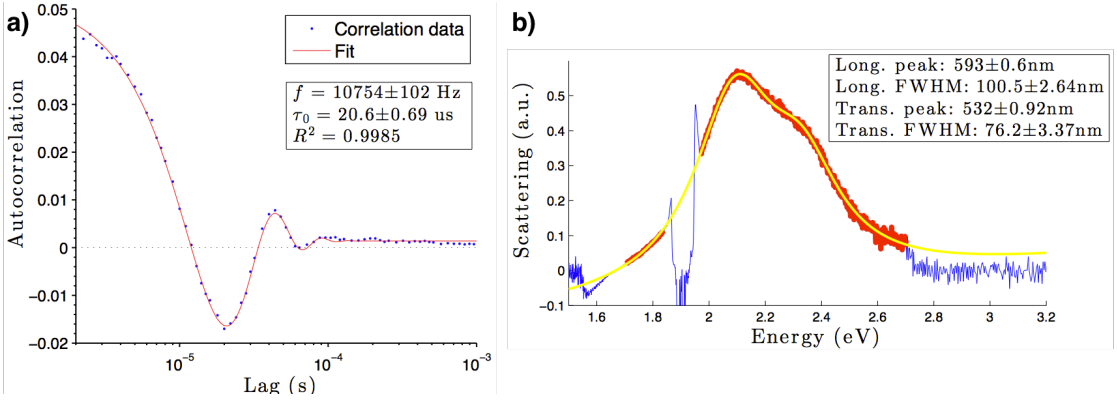

Figure A.3: Examples of detailed measurements for particle in the consecutive triangular laser ramps with linearly increasing maximum experiment in Section 4.3.3. Measured autocorrelation data together with a fit to the model function (a) and recorded DF scattering spectra together with a fit (b). In the figures the extracted parameter of important are presented.

B

Second argument against desorption of CTAB

A dense colloidal solution of nanorods contains a concentration of about $5 \cdot 10^{10}$ NR/ml and need a concentration of CTAB that is $20\,\mu$M in order to stabilize the solution [87]. When the solution of gold nanorods for experiments is prepared, the dense solution is diluted by about 10000 times and then $4\,\mu$L of this dilute solution is used. This small volume of solution would then contain $2{\cdot}10^4$ nanorods and $\frac{20\,\mu\text{M}}{10000}{\cdot}4{\cdot}10^{-6}{\cdot}6.02{\cdot}10^{23} = 4.82{\cdot}10^9$ number of CTAB molecules. If we assume that all the CTAB molecules bind to nanorods then that makes approximately $\frac{4.82{\cdot}10^9}{2{\cdot}10^4} = 2.41 \cdot 10^5$ CTAB molecules per nanorod. The surface area of the nanorod is estimated by the surface area of a hemispherically capped cylinder of appropriate dimensions to $A_{\text{NR}} = 4\pi ab = 2.2 \cdot 10^4\,\text{nm}^2$. This makes for a surface distribution of $\frac{2.41{\cdot}10^5}{2.2{\cdot}10^4} \approx 11\,\text{CTAB/nm}^2$. To form a monolayer of CTAB on gold a surface density of $3.7\,\text{CTAB/nm}^2$ is needed [88]. This would make the CTAB concentration in our experiments enough to form at least a bilayer of CTAB. A full bilayer of CTAB could be estimated to have a thickness of 3.4 nm [89], which would indeed change the refractive index that the gold nanorod experiences enough to produce a peak shift of several nanometers. As the particle was heated and CTAB molecules would desorb it would produce a peak shift of the longitudinal peak of some nanometers, potentially explaining the peak shift observed in Figure 4.6.

However, the estimate just preformed assumes that all the CTAB molecules bind to the gold rods, with nothing remaining in solution and no CTAB molecules bound anywhere else. In fact, the washing procedure of the microscope slides, used to fabricate the sample cell, make the glass high negatively charged. This will make it equally if not more attractive to the positively charged head groups of the CTAB molecules than the gold nanorods are. The glass in contact with the solution is estimated to have a surface area of $25\,\text{mm}^2 = 25 \cdot 10^6\,\mu\text{m}^2$. If all CTAB was instead bound to the glass surface the density of CTAB on the glass surface would be as low as $\frac{4.82{\cdot}10^9}{2.5{\cdot}10^7} = 192\,\text{CTAB}/\mu\text{m}^2 = 1.92 \cdot 10^{-4}\,\text{CTAB/nm}^2$.

In reality, it is reasonable to believe that some CTAB molecules will bind to the gold particles and some to the glass surface while some remain free in the solution. Yet, due to the fact that the glass surface has a surface area that is several orders of magnitude larger than the collective gold particle surface area it should be safe to argue that the CTAB layer on the single gold particle should be less than a monolayer and therefore the peak shift from desorption of the surfactant molecules from the gold should not be enough to explain the blue shift of the longitudinal peak.